

THREE DIMENSIONAL ANALYSIS OF THE GAS FLOW IN PISTON RING PACK

By

Ali Kharazmi

A DISSERTATION

Submitted
to Michigan State University
in partial fulfillment of the requirements
for the degree of

Mechanical Engineering – Doctor of Philosophy

2017

ABSTRACT

THREE DIMENSIONAL ANALYSIS OF THE GAS FLOW IN PISTON RING PACK

By

Ali Kharazmi

Cylinder-kit dynamics design in an internal combustion engine is highly relevant for the engine performance characteristics, durability and reliability. Since the middle of the 20th century, researchers have been using numerical models to describe the processes that occur in a ring pack. Because it is difficult and extremely costly to conduct experiments on every series of engines to check for the blow-by and oil consumption, a computational analysis can be performed on the ring pack to study the blow-by and oil-consumption characteristics.

In this dissertation a 3D CFD simulation model is introduced to analyze the flow between the cylinder liner and the piston. This model allows for calculation of the piston assembly with consideration of the ring dynamics, transient boundary conditions for combustion chamber pressure and temperature as well as thermal distortion of the piston and liner. The determination of the complex geometry of the cylinder-kit is established in a STL (STereoLithography) format by considering the complicated geometrical details of the ring pack such as thermal distortion of piston and liner, ring twist and ring/groove conformability. The blow by and blow back is numerically calculated for a small bore cylinder operating at 2000 RPM and verified by the results of commercially available 1D models.

The calculated velocity field shows substantial circumferential flow in the piston ring pack that is dominated by the ring and groove geometry as well as the relative position of the rings end gap. It is found that the amount of gas that flows back to the combustion chamber increases when the in-cylinder pressure trace decreases from its peak value. The knowledge from this study can be used as a basis for further multiphase calculations containing oil flow such as oil consumption, oil evaporation and eventually cylinder-kit wear.

Copyright by
ALI KHARAZMI
2017

This thesis is dedicated to my parents for their constant support and unconditional love and to my grandfather who taught me how to live life to the fullest

ACKNOWLEDGMENTS

I would like to thank my committee members for their guidance and constructive advices. In particular, I would like to thank my thesis supervisor Dr. Harold J. Schock, who not only gave me the opportunity to conduct my doctoral studies at Michigan State University, but also supported and guided me consistently through his insightful and broad knowledge. I enjoyed and will remember every single discussion with him, which helped me to solve the problems I encountered and eventually leaded to the achievement of my thesis work. Besides being a respectable advisor, Dr. Schock has been the most instructive and supportive friend during my time at MSU. I would also like to express my gratitude to Professor Farhad Jaberri for the continuous help over the years, especially his advices on Computational fluid dynamics. My sincerely thanks to Professor Guoming Zhu and Professor Carl Lira for accepting being part of the committee and delightful suggestions.

I would like to thank the people from Cummins including Dr. Dan Richardson and Mr. William D. McNulty, whom I have the opportunity to work with. Also I would like to take this opportunity to thank the passionate and gifted engineer Dr. Chao Cheng from Cummins for his supports and invaluable suggestions throughout the years as well as his guidance in understanding the modeling techniques in CASE.

My deep appreciation goes out to my friends and colleagues: Ravi Vedula, Sedigheh Tolou, Tom Stuecken, Brian Rowley, Jenny Higel and Jeff Higel. They have made the lab a fun place to work and have been always there to support me.

Last but not the least, I would like to thank my family: my parents and to my brothers for their encouragements trust and faith. This thesis would not have been completed without their unconditional support.

TABLE OF CONTENTS

LIST OF TABLES	viii
LIST OF FIGURES	ix
CHAPTER 1 INTRODUCTION	1
1.1 Introduction	1
1.2 Structure of this dissertation	3
CHAPTER 2 INTERNAL COMBUSTION ENGINES	4
2.1 Introduction	4
2.2 Cylinder kit assembly	4
2.3 Piston skirt and ring groove	6
2.4 Piston ring design	6
2.5 Gas flow through ring pack	14
2.6 Blow-by	14
2.7 Inter ring gas analysis	16
2.8 Piston ring flutter	19
2.9 Piston ring collapse	20
2.10 Piston ring twist	21
2.11 Piston ring lubrications	22
2.12 Three dimensional gas flow analysis	25
2.13 Previous efforts	28
CHAPTER 3 DEVELOPMENT OF A LINK PROGRAM	33
3.1 Introduction	33
3.2 LINK program	33
3.2.1 Overview of the Geometry in STL format	34
3.2.2 Geometry of Cylinder Kit Assembly in STL format	35
3.2.3 Modification of surface	36
3.2.4 Ring construction	37
3.2.5 Piston construction	41
3.2.6 Cylinder Liner construction	41
3.2.7 Final Assembly of the geometry	42
3.3 Simulation method	43
3.4 Geometry of the proposed problem	45
3.4.1 In-cylinder pressure "Binning"	47
3.4.2 Governing equations	49
3.4.3 Boundary conditions	51
3.4.4 Grid generation	53
3.4.4.1 2D and 3D Geometries grid	55
3.5 Simulation time of the 3D geometry	65
3.6 Parallel computing	66

3.6.1	Classification of parallel computer architecture	67
3.6.2	Issues in parallel computing	69
3.6.3	Scalability	70
3.6.4	Parallel processing in CONVERGE	70
CHAPTER 4 RESULTS AND DISCUSSION		74
4.1	Introduction	74
4.1.1	Test run 1 (Narrow channel)	74
4.1.2	Test run 2 (Hollow Cylinder)	76
4.1.3	Test run 3 (Channel with Obstacle)	78
4.2	Cylinder kit assembly Results	82
4.2.1	2D Results	84
4.2.2	2D Velocity Profile	85
4.2.3	2D Blow-By calculation	87
4.2.4	3D-Steady results	88
	4.2.4.1 Convergence of the results	88
	4.2.4.2 Pressure distribution	92
	4.2.4.3 Circumferential flow	94
	4.2.4.4 Blow-by calculation	97
4.2.5	3D-Unsteady results	100
	4.2.5.1 Blow-by calculation	101
	4.2.5.2 Blow-back	102
4.3	Conclusions	103
4.3.1	Wall clock time	104
4.3.2	Flow structure	105
4.3.3	Blow-by and blow-backs	106
CHAPTER 5 SUMMARY, CONCLUSIONS AND FUTURE WORK		107
5.1	Summary	107
5.2	Future work	107
	5.2.1 Simplifying the geometry	108
	5.2.2 Alternative method	109
	5.2.3 Fluent as the CFD solver	111
BIBLIOGRAPHY		112

LIST OF TABLES

Table 3.1	Grid specification for 2D cylinder-kit assembly	56
Table 3.2	Grid specification for 3D cylinder-kit assembly	61
Table 3.3	Simulation time for different grid levels of bin #1 inlet pressure	66
Table 3.4	Flynn’s Taxonomy	68
Table 4.1	Grid systems used for test run 1 - Narrow channel	75
Table 4.2	Grid systems used for test run 2 - Hollow cylinder	77
Table 4.3	Pressure bins after binning process	83
Table 4.4	Comparison between the 3D-steady and CASE pressure results (pressures are in <i>kPa</i>)	93
Table 4.5	Calculated mass flow rate for each bin pressure	99
Table 4.6	Calculated discharged mass for each bin pressure	99

LIST OF FIGURES

Figure 2.1	Schematic view of a typical cylinder kit assembly	5
Figure 2.2	Piston terminology	7
Figure 2.3	Schematic view of a piston and piston ring pack assembly	8
Figure 2.4	Various piston ring cross sections	9
Figure 2.5	Ring end gaps and clearances	12
Figure 2.6	Compression Ring terminology	13
Figure 2.7	Piston ring free shape (cam shape)	14
Figure 2.8	Detailed schematic view of crevice volumes in ring packs	15
Figure 2.9	Gas flow through crevices and location of blow-by	15
Figure 2.10	Conceptual diagram of the gas flow model in the piston ring pack	17
Figure 2.11	Forces acting on a piston ring inside a ring groove	18
Figure 2.12	Ring Flutter Scenario	19
Figure 2.13	Gas pressure on the ring with positive relative angle showing collapse scenario	21
Figure 2.14	Positive twist of the top ring	22
Figure 2.15	Negative twist of the 2 nd ring	22
Figure 2.16	Cross section of the oil film between the piston ring and cylinder liner	24
Figure 2.17	Flow of the gas through the ring end gap using orifice-volume method	27
Figure 2.18	Calculated geometry of a deformed (twisted) Piston ring	31
Figure 3.1	Orientation of a facet and its normal vector	34
Figure 3.2	Vertex to vertex rule - the left figure is the violation of this rule	35
Figure 3.3	A cube represented in STL format	35
Figure 3.4	Geometry of cylinder-kit assembly in STL format	36
Figure 3.5	Example of overlap surfaces condition	37

Figure 3.6	Example of overlap points condition	38
Figure 3.7	Top view of a installed piston ring in a bore	38
Figure 3.8	Top view of a slice of a piston ring installed in a bore	39
Figure 3.9	An arbitrary non-touching ring cross section	39
Figure 3.10	An arbitrary touching ring cross section	39
Figure 3.11	Piston ring element types. From left to right 1)TT 2) TN 3)NT 4)NN	40
Figure 3.12	Front view of a slice of a piston ring constructed by ring element concept	40
Figure 3.13	Different cross sections of the portion of a piston ring	41
Figure 3.14	Cross section of a piston	42
Figure 3.15	Constructed piston in STL format	42
Figure 3.16	3D representation of a completed cylinder kit assembly	43
Figure 3.17	Cross section of the studied geometry (units are <i>mm</i>)	46
Figure 3.18	2D-cut of the cylinder-kit	47
Figure 3.19	Complete 3D cylinder-kit geometry (sectioned)	47
Figure 3.20	Pressure trace curve	48
Figure 3.21	Binned pressure trace	48
Figure 3.22	Schematic view of the boundary conditions	54
Figure 3.23	An example of grid embedding (a) before and (b) after	55
Figure 3.24	Grid around ring 1 - Case No. 1	56
Figure 3.25	Grid around ring 1 - Case No. 2	57
Figure 3.26	Grid around ring 1 - Case No. 3	57
Figure 3.27	Grid around ring 1 - Case No. 4	58
Figure 3.28	Grid around ring 2 - Case No. 1	58
Figure 3.29	Grid around ring 2 - Case No. 2	59

Figure 3.30	Grid around ring 2 - Case No. 3	59
Figure 3.31	Grid around ring 2 - Case No. 4	60
Figure 3.32	Calculated mass flow rate of 2D geometry and various levels of grid size	61
Figure 3.33	Fixed embedding location (hatched area) in 3D geometry	62
Figure 3.34	The 3D grid system - Case No.1	63
Figure 3.35	The 3D grid system - Case No.2	63
Figure 3.36	The 3D Grid system - Case No.3	64
Figure 3.37	The 3D grid system - Case No.6	64
Figure 3.38	Parallel computing	67
Figure 3.39	Example of parallel Computing	67
Figure 3.40	Multiprocessor and Multicomputer	68
Figure 3.41	An example of automatic parallel domain decomposition of a duct: (a) duct surface geometry; (b) parallel blocks from user-specified <i>parallel_scale</i> , where each blue or red section represent a single parallel block; (c) assigned domain for four processors, where each color represents the computational region for a single processor (which is made up of several parallel blocks).	71
Figure 3.42	Load balancing for two different base grid sizes. Red lines demarcate parallel blocks, which can be assigned to different processors. Processor distributions are indicated by heavy dashed lines. Because the base grid size of (b) is half that of (a), parallel blocks can be more evenly distributed. In (a), note the bottleneck in Processor I, which has more than three times more cells than any other processor. Due to the large amount of cells in this processor, (a) has a longer runtime than (b).	73
Figure 4.1	Geometry of the test run 1 - Narrow channel	74
Figure 4.2	Snapshot of the grid systems used for test run 1 - Narrow channel	75
Figure 4.3	Velocity profile at the outlet for test run 1 - Narrow channel	76
Figure 4.4	Outlet velocity profile curve fit for test run 1 - Narrow channel	76
Figure 4.5	Geometry of the test run 2 - Hollow Cylinder	77
Figure 4.6	Snapshot of the grid systems used for test run 2 - Hollow cylinder	78

Figure 4.7	Velocity vector of the cut surface close to the inlet for test run 2 - Hollow cylinder	79
Figure 4.8	3D channel with different obstacle heights	80
Figure 4.9	Dimensions of the 3D channel with obstacle	80
Figure 4.10	Velocity field of the 3D channel for different simulation. On the left, uniform initialization simulation result is shown. On the right, the mapping simulation result is depicted	81
Figure 4.11	Velocity field and vortex eye location of 3D channel simulation	81
Figure 4.12	Cross section of the studied geometry	82
Figure 4.13	Binned pressure trace	83
Figure 4.14	Velocity field around the first ring in 2D simulation	85
Figure 4.15	Velocity profile at cross section A-A of figure 4.14	86
Figure 4.16	Velocity profile at cross section B-B of figure 4.14	86
Figure 4.17	Velocity profile at cross section C-C of figure 4.14	86
Figure 4.18	Velocity field around the second ring in 2D simulation	87
Figure 4.19	Averaging surface that cuts geometry in z direction, shown by green color	88
Figure 4.20	Average pressure vs. time for 3D-steady simulation at different locations and pressure bins	89
Figure 4.21	Average axial velocity vs. time for 3D-steady simulation at different locations and pressure bins	90
Figure 4.22	Variation of Reynolds number over the cut surface - first land	91
Figure 4.23	Variation of Reynolds number over the cut surface - skirt	91
Figure 4.24	Location of calculated pressure across the piston using CASE	92
Figure 4.25	Pressure profile for similar cylinder-kit assemblies but different 2 nd ring leakage area	94
Figure 4.26	Circumferential flow in 2 nd land	95
Figure 4.27	Circumferential flow in 3 rd land	95
Figure 4.28	Circumferential flow in the 2 nd land with twisted 2 nd ring	96

Figure 4.29	Circumferential flow in the 3 rd land with twisted 2 nd ring	97
Figure 4.30	Mass flow rate comparison in twisted and untwisted 2 nd ring geometries	98
Figure 4.31	Different regions of pressure trace in 3D-unsteady approach	100
Figure 4.32	Mass flow rate in Region 2 in 3D-unsteady approach	102
Figure 4.33	Velocity profile at the inlet showing blow-back	103
Figure 4.34	Velocity profile at the inlet showing blow-back	103
Figure 5.1	Removal procedure of the tiny areas in cylinder kit assembly	109
Figure 5.2	Sliced geometry of the full 3D geometry	110
Figure 5.3	Various slices of the 3D geometry with different twisted 1 st ring	110

CHAPTER 1

INTRODUCTION

1.1 Introduction

A reciprocating engine, also often known as a piston engine, is a heat engine that uses one or more reciprocating pistons to convert pressure into a rotating motion. Each piston is inside a cylinder into which a gas is introduced and its pressure is maintained via providing a seal between the sliding piston and the walls of the cylinder liner. The pressurized fuel air mixture in the combustion chamber is ignited to push the piston. This linear movement of the piston is converted to a rotating movement via connecting rod and crankshaft.

In the early steam engines no piston rings were used. Increasing power demands required higher temperatures, which caused stronger heat expansion of the piston material. This made it necessary to use a sealant between the piston and the cylinder liner to allow a decrease in the clearance in cold conditions, i.e. when the clearances were at their maximum. Keeping the clearance between the piston and liner wall at a minimum considerably reduces the combustion gas flow from the combustion chamber past the piston.

The so-called internal combustion engine cylinder-kit is comprised of the piston, piston rings and cylinder liner. The main purpose of the piston is to convert the thermal energy of the combustion gas into mechanical energy while the piston rings are accountable for eliminating energy loss by providing proper sealing to the combustion chamber. They also facilitate the heat transfer between the piston and cylinder wall.

It is generally believed that half of the mechanical energy losses in an engine occur in the cylinder kit assembly. Engine durability, performance, controlling the amount of lubrication, noise and vibration are all greatly affected by the ring pack design. Therefore a good piston ring design plays an important role in engine performance.

In recent years a significant amount of work has been done in the area of internal combustion

engine modeling and simulations. The compelling force of these efforts has been an industry trend for fuel efficient, low emission, quiet, durable and high output power engines that cost less. Computational tools have proven to be a valuable asset not only for designing engines but also for troubleshooting and optimizing the existing designs.

Engineers have utilized various methods for studying different aspects of piston rings. Material and structural mechanics are used to design piston rings that can withstand the high pressure and temperature of the combustion chamber while maintaining good sealing and low oil consumption. Wear analysis enables understanding the ring behavior under exhaustive cyclic movement to improve engine efficiency over time. Fluid flow analysis provides a basis for computing the pressure variations between and behind the rings in a ring pack as well as minimizing the blow-by (the amount of gas leakage past the rings). Lubrication fundamentals that are frequently used in analyzing piston and piston rings enables decreasing the oil consumption, friction between the ring face and wall cylinder while increasing the rate of heat transfer and sealing capabilities of rings.

The difficulties associated with obtaining a good ring pack design is a complex task. First because of the complicated nature of the governing physics of the internal combustion engines, the cyclic nature of the problem provides sufficient conditions for non-steady transient cyclic processes. Second, due to the highly coupled physical phenomena it is harder to study different physical aspects of the piston ring packs individually without sacrificing important details.

The tribological considerations in the contacts formed by the piston skirt, piston rings and cylinder liner, or bore, have attracted much attention over several decades, not least indicated by the large number of articles published on this topic in recent years. Recent studies include ring pack design and analysis in one and two dimensional formulations; Ranging from predicting the kinematics of the ring pack, to computing the flow behavior and wear analysis. However, some features such as ring rotation and accurate oil consumption and blow-by in designing the ring pack can only be explained by taking into account the circumferential effect (e.g. 3 dimensional analysis).

The advancement of technology in recent years has enabled scientist to do more complex nu-

merical simulations. Super computers and cloud computing systems has come to the aid of engineers to model details of geometry accurately. To name a few, AVL[1] and Federal Mogul[2] are the two prominent companies working on 3D analysis of the ring pack dynamics.

In this study, we aim to model the flow between the cylinder liner and piston to provide a framework for studying 3D physics of a Cylinder kit assembly. The focus of this work is to find the behavior of the flow using Computational Fluid Dynamics (CFD) in order to investigate the effect of ring twist on the ring blow-by.

1.2 Structure of this dissertation

This thesis is organized as follow. An overview of the cylinder kit and its components is included in Chapter 2. In Chapter 3, the theory behind the flow of the gas through the ring pack is described and previous efforts are revised. The governing equations, results and discussions are presented in Chapter 4. In Chapter 5, the future works and suggested methods are reviewed.

CHAPTER 2

INTERNAL COMBUSTION ENGINES

2.1 Introduction

In this chapter, the main components of an internal combustion engines are introduced and their functions are explained. The gas flow through the cylinder kit assembly is explained and different physical phenomenon's' involving the piston ring is discussed. Oil consumption mechanism is described later in this chapter and finally a brief summary of previous studies on the analysis of different aspects of the internal combustion engines are demonstrated.

2.2 Cylinder kit assembly

Internal combustion engine is the one in which combustion of the fuel takes place in a confined space, producing expanding gases that are used directly to provide mechanical power. Such engines are classified as reciprocating or rotary, spark ignition or compression ignition, and two-stroke or four stroke. The most familiar combination, used from automobiles to lawn mowers, is the reciprocating, spark-ignited, four-stroke gasoline engine. Engines are rated by their maximum horsepower, which is usually reached a little below the speed at which undue mechanical stresses are developed.

The most common internal combustion engine is the piston type gasoline engine used in most automobiles. The confined space in which combustion occurs is called a cylinder in which a piston slides up and down. The reciprocating motion of the pistons is translated into crankshaft rotation via connecting rods. The term "Cylinder kit assembly" is defined as the assembly of the piston, piston rings, cylinder liner, cylinder head, Intake and exhaust port. A Schematic view of a cylinder kit assembly in a four-stroke gasoline engine is shown in Figure 2.1.

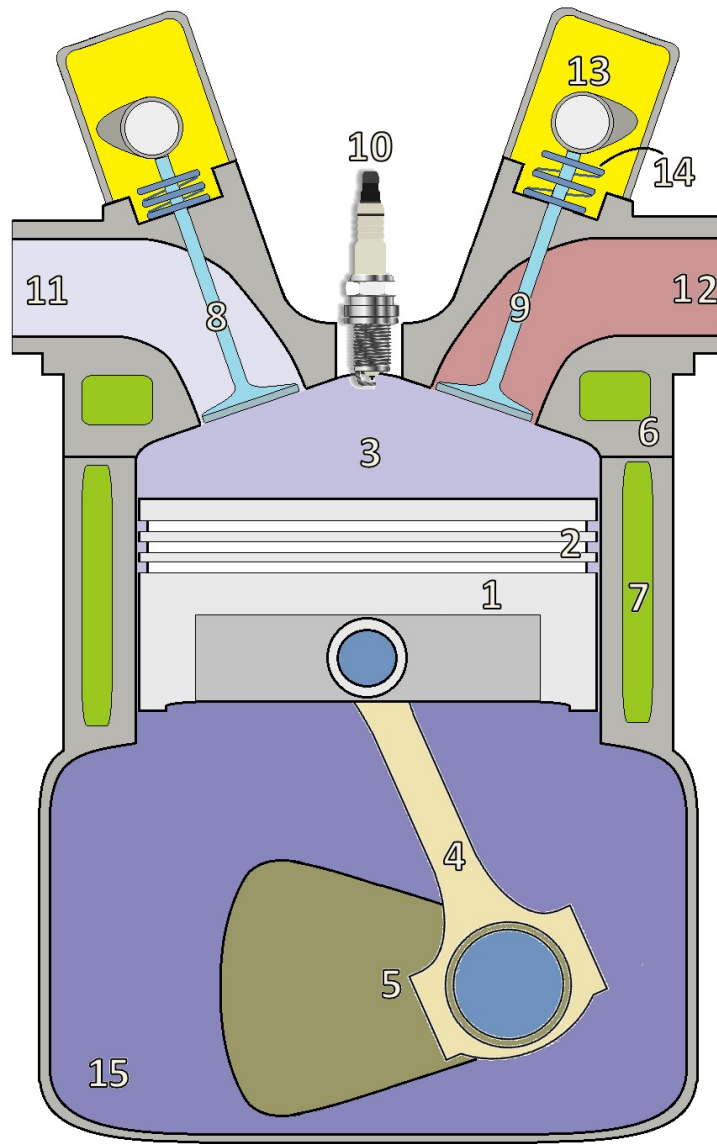


Figure 2.1 Schematic view of a typical cylinder kit assembly

- | | |
|----------------------|-----------------|
| 1-Piston | 9-Exhaust Valve |
| 2-Ring pack | 10-Spark Plug |
| 3-Combustion Chamber | 11-Intake Port |
| 4-Connecting Rod | 12-Exhaust Port |
| 5-Crank Shaft | 13-Camshaft |
| 6-Cylinder head | 14-Valve Spring |
| 7-Cooling Water | 15-Crank Case |
| 8-Intake Valve | |

2.3 Piston skirt and ring groove

A piston is a cylindrical shaped piece of metal that moves up and down inside the cylinder and converts thermal energy into mechanical work. The piston rings seal the combustion chamber from the crankcase and transfers heat to the coolant. The piston skirt, acts as a load-carrying surface that keeps the piston properly aligned within the cylinder bore.

The most essential area of the piston is the piston top (crown), the ring belt including the top land, the pin support, and the skirt. The geometry of these areas can vary significantly in compliance with the field of application.

The height of the top land has a major role in determining the emission and the power output of the engine. The second land has to be thick enough to withstand the pressure load created by combustion. The combustion pressure is reduced progressively and therefore the third land can be designed relatively thinner to reduce piston mass. The construction of a typical piston and ring assembly is shown in Figure 2.2.

The piston skirt extends below the piston crown. It is comprised of the major and minor thrust side, also referred as thrust and anti-thrust sides. The major thrust side is the one that experiences the highest loads during the expansion stroke because of the connecting rod orientation. The main function of the piston skirt is to provide guidance for the piston during its reciprocating motion and also provides optimal control over the piston secondary motion and reducing oil consumption and noise. A well-designed piston requires a comprehensive study of the deformation, thermal load and material of the piston.

2.4 Piston ring design

Piston rings have been an area of considerable focus and development for internal combustion engines. Piston rings may account for a considerable proportion of the total friction in the engine, as much as 24% [3]. The first piston rings installed in an engine was for closing off the combustion chamber, inhibiting the gases from the combustion process from escaping into the crankcase.

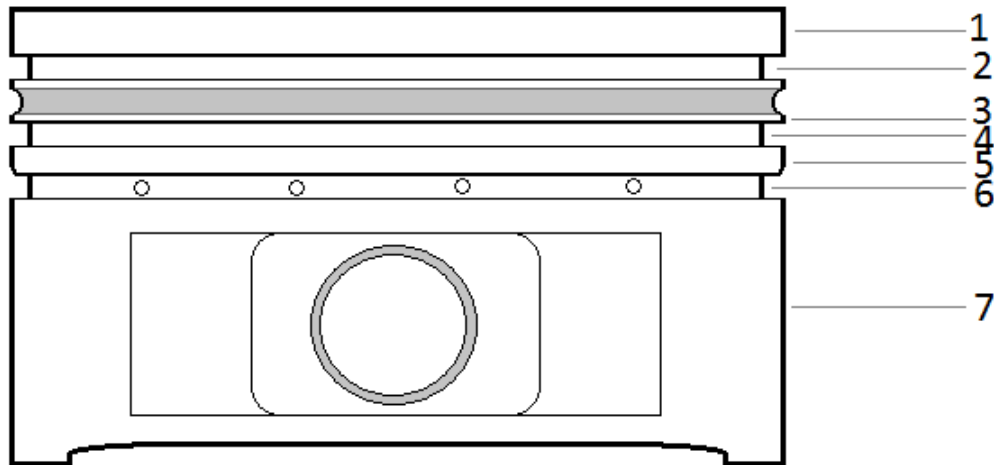


Figure 2.2 Piston terminology

- 1- Top Land
- 2- Top Ring Groove
- 3- Second Land
- 4- Second Ring groove
- 5- Third land
- 6- Third Land Groove
- 7- Piston Skirt

This development increased the effective pressure on the piston. Ramsbottom and Miller [4] were among the first innovators to examine the piston rings performance in steam engines. Previous piston rings were consisted of multiple pieces and were attached with springs to provide an adequate pressure sealing force against the cylinder bore. Miller, in 1862 [5] devised a system whereby steam was purposely used to affect the seal, without the aid of the ring's elasticity. In the early days, the ring pack was lubricated solely by splash lubrication; i.e. lubrication by the splashing of the rotating crankshaft into the crankcase oil surface. Oil control rings were introduced after higher demand of temperatures, pressures and piston speeds [5].

Piston rings form a ring pack, which usually consists of 2–5 rings, including at least one compression ring. The number of rings in the ring pack depends on the engine type, but usually comprises 2–4 compression rings and 0–3 oil control rings. The ring pack in todays engines is usually comprised of a compression ring, scraper ring and one oil control ring.

The construction of typical piston ring assembly is shown in Figure 2.3

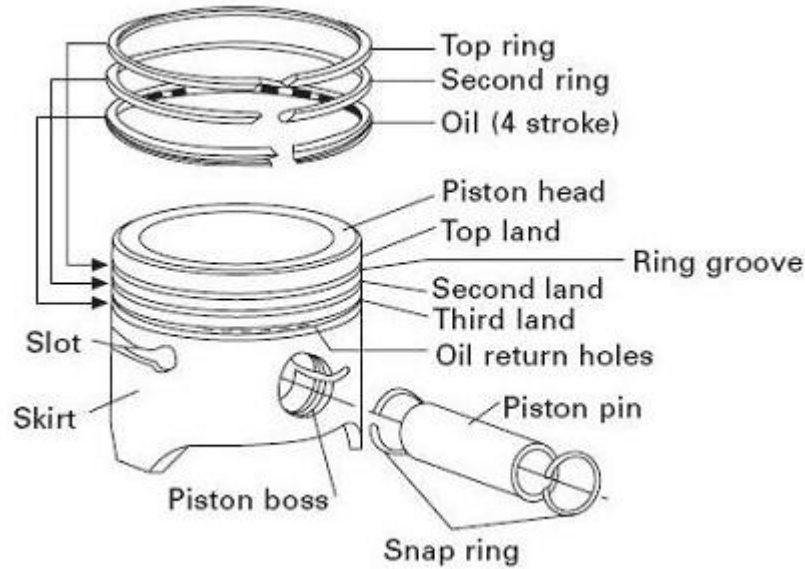


Figure 2.3 Schematic view of a piston and piston ring pack assembly

Over the years numerical models and computational tools have been developed in an attempt to model the piston ring behavior and estimate its performance and its efficiency of the internal combustion engine. The primary functions of the ring-pack designs include the following:

1. Controlling blow-by by preventing the air/fuel mixture from escaping the combustion chamber to the crankcase.
2. Controlling oil, by distributing oil evenly on the cylinder liner and preventing oil from contaminating the combustion chamber.
3. Transferring heat from piston to the cylinder wall and ultimately to the cooling jacket.

Piston rings are subject to wear as they move up and down the cylinder bore due to their own inherent load and due to the gas load acting on the ring. To minimize this, they are made of wear-resistant materials and are coated or treated to enhance the wear resistance [6]. Ring coatings have been under development for several years and their general adoption by nearly all automobile companies indicates both the need for them and their effectiveness. The coatings fall into two general classes, chemical and metallic. Grey Cast iron is used as main material for piston rings[2]

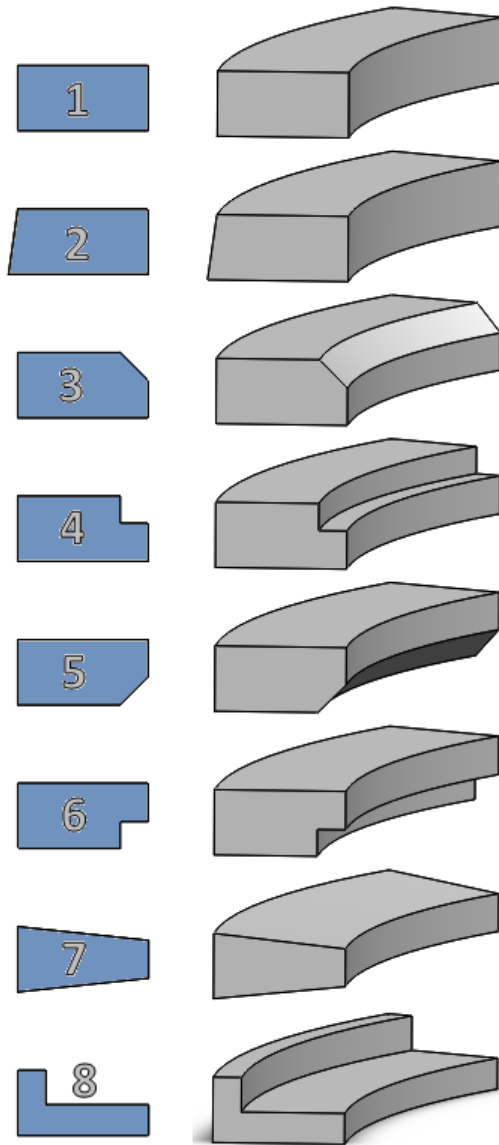


Figure 2.4 Various piston ring cross sections

because of its excellent wearing properties. Coatings for rings are also widely used to further decrease the wearing. One example of such a coating is chromium, which is used in abrasive and corrosive conditions where running conditions are severe. Hard chrome plating is particularly relevant for the compression ring. Careful tests under accelerated wear or scuffing conditions on newly finished surfaces shows that untreated rings produces twice the wear that occurs on the coated rings when only the compression rings are coated [7].

Depending on the functionality and purpose, there are different types of piston rings which are shown in Figure 2.4.

Rectangular Ring: A piston ring with rectangular cross section that can perform necessary sealing under normal operating conditions (Cross section 1 of Figure 2.4). The rectangular ring is mainly used in the top groove in today's passenger car gasoline and diesel engines.

Taper Faced Ring: The taper faced rings are mainly installed in the second groove in passenger car gasoline and passenger car and truck diesel engines and are utilized to further seal the combustion chamber and to wipe the cylinder wall clean of excess oil. Combustion gases that pass by the compression ring are stopped by this ring. (Cross section 2 of Figure 2.4)

Internally Beveled or Stepped Ring: By providing an edge relief (i.e. the cut in the rectangular cross section) on the top side of rectangular and taper faced rings, a twist effect is achieved which, in all operating phases without gas pressure loading, brings the ring into bore contact only with its bottom outer edge while the inner edge contacts the bottom groove side (positive twist). This helps to improve oil consumption control. Under operating conditions the gas pressure forces the ring flat against the piston groove, creating an additional dynamic behavior of the ring. Rings of this kind are used in the top and second groove of passenger car gasoline and passenger car and truck diesel engines. (Cross sections 3 and 4 of Figure 2.4)

Taper Faced Ring with Inside Bottom Bevel or Step: In the installed condition the edge relief causes a negative twist, i.e. in the opposite direction to a ring with the relief on the top side. The taper must be larger than on a taper faced ring without twist or with positive twist so that the top outer edge is prevented from contacting the cylinder wall. The effect of the negative twist is to make the ring contact the groove and create a seal with its outer bottom side and its inner top side [8]. This type of ring is installed in the second groove in passenger car gasoline and passenger car and truck diesel engines. (Cross sections 5 and 6 of Figure 2.4). The ring twist angles are explained later in section 2.10.

Keystone Ring: As shown in Figure 2.4, this ring is a compression ring with a wedge cross section. With its tapered sides, radial movement of the ring in engine operation will cause the

axial clearance in the groove to increase and decrease. This greatly reduces ring sticking, as the ring continuously works its way free of the combustion residues. The keystone ring is used in the top groove in passenger car and truck diesel engines where ring sticking must be expected (Cross section 7 of Figure 2.4). A half keystone ring is used in the top groove of passenger car and truck diesel engines when a rectangular ring is no longer adequate in regard to ring sticking but a keystone ring is not yet warranted. In this case only the top side of the ring is tapered.

L-Shaped Compression Ring: This ring is used mainly in small two-stroke gasoline engines as a "head land" ring, the vertical arm of the L being flush with the top edge of the piston crown [9]. With gas pressure acting behind the vertical arm, this ring will also seal when in contact with the top side of the piston groove.

In order to fit a ring into the grooves of the piston, it is not continuous but is broken at one point on its circumference. This split in the piston ring is called ring end gap and is shown in Figure 2.5a. This is necessary for installing the ring on the piston and allowing for expansion from heating. The gap must be such that there is enough space so the ends do not come together, as the ring heats up. This would cause the rings to break. There are a few variations of ring gap joints. Two stroke engines usually have pins in their ring grooves to keep the gap from turning. This is important because the ring would break if the ends were allowed to snap into the inlet or exhaust ports. Staggering the ring gap is also important as it prevents blow-by. For this reason, the top and second compression rings are assembled to the piston with their gaps 60-degrees offset with the first ring gaps. Rings must also be fitted for the proper side clearance (see Figure 2.5b). This clearance varies in different types and makes of engines; however, in a diesel engine, the rings must be given greater clearance compared to the gasoline engine. Too much side clearance will result in an excessive wear on the lands while too little side clearance, may result in the breaking the piston lands because of ring expansion.

It's been a well-accepted piston ring engineering design criteria, that for optimum performance, ring back clearance should be minimized [10]. This comes from the fact that the top compression ring needs the pressure from the combustion gases to get in behind the ring and push out on the

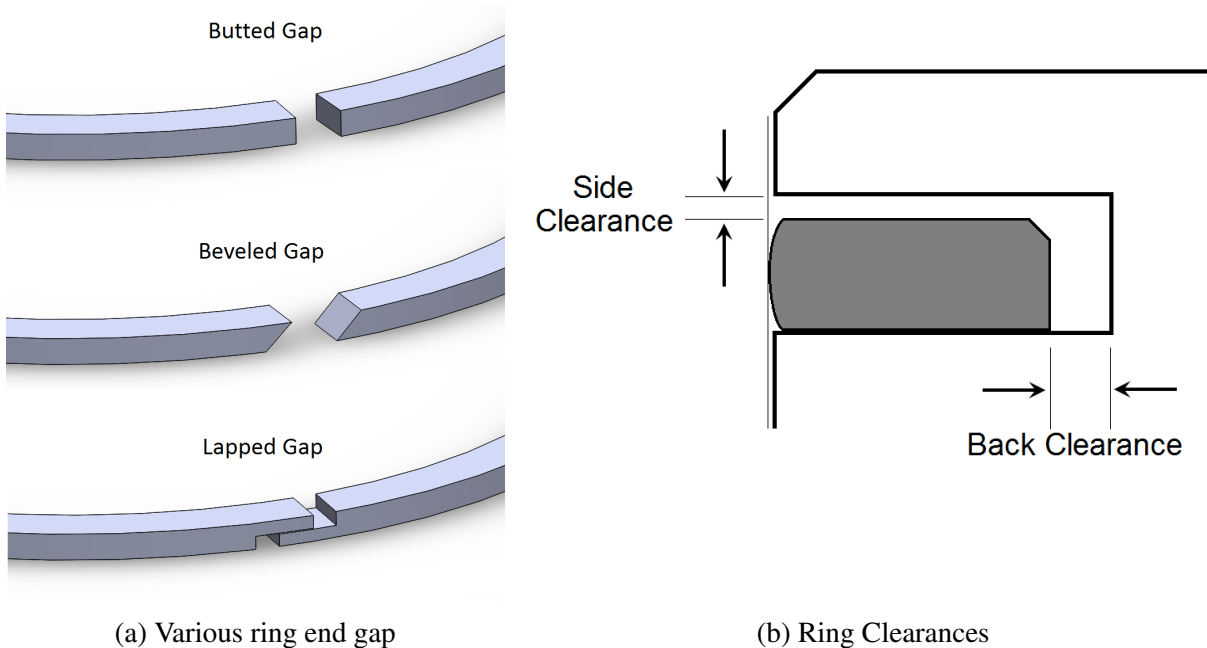


Figure 2.5 Ring end gaps and clearances

ring to maintain proper seal on the high pressure, or expansion stroke. The compression ring acts as a gas seal between the piston and the liner wall, preventing the combustion gases from trailing down to the crankcase. The rings have a certain pretension, i.e. they have a larger free diameter than the cylinder liner, which assists the ring in conforming to the liner. The cylinder gas pressure acts on the back-side of the ring, especially on the top ring, pressing it against the liner. The logic is that the smaller the area created by the back clearance, the quicker that pressure would build to push out on the ring, and the quicker the ring would react to its sealing requirements job. However, MAHLE found that the engine isn't nearly as sensitive to ring back clearance as it is to ring side clearance [11]. In any cylinder, there is enough very pressurized air available to fill the small space behind the ring very quickly if given enough room a.k.a. side clearance, to get there.

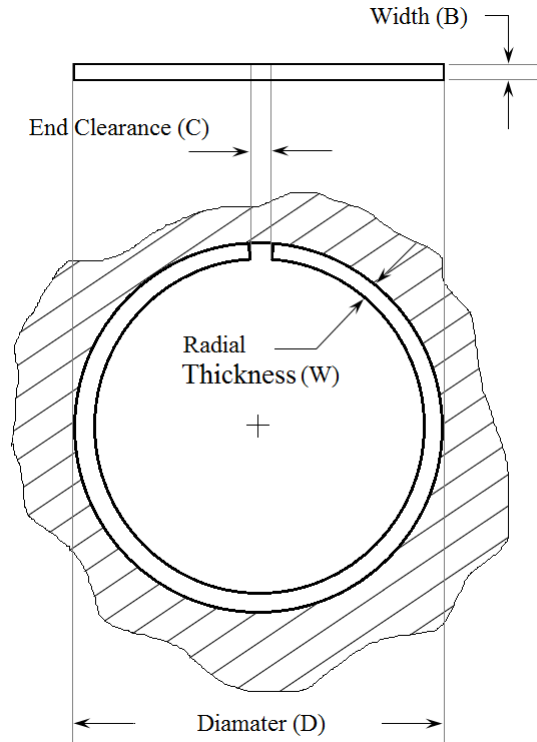


Figure 2.6 Compression Ring terminology

To understand the terminology of the piston ring a compression ring that is installed in a cylinder bore of diameter (D) is shown in Figure 2.6 . The radial thickness (W) is the distance between the outer diameter (O.D.) and inner diameter (I.D.) of the ring. Ring width (B) is the axial distance between the two sides. End clearance (C) is the shortest distance between the ends of the ring when the ring is installed in the bore. The end clearance at the O.D. may exceed the clearance at I.D.

The piston rings should have tension properties with which sealing effect is produced. Therefore the shape of the ring is different before and after installing inside the bore. The free shape of the ring (or sometimes called cam shape) is the profile of the ring before fitted inside the cylinder and is shown in Figure 2.7. Many expressions have been formulated for the coordinates of the free shape of the ring which will develop a specified pressure distribution when installed in a circular bore.

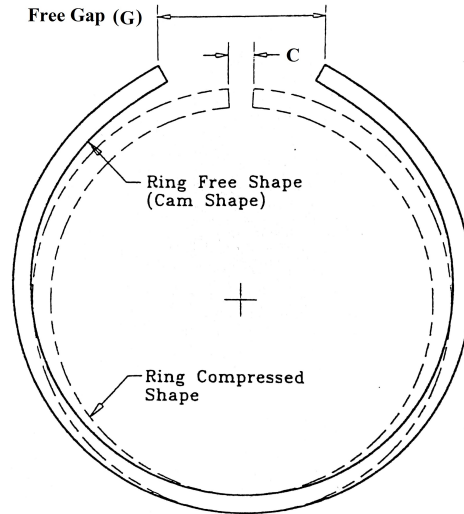


Figure 2.7 Piston ring free shape (cam shape)

2.5 Gas flow through ring pack

Small volumes found at the interfaces to the connecting parts in an engine's combustion chamber are called crevices. Gas flows into and out of these volumes during the engine operating cycles as the in-cylinder pressure changes. The total volume of the crevices is a few percent of the clearance volume which is altered when engine is warmed up [12].

The volumes between the piston, piston rings and cylinder liner walls are shown schematically in Figure 2.8. These crevices consist of series of volumes connected by flow restrictions such as ring side clearance and ring gap. Since the geometry of the crevices changes as the ring moves up and down in its ring groove during a complete cycle, the gas flow, pressure distribution and ring motion are highly coupled [13].

2.6 Blow-by

Blow-by is the phenomenon where combustion gases flow from the combustion chamber past the ring pack to the crankcase. The combustion gases flow past the piston ring at various locations: (a) at the piston ring gap, (b) past the front side of the piston ring at starved lubrication conditions, (c)

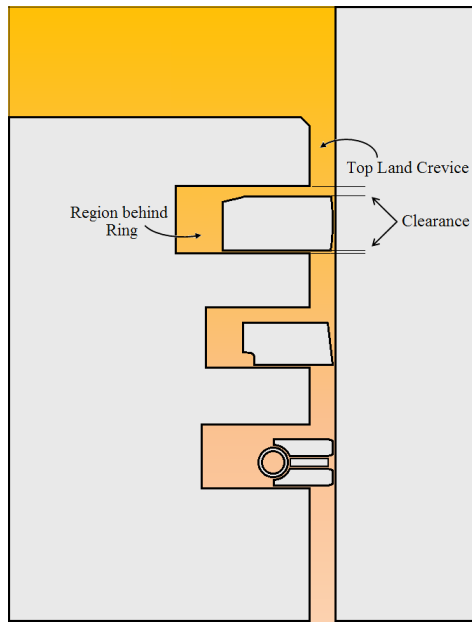


Figure 2.8 Detailed schematic view of crevice volumes in ring packs

or past the backside of the piston ring when the ring is not in contact with either of the ring-groove walls. The approximate location of the blow-by paths are shown in Figure 2.9.

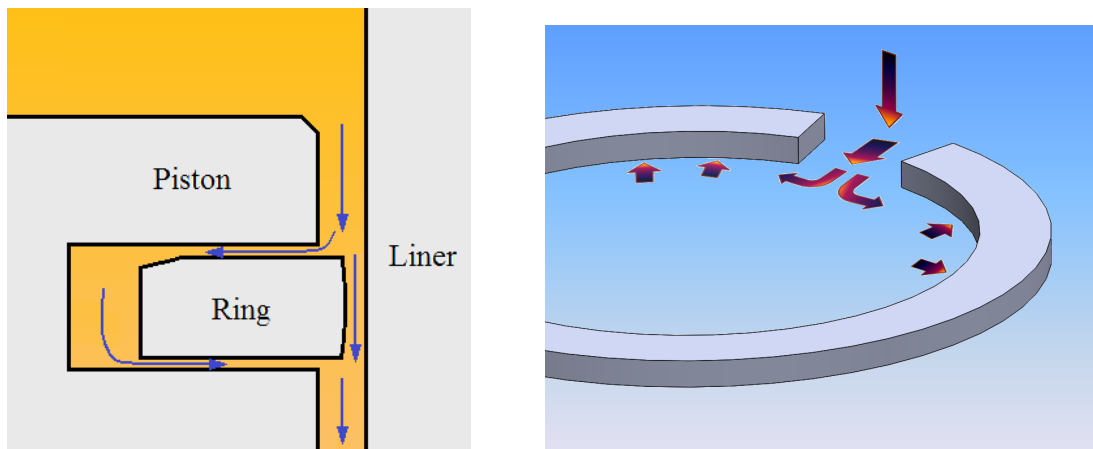


Figure 2.9 Gas flow through crevices and location of blow-by

Blow-by has an important effect on emission, oil consumption and power generated by the engine. Blow-by is majorly caused by different phenomena. When in-cylinder pressure is high during expansion or compression, ring floatation in the groove from side to side increases the blow-by. When inertia force dominates the pressure forces above the ring, causes the ring to lose

its stability in the axial and radial direction and collapse or flutter and create additional passage for the gas to escape combustion chamber. Additionally, when the ring is fitted to the cylinder bore the two ends do not seal completely. This allows for the creation of a flow passage which is purely dependent on end gap clearance. The end gap clearance is usually utilized to regulate interring gas pressures.

Ovality of the cylinder is another causes of blow-by because the ring can no longer seal the worn area. During normal operation, the cylinder, piston and the ring begin to wear. The cylinder wears the most on opposite sides (Major and minor thrust sides) which creates an oval shape to the cylinder. Combustion gases are blown by the ring into the crankcase, hence the name blow-by. This is seen as a reduction of compression as measured by compression test. The ring is designed to rotate around in its groove; however, carbon deposits are often left behind in the combustion process. Complex fuel molecules simply do not burn completely and are often left behind as a black deposit. One of the primary areas that these deposits accumulate is on the upper surface of the top ring of the piston. As these deposits accumulate, the ring movement becomes restricted, eventually resulting in the ring actually getting stuck.

2.7 Inter ring gas analysis

Figure 2.10 is a conceptual diagram of the gas flow inside the ring pack, modeled by orifice flow [14]. Gas is allowed to flow between different crevice regions to model the flow between the rings in a quasi-steady manner. It is done by assuming the combustion products as ideal gas and flow to be laminar. The mass flow between the crevices volumes are calculated using the law of conservation of mass (equation (2.1)) where the pressure and temperature of each region is assumed to be uniform. The crevice regions are shown in Figure 2.10.

$$\sum \dot{m}_{in} - \sum \dot{m}_{out} = \frac{dm}{dt} \quad (2.1)$$

The ring gap is assumed the orifice that connects the flow between each land. A discharge coefficient is assumed and the mass flow rate is found as equation (2.2):

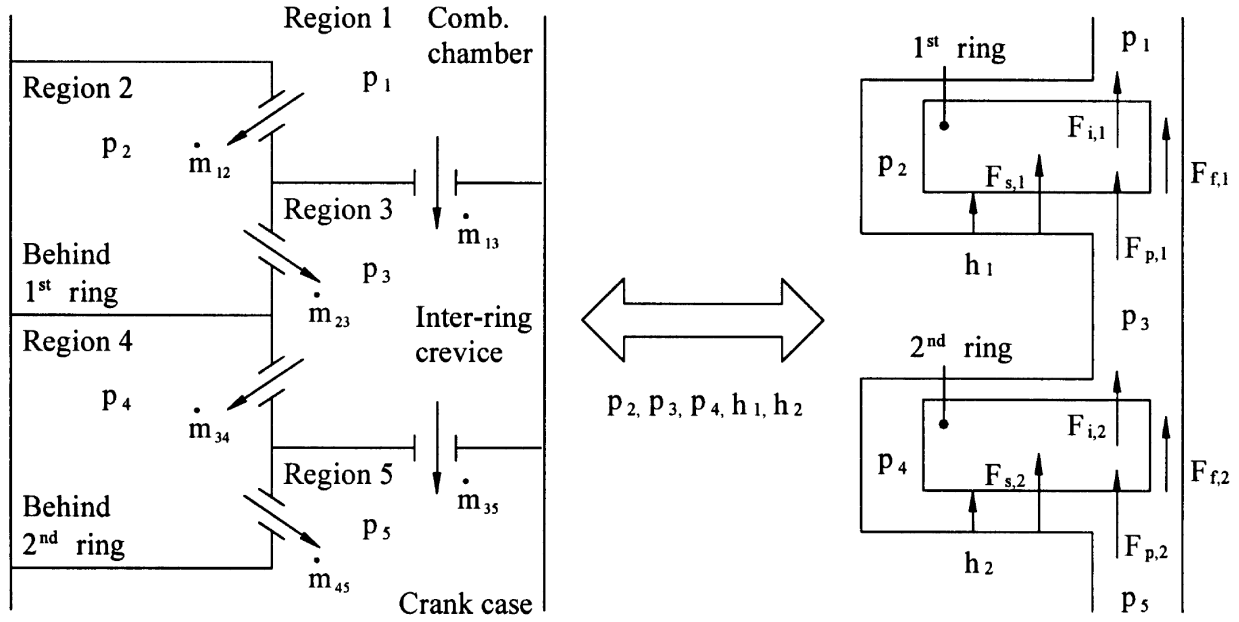


Figure 2.10 Conceptual diagram of the gas flow model in the piston ring pack

$$\dot{m} = K_c A \sqrt{\frac{2\gamma}{\gamma-1}} \left(\frac{P_1}{\sqrt{T_1}} \right) \left(\frac{P_2}{P_1} \right)^{\frac{1}{\gamma}} \sqrt{1 - \left(\frac{P_1}{P_2} \right)^{\frac{\gamma-1}{\gamma}}} \quad (2.2)$$

where:

- \dot{m} Mass flow rate
- A Flow area
- P Pressure
- T Temperature
- γ Specific heat ratio of Air
- K_c Orifice discharge coefficient

Assuming a constant crevice volume, constant gas properties and temperature in each piston crevice volume and using equation (2.1) the pressure changes in each crevice volume can be calculated as equation (2.3):

$$\frac{dp}{dt} \frac{V}{R.T} = \sum \dot{m}_{in} - \sum \dot{m}_{out} \quad (2.3)$$

The first step in understanding the ring dynamics and deformation is to study the forces acting upon a ring. Forces acting on a typical piston ring are shown in Figure 2.11. P_{top} is the gas

pressure above the piston ring. P_{bottom} is the gas pressure below the piston ring. $F_{inertia}$ is due to piston acceleration and deceleration. $F_{contact}$ and $F_{friction}$ are forces caused by ring contact with the cylinder liner and friction respectively. All of the loads acting on the ring can be projected as a combination of a radial force, axial force, and twisting moment acting at the ring cross-section center of gravity [15, 16].

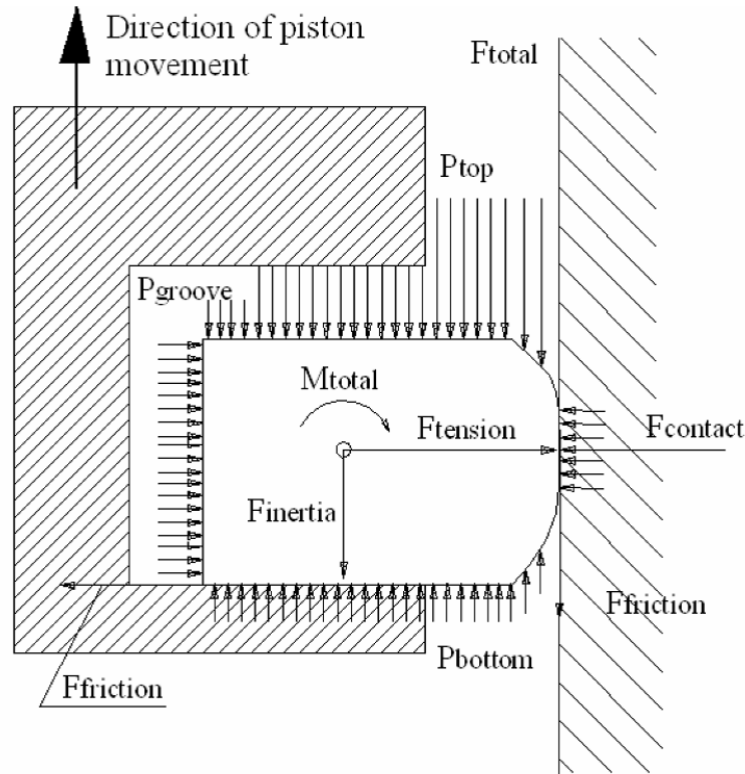


Figure 2.11 Forces acting on a piston ring inside a ring groove

The static force (i.e. when the engine is not operating) with which a piston ring presses against the cylinder wall depends mainly on the difference in diameters of the pre-stressed piston ring and the cylinder. This tangential force is designed in such a way that the piston ring meets the particular requirements arising from the combustion process and operating conditions. When the piston ring is installed in the cylinder, a tangential force is created that in turn generates the contact pressure.

Understanding these forces has enabled engineers to explain ring dynamic in the groove and

has shed lights on phenomena such as ring flutter and collapse.

2.8 Piston ring flutter

The gas always flows through the ring gaps under the pressure difference between the regions separated by piston rings. The ring may lose its stability in the axial and radial direction and introduces new paths of gas leakage additional to the ring gaps. At high engine speed, physical breakage and piston ring flutter can occur, resulting in loss or even engine destruction. Due to lower pressure gradient across the ring, the ring inertial force becomes competitive to gas pressure force [17].

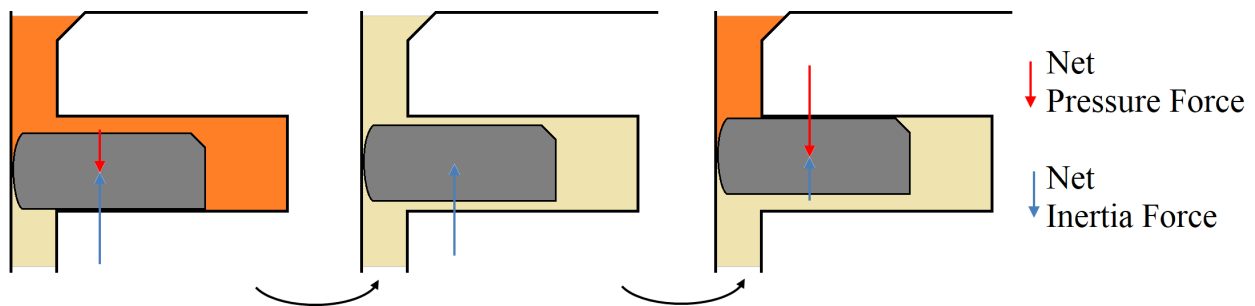


Figure 2.12 Ring Flutter Scenario

In essence, ring flutter inside the groove is an unstable axial in-groove motion which is the result of strong coupling between the ring dynamics and gas flows. First, the ring moves to the other side of the ring groove due to change in the direction of the net force on the ring; then, the ring motion gradually leaves a large enough clearance between the ring and the groove and introduces strong gas flow through the groove and fast land pressure variation. As a result of the land pressure variation, the net force reverses the direction and the ring moves back. This process may repeat depending on the pressure build-up above the second ring when it is top seated [18–20].

Ring flutter, which is mainly driven by the competition of the difference in gas pressures and the inertial force, has significant effects on gas flow as well as the oil flow. To control top-ring flutter, it is necessary to create first a positive ring-groove relative angle and second, to find ways

to reduce ring dynamic twist during dynamic situations. Thus, the ring static twist, groove tilt angle, ring material and axial height are important parameters for controlling top ring flutter [17].

Unlike top-ring flutter, second ring flutter has much smaller effects on blow-by. Any increase in blow-by due to second ring flutter most likely is because second ring flutter reduces the amount of reverse gas flow through the top ring by quickly releasing the second land gas to the lower land and reducing the second land pressure. Therefore, second ring flutter may be beneficial to oil consumption reduction if it indeed results in higher blow-by [21].

The second ring flutter effect in decreasing oil consumption is provided by two phenomena. The gas flow through the groove during ring flutter may be able to first, bring the oil in the second land and inside the second ring groove to the lower region and second, provide a resistance to the oil moving to the second ring groove from the third land. Therefore, in many situations, the design purpose is to create second ring flutter [22].

2.9 Piston ring collapse

A ring may be pushed inwards by the gas pressure acting on the ring running surface and causes a direct gas leakage through the ring-liner interface [21]. The emergence of the additional gas flow path during ring radial collapse also has a direct impact on blow-by and oil transport. This phenomenon is called ring radial collapse.

Ring radial collapse mainly occurs when a ring seals the gas flow path through the upper side of ring-groove clearance by making contact with the O.D. (outer diameter) corner of the upper side of the groove. By having such contact, the ring can stay on the top with maximum stability under gas pressure of the upper land, as illustrated in Figure 2.13. Thus, generally, ring collapse requires a positive relative angle between the upper flanks of the ring and the groove. Consequently, ring radial collapse is more likely to occur for the second ring with a positive static twist (Napier or simple taper face; refer to Figure 2.4) because the second land pressure rises relatively slowly and thus the inertial force has the opportunity to bring the second ring up at a certain point of the late

part of the compression stroke [18].

Although a large static twist stabilizes the top ring and reduces the extent of the operating condition regime that has top-ring flutter, top ring static twist can create top-ring collapse when it is too large.

2.10 Piston ring twist

Depending on the pressure difference around the rings, the gas flows between cavities which will change the inter-ring pressure and the pressure loads acting on the rings inevitably generates ring dynamic twist. Creating different static ring-twists is one of the major ways to control blow-by, oil consumption, and wear. The net force on the ring and the contact between the ring and the ring groove are altered greatly with different ring twist angles. As a result, ring stability, land gas pressure, and the wear of ring/groove and ring/liner may be changed [17].

Although the exertion of various forces on the ring can generate ring dynamic twist; creating different static ring-twist is one of the major ways to control blow-by, oil consumption, and wear [23]. The net force on the ring and the contact between the ring and the ring groove are changed greatly with different ring twist angles and as a result, ring stability, land gas pressure, and the wear of ring/groove and ring/liner may be changed [17].

Most rings are cut with a bevel to help the ring twist in its groove. The top ring will have the

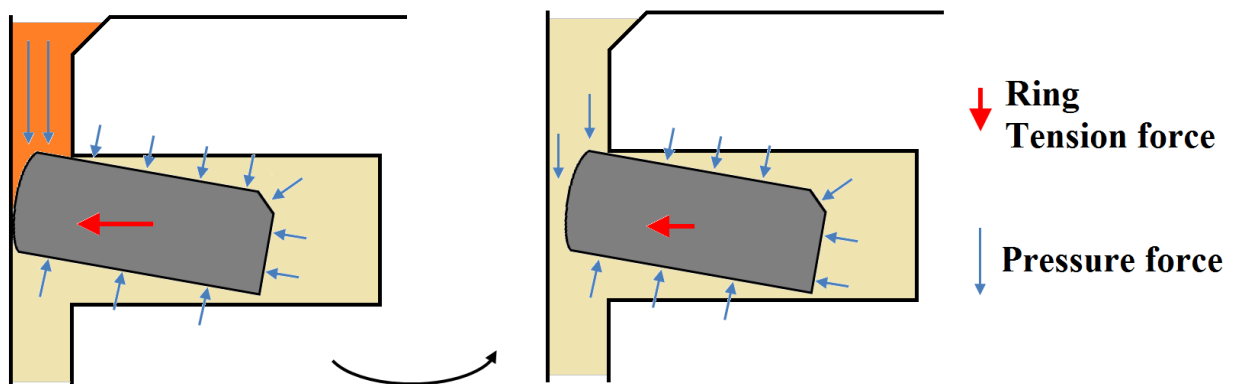


Figure 2.13 Gas pressure on the ring with positive relative angle showing collapse scenario

bevel on the inside top edge which twist the face downward. This is referred as positive twist, and it allows the cylinder pressure to get behind the ring and push it out against the cylinder wall for a better seal. Positive twist also holds the inside bottom edge of the ring against the ring groove for oil control purposes [17]. (See Figure 2.14)

The second compression ring uses a bevel on its inside bottom edge to create a negative twist. This helps position the bottom face of the tapered edge of the ring against the cylinder liner, while the inside top edge seals against the ring groove. That allows the oil scraped off the cylinder wall to pass under the ring and through the return holes in the back of the ring groove. (See Figure 2.15)

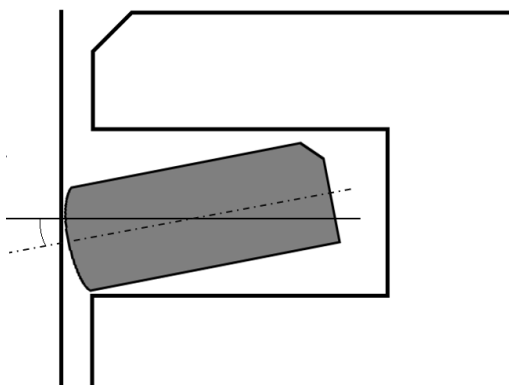


Figure 2.14 Positive twist of the top ring

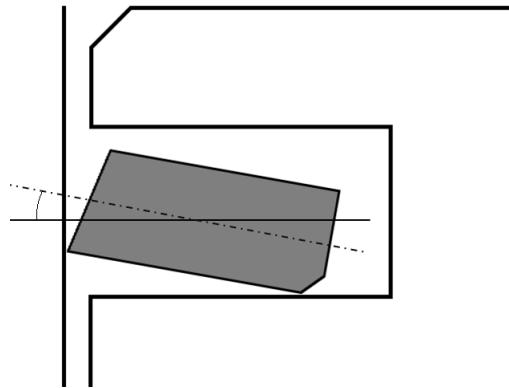


Figure 2.15 Negative twist of the 2nd ring

2.11 Piston ring lubrications

Engine oil consumption is one of the primary interests for the automotive industry in controlling emissions and reducing service cost. Due to a lack of understanding of the mechanisms of oil transport along the piston, reducing oil consumption from the ring pack of internal combustion engines has been extremely challenging for engine manufacturers and suppliers [24].

Because the rings are sliding along the liner and the groove sides, lubrication is needed to minimize friction and wear. Consequently, a sufficient lubricant supply must be provided in the contact regions. The performance of the piston ring pack can thus be regarded as a compromise between friction, wear, and oil consumption [24]. The key to minimizing oil consumption is to optimize oil transport within the piston ring pack. Because the regions above the oil control ring

are only partly flooded with oil [25, 26], the rate at which oil flows from the upper skirt region to the combustion chamber is the result of numerous oil transport processes between the various regions defined by the ring pack geometry, namely the piston lands, the ring grooves, and the liner [27].

One of the major difficulties for oil transport analysis lies in the number of sub-regions and the multitude of flow paths. For instance, oil may flow from one land to another through the grooves, the gaps or the ring liner interface. Furthermore, due to the motion of the rings in their grooves, connections between ring grooves and piston lands are repeatedly opened and closed, making the gas and oil flows highly coupled with the ring dynamics [27]. Potential driving forces for oil transports between the different parts of the piston ring pack are pressure gradients, shear stress from gas flows, ring/liner and ring/groove relative motion and inertia forces. Pressure gradients and resulting gas flows greatly vary in amplitude and direction with the engine load. Eventually, oil consumption and thus oil transports were found to be significantly affected by the detailed geometry of the ring pack components; to name a few, ring and groove relative angles, ring running surfaces [28–30], piston land geometry [31, 32] and bore thermal and mechanical deformations [33, 34].

The lubricant between the ring and the cylinder bore reduces the frictional resistance of the engine to a minimum to ensure maximum mechanical efficiency, protects the ring and the bore against the wear, and contributes to cooling the piston and the cylinder where the friction work is dissipated. [35]

The viscosity which is the most important property of a lubricant is a function of temperature and pressure [36]. Both friction and film thickness increases with increasing viscosity under normal engine operating conditions. The viscosity of lubricating oil decreases by increasing the ring temperature:

$$\mu = ae^{\left(\frac{b}{T+c}\right)} \quad (2.4)$$

Where a is the viscosity at $T = \infty$, b and c are the constants that can be determined from known viscosities at certain temperature [37].

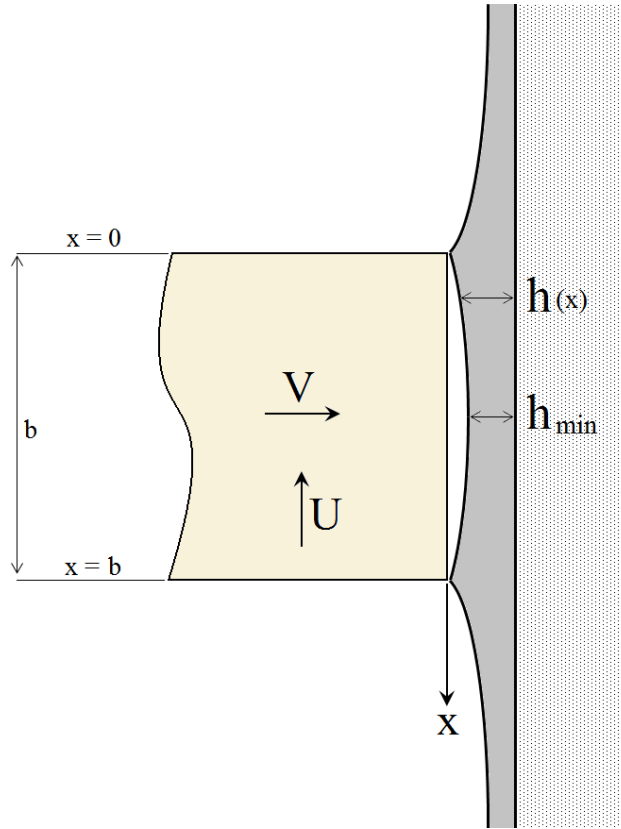


Figure 2.16 Cross section of the oil film between the piston ring and cylinder liner

During an engine cycle, the piston ring face is always in contact with oil film on the cylinder liner. Depending on oil film thickness, there are three distinct regions of piston ring lubrication: boundary, mixed and hydrodynamics [38]. When there is enough oil film to avoid surface to surface contact, the lubrication is in the hydrodynamic region. When the oil film is not thick enough to avoid surface to surface contact, the lubrication is in the boundary regime. The intermediate regime between the hydrodynamics and boundary lubrication is called mixed lubrication.

The oil film development between the ring face and the cylinder liner for hydrodynamic lubrication is modeled with Reynolds equation. An axisymmetric case of piston ring lubrication can be simplified to:

$$\frac{d}{dx} \left(\frac{h^3}{\mu} \frac{dp}{dx} \right) = -6U \frac{dh}{dx} + 12V \quad (2.5)$$

where:

P	Lubricant pressure
μ	Lubricant dynamic viscosity
h	Lubricant thickness
U	Ring Axial velocity
$V = \frac{dh}{dt}$	Ring Radial velocity

By assuming a uniform lubricant viscosity and integrating equation (2.5) and using the geometry of the ring face, the hydrodynamic pressure distribution and the minimum film thickness can be obtained.

A great deal of knowledge on the oil film thickness between the rings and the liner and on the piston can be modeled using the above relations. Reduction of oil consumption is required to satisfy three factors that currently govern the development of automotive engines: utilization of hydrocarbon resources, protection of the environment, and customer satisfaction. It is estimated that more than 50% of the engine oil consumption in automotive engines is from the piston ring pack. Consequently, the investigation of oil transport mechanisms at the interface between piston and liner is of critical importance. The ring and groove geometry along with temperature and pressure conditions at the interface between piston and liner are the governing factors in oil flow [39].

2.12 Three dimensional gas flow analysis

The physics of ring-pack motion and gas flow are very complex. The study of piston ring pack's gas flow, not only can provide guidance for the design of piston ring, but also is the essential prerequisite to study the lubrication and friction performance of the cylinder piston ring system.

Since it is difficult and extremely costly to conduct experiments on every series of engines to check for the blow-by and oil consumption, a CFD analysis can be performed on the ring pack to study the blow-by and oil consumption characteristics.

There have been numerous models to analyze the gas flow in cylinder kit assembly. They all suffer from simplifications that are forced because of the level of complexity in modeling the ring pack. Conventional numerical models that performs calculations in two-dimensional domain, proved to be only adequate for ring-pack design of the last decades. The need to accurately calculate ring pack design has been increased recently due to higher demands in market place for more powerful, more efficient with less emission engines. This has led the engineers to utilize newer models that take into consideration the three-dimensional effects which have become available due to recent advances in computational technology.

RINGPAK [40] by Ricardo software is an advanced two-dimensional simulation package for predicting ring pack dynamics, lubrication and gas flow for optimization of the ring pack that is based around advanced lubrication, gas and ring dynamic models. Sealing calculations can be performed based upon detailed gas flow analysis through the ring pack to predict blow-by and blow-back values. In its methodology, RINGPAK forms an interconnected system of gas volumes where the gas flow between these volumes is controlled by either the ring motion or by the conformability of the rings to the liner body during deformation. RINGPAK includes two flow models, one based upon isentropic conditions and the other based upon compressible isothermal flow. Each flow model can either be selected explicitly or left to be decide based upon flow parameters.

AVL (Advanced simulation Technologies) [1] is another independent company for the development of powertrain systems as well as instrumentation and test systems. They provide advance simulation tools thorough various softwares such as AVL BOOST, CRUISE and FIRE. They are capable of modeling injection nozzle flow, multi-phase flow. AVL BOOST and AVL FIRE® are used to obtain thermodynamics and combustion/emission development of internal combustion engines. Development and optimization of aftertreatment systems is done by AVL BOOST which is among other available 1D aftertreatment simulation software.

Ricardo and AVL are both commercial softwares that the availability of the details of their methodology are very limited. Therefore, a direct comparison between their results and the result of this study cannot be established.

CASE (Cylinder Kit Analysis System for Engines) [41] is a comprehensive simulation tool for ring-pack and piston dynamics analysis developed by Mid-Michigan Research LLC. It consists of two main parts. CASE-Piston uses parametric inputs data to auto generate a FEA (Finite Element Analysis) model that simulates the piston dynamics including its deformation. The CASE-RING is used for ring pack dynamics, including the ring axial and radial motion as well as twist. The code also predicts tribological phenomena between the rings and their interacting counterparts. Prediction of blow-by is determined by using orifice-volume method where the gas flow is assumed adiabatic and following perfect gas law. A discharge coefficient is designated to each ring to model the loss associated with the flow passing an orifice. Pressure (P) and Temperature (T) before and after the ring is shown in Figure 2.17 . The flow passing the ring gap (dW/dt) depends on the gap area (A_1).

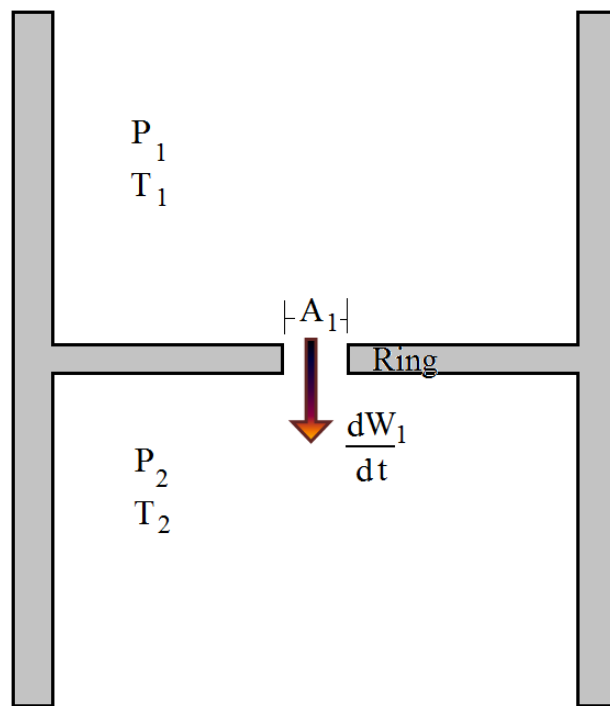


Figure 2.17 Flow of the gas through the ring end gap using orifice-volume method

2.13 Previous efforts

Since the middle of the 20th century many researchers have been trying to use numerical models to describe the physics of a ring pack. Engineers have studied the phenomenon of oil consumption and blow-by in a piston ring pack. This phenomenon has been studied from various points of view. Some have studied the phenomenon through experiments and developed models for blow-by and others have developed models based on the physics involved. Some have incorporated the effects of the shape of the rings on blow-by and gas flow through the piston ring pack [42].

In this section we consider the major developments in understanding the governing physics of the Internal combustion engines throughout the history.

In 1960, Furuhashi [43] developed a transient hydrodynamic lubrication model based on the one-dimensional solution of the Reynolds equation for a piston ring and compared the theoretical results with the experiment. In their work, they compared their gas transport model with the existing labyrinth model.

There have been a number of ring twist models. Ruddy et. al. [44, 45] studied the influence of ring twist on ring/liner lubrication. They addressed the importance of the contact point between rings and their grooves and found some interesting phenomena related to ring twist such as possible ring flutter if the contact point of the ring and its groove is at outside edge.

In 1979, Dowson and Ruddy et al [44, 46] proposed a 1D lubrication model and calculated the hydrodynamic friction, film thickness and the oil transport by including the influence of the ring dynamics and the ring twist for a ring.

Namazian and Heywood [47] employed orifice flow to model the flow into and out of the crevice regions between the piston, piston rings and cylinder wall. They used their model to understand the relation between the gas flow and unburned hydrocarbon emission and found possible sources of unburned hydrocarbons in the exhaust of spark-ignition engines,

Chucholowski et al. [48] and Kornprobst et al. [49] were the first scientists to develop a 2D simulation model of the entire cylinder-kit assembly. They employed the Reynolds equation to

determine the radial oil film thickness. They were able to include the effect of piston ring dynamics and gas dynamics in their results.

Tian et al. [17, 18, 50, 51] used analytical equation of low-Reynolds-number flow to accurately model the dynamic behavior of ring packs such as ring flutter, ring collapse, piston dynamics and their influence on gas flow and oil consumption. They developed a ring-dynamics and gas-flow model to study ring/groove contact, blow-by, and the influence of ring static twist and keystone ring/groove configurations. Their model was able to resolve ring flutter and gas blow-by, as well as ring axial and angular position, oil film thickness and hydrocarbon emission. The static twist angles were predicted and verified by a 2.0 liter four cylinder gasoline engine.

Chung [35] studied the wear models of a fire ring in a piston cylinder and compared the results with the available experimental data of a Diesel engine. They found that the specific wear rate at steady state drawn from their analysis corresponds to the maximum value of the wear coefficient observed in other experimental studies.

Dunaevsky et. al. [52, 53] employed a FEA method to study the mechanical and geometrical parameters of a split ring which affect the twist of the ring during the installation in the cylinder bore, and the calculated magnitude of this twist along the ring circumference. They were able to predict the inter-ring gas pressures and blow-by in a diesel engine analytically and compare their results with the experimental data measured at three engine speeds with RINGPAK software.

In 1997 Ejakov et al. [54] simulated the ring pack kinematics and gas dynamics for a deactivated cylinder. Later in 1998, Ejakov et.al. [16] developed a comprehensive computer program that includes a 3-dimensional beam model of a piston ring. Based on ring cross sectional properties, ring tension, pressure load above and below the ring, friction force and inertia force, the model predicts axial displacement, radial displacement, bend angle and twist angle of the ring over an engine cycle for any arbitrary ring cross section and groove geometry.

Liang Liu [55] and his coworkers employed an analytical tool to study three-dimensional (3D) ring-bore and ring-groove interactions for piston rings. The structural response of the ring is modeled with 3D finite element beam method with given free shape and the geometry of the cross-

section.

In 2007 Hronza and Bell [56] introduced a 2D-CFD model for a piston ring that takes into account the hydrodynamic lubrication, oil transport and radial ring dynamics. They were able to model the oil distribution in leading and trailing areas surrounding the piston ring by including the effects of the surface tension and wetting angles.

Oil film outside the lubrication gap has been studied by Felter [57] and Shahmohamadi et al. [58], where they used different methods. Felter employed a 2D free surface model based on the Navier-Stokes equations while Shahmohamadi exploited an isothermal 2-phase 2D CFD model of the lubrication gap between the ring running face and liner with a high degree of spatial discretization.

Veettil and Shi [42] described a CFD analysis where the region between the compression chamber and the skirt and between the piston (including the rings) and the cylinder liner is considered. In their study the effects of the position of the rings in the grooves and the position of the end gaps on blow-by and oil consumption was studied using commercially available CFD software. Ring twist was excluded from their model and rings were assumed to be either at the bottom, at the top or at the middle of the ring groove.

Jiang et. al. [59] investigated a three-dimensional EHD (ElastoHydroDynamic) lubrication and wear loss of piston ring-cylinder liner components for five rings in the firing diesel engine by using VC++ programs. The gas blow-by, along other engine parameters were all considered in the EHD lubrication analysis algorithm. The inter-ring pressure and the blow-by of ring gap in a working cycle were obtained by solving the first-order differential equations using Runge-Kutta method. Their model is comprised of modified average Reynolds equation adopted to simulate EHD lubrication. They assumed the gas is unsteady and adiabatic and follows the state equation of ideal gas. They found that the gas pressure of the inter-ring decreases from the top of the cylinder to the bottom of the cylinder liner and that the gas blow-by of the first piston ring gap is larger than that of other rings.

In 2015 Olivia et. al. [60] showed the possibilities to do a CFD analysis of the gas flow through

ring pack in an engine in the hope of minimizing the blow-by. A 3D approach was proposed however due to the difficulties in analyzing the full geometry, a 2D presentation of the geometry were investigated. They used a 1-D tool to adjust their CFD method by adjusting the leakage of each ring with respect to its groove sides and the influence of ring end gaps were compensated with adjusted axial ring motion.

Cheng et. al. [61] developed a robust three-dimensional piston ring model using finite element method with eight-node hexahedral elements that predicts the piston ring conformability with the cylinder wall as well as the separation gap between the interfaces. In addition to the radial interaction between the ring front face and the cylinder wall, the model also predicts the ring axial lift, twist, and contact forces between the ring sides and the groove sides along the circumferential direction simultaneously [61]. In this way, gas flow area around the entire ring can be accounted and coupled for gas dynamics and ring dynamics analysis [62]. This can be good for oil consumption and wear prediction as well [63]. A "Penalty method" [64] was employed to solve the non-linear contact problem. Finally A positive twisted scraper second ring with negative ovality is used as an example showing the result of the model (see Figure 2.18).

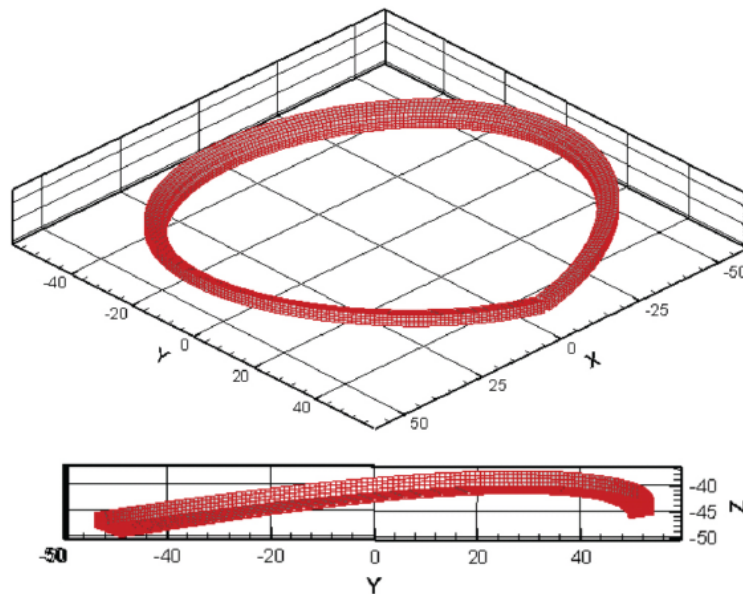


Figure 2.18 Calculated geometry of a deformed (twisted) Piston ring

In 2016, Lyubarskyy and Bartel [65] developed a 2D-CFD model of a piston assembly to analyze the mass transport through the piston-liner crevices of a diesel engine. The asperity contact and the boundary friction were used via elastic-plastic contact model and an analytical approach is implemented to consider the mass-flow through the ring gaps allowing the estimation of inter-ring pressures and blow-by into the crankcase.

In summary it can be asserted that the majority of the existing simulation procedures are based on 2D-CFD methods that employ the averaged Reynolds equations. Although CFD methods can provide very accurate result, However, they are only available in conceptual approached due to the complexity of the implementation [65]. Therefore, the focus in this study is to diminish the complexities of the 3D-CFD models within an acceptable range and solve the flow inside the ring pack using a 3D-CFD method.

CHAPTER 3

DEVELOPMENT OF A LINK PROGRAM

3.1 Introduction

Among the available Internal combustion engine simulation programs, CASE [41] has been considered a prominent modeling tools in the industry. The geometrical information of the simulated engine, required by CASE is enough to create the geometry of the ring pack. In this chapter, the development of a program that can construct a three dimensional geometry of the cylinder kit assembly is discussed. The strategy in approaching the problem is divided into two main parts. First, a *Link* program is introduced to import the CASE input file and create a framework that could be accepted by a CFD solver. Second, a CFD solver is chosen and properly set up to solve the domain of the problem.

3.2 LINK program

The main purpose of the link program is to create the necessary files for completing a CFD solution. It uses the same input structure format as the CASE program, and can be easily implemented into CASE as a subroutine. Simulations performed by the CASE programs are handled by a set of input *data lines* and files that specify the geometrical and operational information of the engine. Some data lines are required while others can be optional. Input data lines may be in any order in the data file and are considered as *input file* to the CASE program. More information about CASE program can be found in [66].

Additionally, the created output files are required to follow a standard format to give flexibility in choosing the CFD solver. The “Link” program creates the geometry of the cylinder kit through a set of input data lines and creates a geometry file in STL (STereoLithography) format [67]. It also generates necessary additional files to set initial and boundary conditions to be used in the

CFD solver.

In the following sections, the mechanics of the “Link” program are described as well as the steps taken to create the geometry of a ring pack. The CASE’s input file is read by the Link program and the cylinder kit assembly geometry is created progressively.

3.2.1 Overview of the Geometry in STL format

An STL file is a triangular representation of a three dimensional surface geometry. The surface is broken down logically into a series of small triangles (facets). Each facet is described by a perpendicular direction and three points in a Cartesian coordinate system, representing the vertices (corners) of the triangle. An STL file consists of a list of facet data. Each facet is uniquely identified by a unit normal (a line perpendicular to the triangle with a length of 1.0) and by three vertices (corners). The normal and each vertex are specified by three coordinates each, so there is a total of 12 numbers stored for each facet [68].

Facet orientation: The facets define the surface of a three dimensional object. As such, each facet is part of the boundary between the interior and the exterior of the object. The orientation of the facets (which way is “out” and which way is “in”) is specified redundantly in two ways which must be consistent. First, the direction of the normal is outward. Second, the vertices are listed in counterclockwise order when looking at the object from the outside (right-hand rule [69]). These rules are illustrated in Figure 3.1.

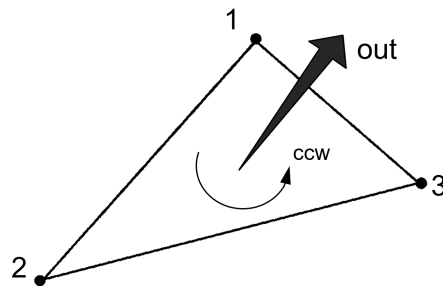


Figure 3.1 Orientation of a facet and its normal vector

Vertex-to-vertex rule: Each triangle must share two vertices with each of its adjacent triangles.

In other words, a vertex of one triangle cannot lie on the side of another. This is illustrated in Figure 3.2.

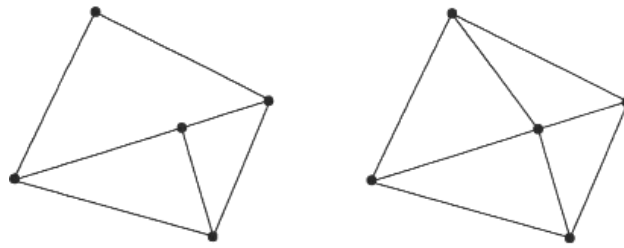


Figure 3.2 Vertex to vertex rule - the left figure is the violation of this rule

A 3D object can be represented by series of surfaces that could be broken down to triangles. As an example, a cube in an STL format will look as Figure 3.3.

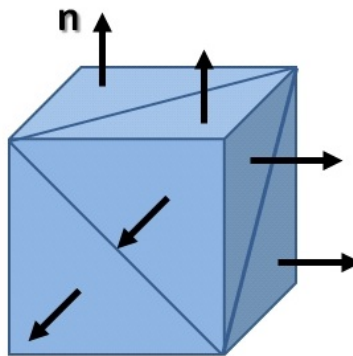


Figure 3.3 A cube represented in STL format

3.2.2 Geometry of Cylinder Kit Assembly in STL format

The geometry of the ring pack is constructed consecutively by first constructing the rings and the piston. The deformation of the rings due pressure and heat transfer load is calculated using an FEA analysis [70] that determines the flow passages between the ring and groove. This will require additional modification to the final STL file which is explained in section 3.2.3. Once all the components of the ring pack are created and assembled, the crevice regions between the piston, piston rings and cylinder liner is established. A typical geometry of a cylinder liner is shown in Figure 3.4. The clearances are exaggerated for a better view and the possible flow paths are shown with yellow arrows.

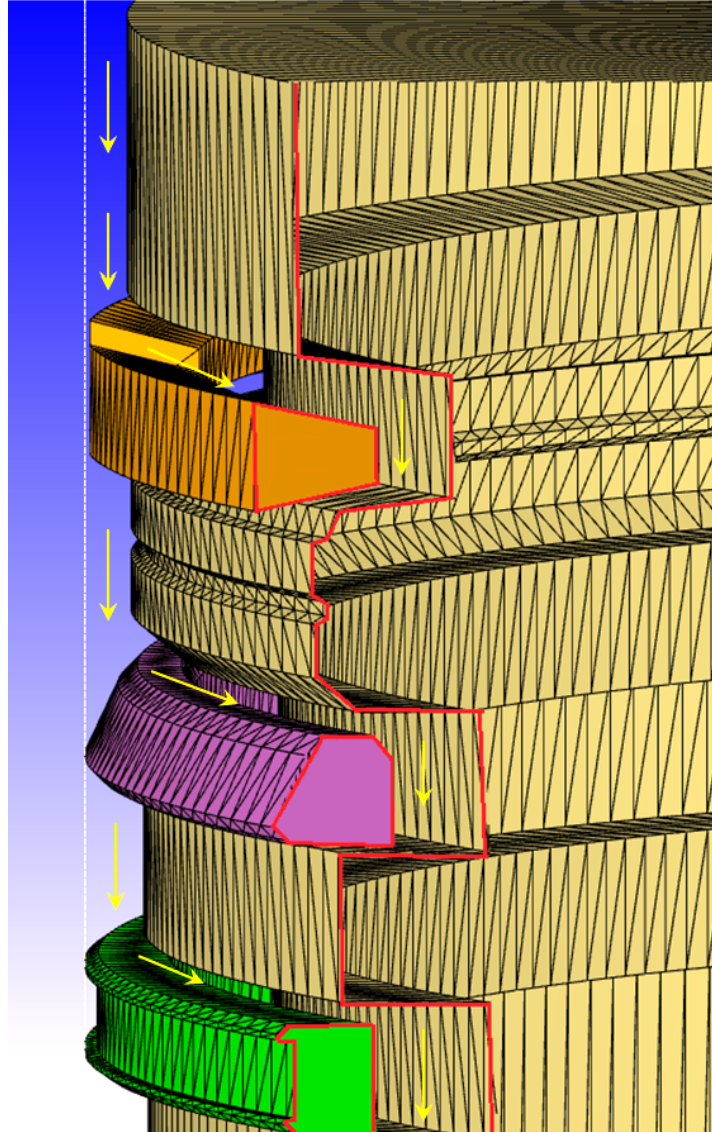


Figure 3.4 Geometry of cylinder-kit assembly in STL format

3.2.3 Modification of surface

Two important criteria are met for a properly configured surface in STL format. While the surface geometry needs to represent the shape of the objects in the simulation there are no restrictions on the size or skewness of the triangles that constitute the surface. Several types of surface defects can cause problems as listed below.

1- Overlap surfaces

2- Overlap points

When whole or partial surfaces of two components overlap, the overlapping part is introduced twice. In this case (*Overlap Surfaces*), two surfaces are representing the same physical surface that no flow exists in between. This situation happens when the ring side surface comes in contact with the cylinder liner causing a complete seal. A cross section of this situation is shown in Figure 3.5 . Therefore, the overlapping surface is removed since no flow passes through.

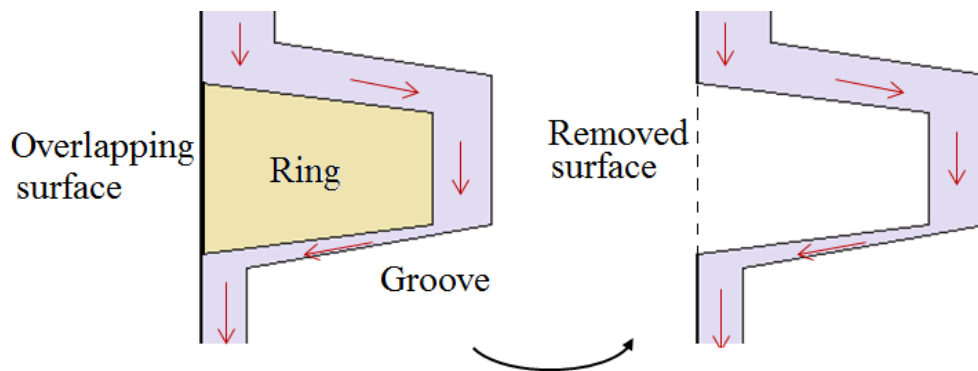


Figure 3.5 Example of overlap surfaces condition

When one surface intersects another surface with a line, the *Overlap points* condition occurs. This situation mostly happens when the ring is twisted and the sharp edge of the ring is resting on the cylinder liner representing the seal. To remedy this situation, an infinitesimal surface is introduced that is called *Ghost surface*. This will create a cross section with no *Overlap surfaces* which has to be removed as discussed earlier.

A scenario that the overlap point condition occurs, is illustrated in Figure 3.6. The wetted area is shown by green lines. The ring meets the cylinder liner at only one point as shown in part (a) and the ghost surface is depicted in part (b) of Figure 3.6.

3.2.4 Ring construction

The ring is constructed by rotating the cross section about the center of the piston axis. The cross section at each angle of the circumference can be different based on the gap distance between

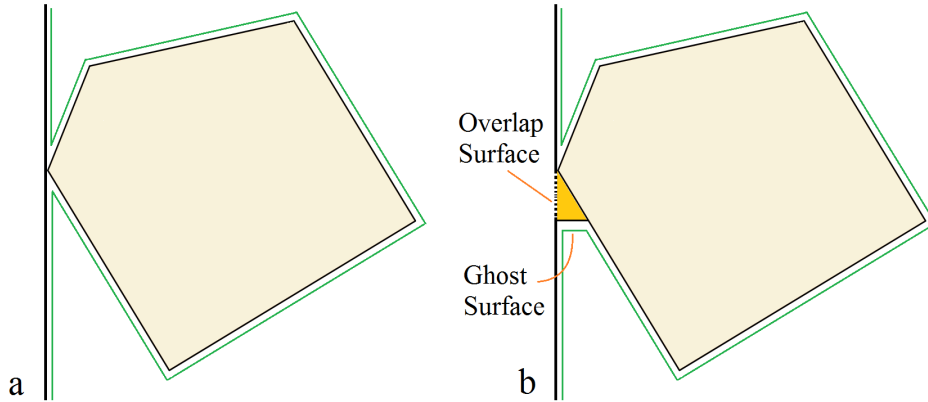


Figure 3.6 Example of overlap points condition

the cylinder liner and the ring. If the gap distance is zero, the ring is touching the cylinder liner and the cross section will require some surface modification applied to the overlapping surfaces with cylinder liner. This will change the cross section of the ring at that location. If the ring is not touching the liner, the cross section of the ring at that circumference angle will remain unchanged.

The top view of a ring installed in the bore is illustrated in Figure 3.7. As shown in this figure, the circumferential sealing of the ring only occurs at certain location across the circumference that are colored by light blue.

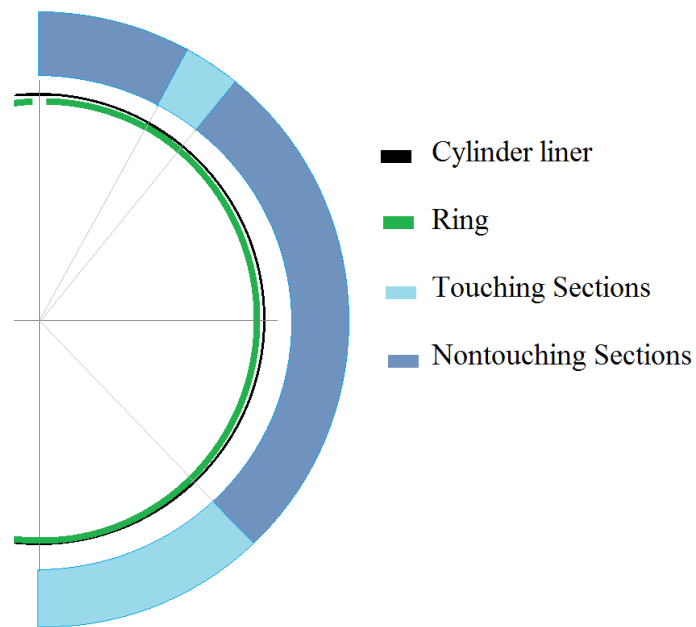


Figure 3.7 Top view of a installed piston ring in a bore

In order to understand the details of the ring construction in Link program, a schematic view of the slice of a typical piston ring and cylinder liner is shown in Figure 3.8. The focus of this figure is to show a sequence of cross sections that are either touching or not touching the cylinder liner. The different arrangements of the cross sections will form different types of ring elements. A ring element is described as the segment of the ring confined between two cross sections. The cross sections are marked by T or N if they are touching or not touching the cylinder liner, respectively.

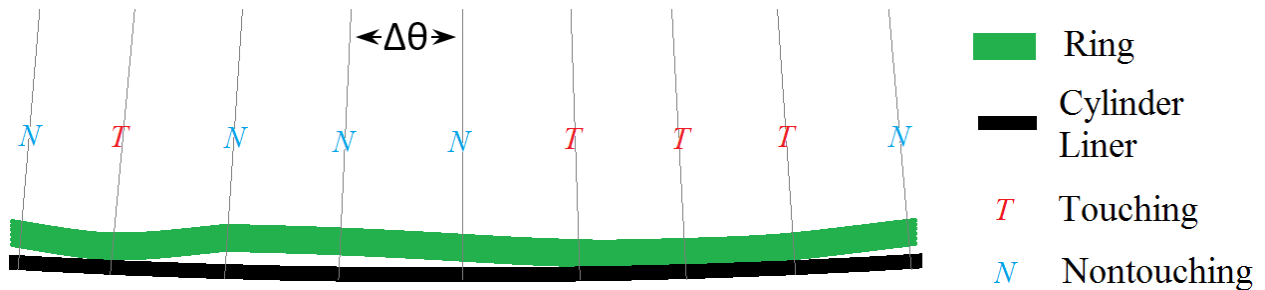


Figure 3.8 Top view of a slice of a piston ring installed in a bore

To understand how a cross section is modified when it is touching the liner, a ring with an arbitrary cross section as depicted in Figure 3.9 is assumed. It is assumed that the ring comes in contact with the liner only at one point. Therefore, the cross section of the ring at the touching point will get a new shape according to the *Overlap points* rule (see Figure 3.10).

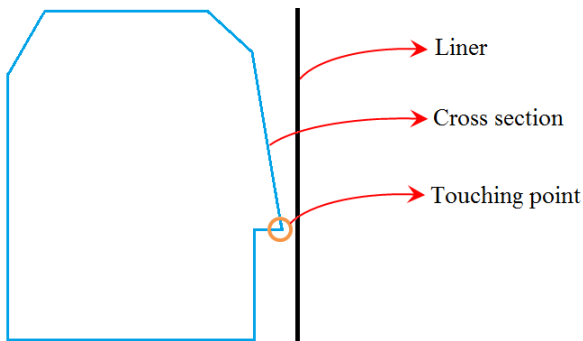


Figure 3.9 An arbitrary non-touching ring cross section

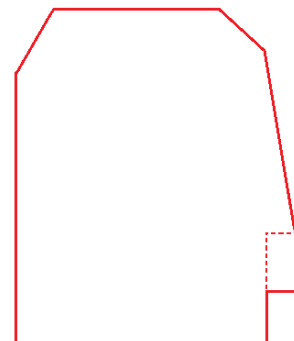


Figure 3.10 An arbitrary touching ring cross section

Depending on the condition of the cross section (touching or not touching the liner) four different types of elements are possible. For the cross section of Figure 3.9 all the possible ring elements

are shown in Figure 3.11. These elements are named by their side cross section type. For example, a TT element is an element with both sides touching the cylinder liner.

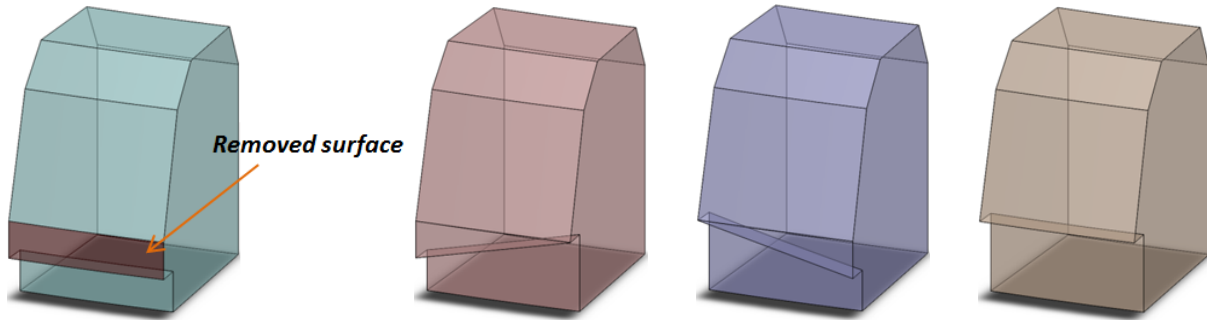


Figure 3.11 Piston ring element types. From left to right 1) TT 2) TN 3) NT 4) NN

Using the ring element concept, the piston ring slice that were shown in Figure 3.8, can be constructed with the above procedure. The final geometry of the ring will look like Figure 3.12.

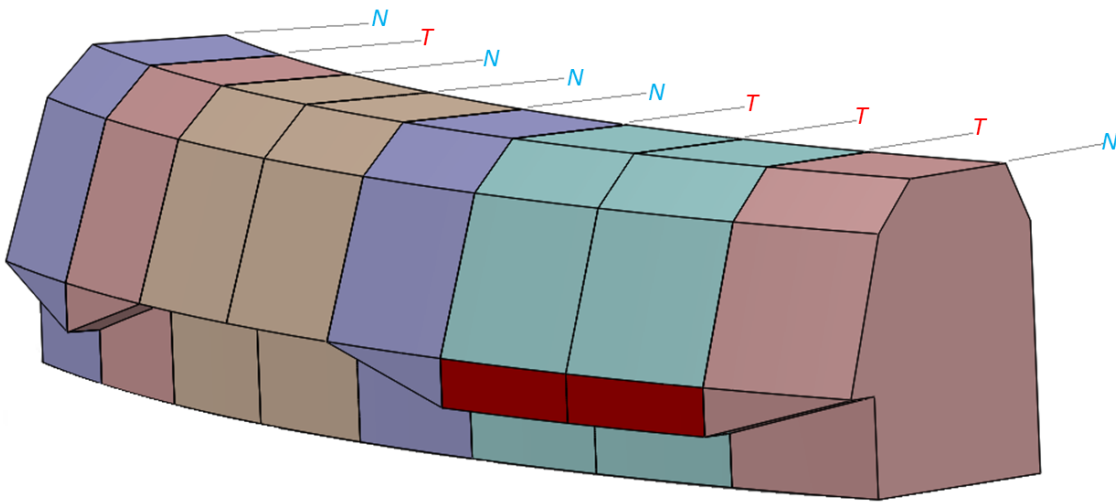


Figure 3.12 Front view of a slice of a piston ring constructed by ring element concept

The series of the cross sections that forms the piston ring in the mentioned slice is summarized in Figure 3.13.

3.2.5 Piston construction

Piston is constructed by first creating a 2D presentation of the grooves and skirt as shown in Figure 3.14 and then rotating about the center axis of the piston. It is assumed that the piston is a cylindrical shape with one axis of symmetry. The front view of a typical piston created in STL format is shown in Figure 3.15.

Pistons can be prone to axial and radial deformations due to piston acceleration and gas pressure forces during engine operation [71]. In the presence of asymmetric structural features such as translot, steel strut and pin boss, thermal deformation analysis becomes essential in piston design [72]. If the deformation of the piston is known, it can be easily modeled by modifying the cross section of the piston at each circumference angle. In this study the deformation of the piston is not considered.

3.2.6 Cylinder Liner construction

The cylinder liner is constructed in the same way the piston is created with the consideration of removal of the overlap regions. As mentioned earlier, a piston ring outer surface might come in contact with some part of the cylinder liner. Therefore, the shared surface is removed because no flow passes between the surfaces.

In addition to the manufacturing tolerances that can cause the liner to deviate from this ideal condition, the liner will deviate from the ideal geometry as a result of thermal and mechanical

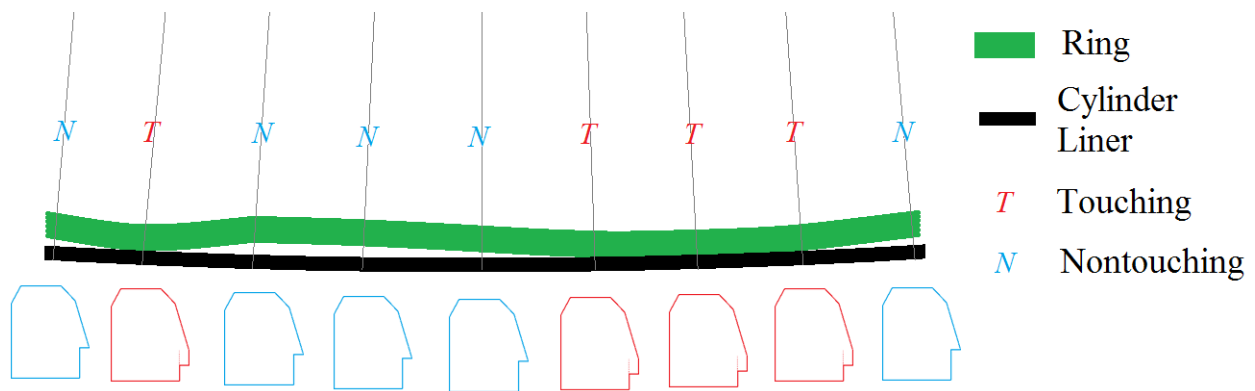


Figure 3.13 Different cross sections of the portion of a piston ring

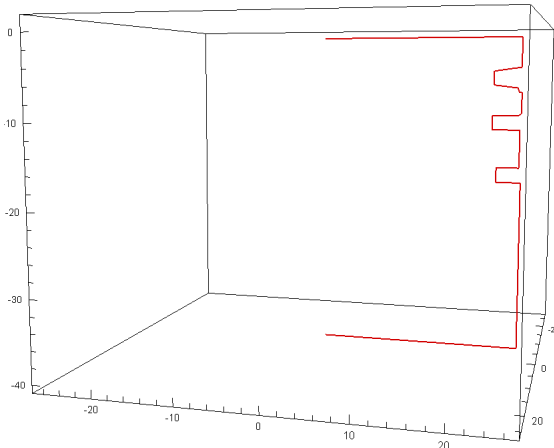


Figure 3.14 Cross section of a piston

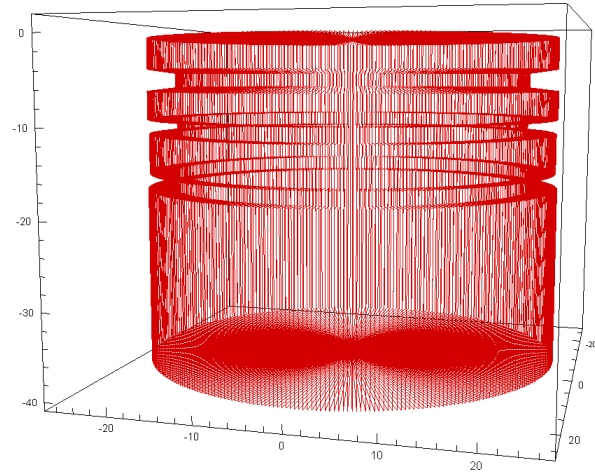


Figure 3.15 Constructed piston in STL format

loads during engine operation. The loads acting on the liner come from a variety of conditions, for example [73]:

- Assembly of the cylinder head and cylinder head gasket (assembly loads).
- Thermal expansion variations between the cylinder block and cylinder head.
- Gas pressure during fired operation.
- Temperature gradients during expansion.

The deformation of the cylinder liner is treated in a similar manner to piston as explained earlier. In this study the deformation of the cylinder liner is not examined.

3.2.7 Final Assembly of the geometry

After the completion of the construction of the rings, cylinder liner and pistons; they are assembled together to form the geometry of the problem. A typical completed cylinder kit assembly is shown in Figure 3.16. This geometry is presented in STL format, surface modifications are applied and the overlapping regions are removed. The surfaces are colored differently for a better view and the red lines show the cut plane.

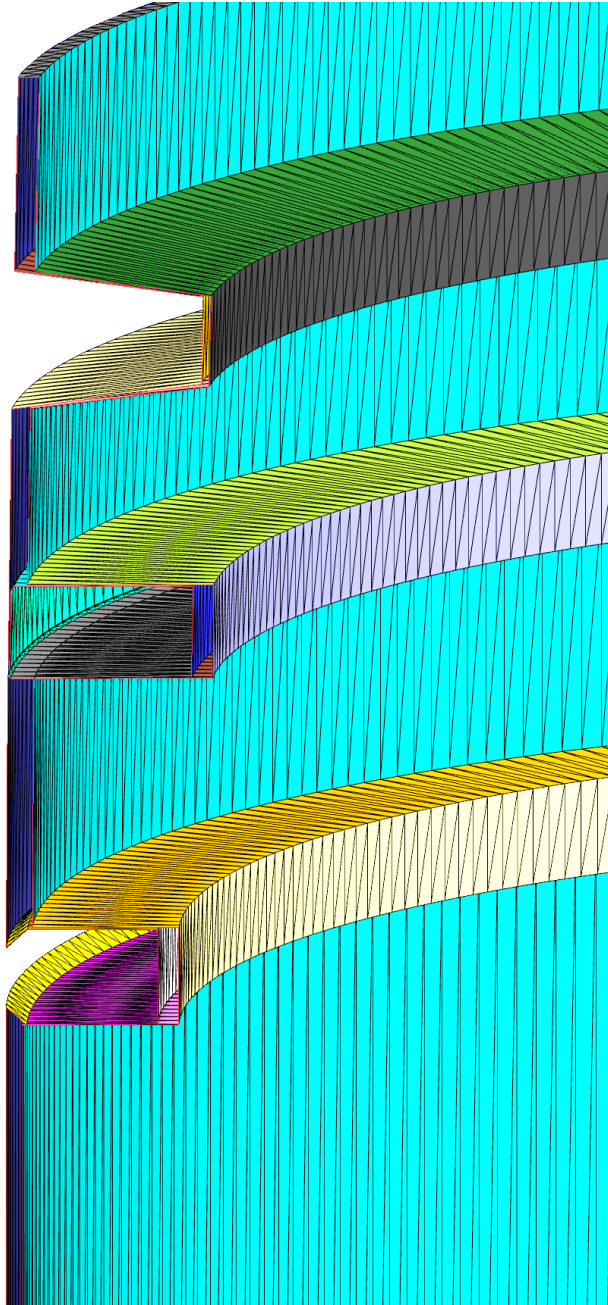


Figure 3.16 3D representation of a completed cylinder kit assembly

3.3 Simulation method

CONVERGE™ [74] is utilized as the CFD solver. CONVERGE is a CFD (Computational Fluid Dynamics) program that eliminates the grid generation process and automatically creates a per-

fectly orthogonal, structured grid at runtime based on simple, user-defined grid control parameters. This grid generation method completely eliminates the need to manually generate a grid. CONVERGE was developed by engine simulation experts and is straightforward to use for both engine and non-engine simulations. Moreover, it is available in the cloud and can be easily set up to run multiple cases simultaneously.

The flow through the piston ring pack is very complex due to different geometrical influences. The gaps between the liner and rings are in the range of few microns, while the gap between the liner and the piston skirt or crown is in the millimeter range. The large difference in the order of the magnitudes of the geometry lengths introduces huge challenges in meshing the domain. Also, the high pressure difference between the combustion chamber and crankcase requires a very small time step to resolve the flow accurately. Additionally, the movement of the ring in its groove and the thermal deformation of the geometry greatly impact the flow through ring pack and introduce another level of difficulty to solve the flow. On one hand, there are up to 100 orders of magnitude difference in the smallest and largest distance in the calculating area which contributes to various characteristic lengths. On the other hand, during the high pressure period of the combustion cycle, the pressure gradient is large enough to create a high velocity flow in the small gaps surrounding piston rings. The above situations introduce major challenges for meshing process that requires high spatial and temporal discretization, respectively.

There are different approaches to overcome the above challenges and each, have their own assumptions and approximations. The two-dimensional representation of the geometry is first chosen as the first step to model the flow in a ring pack. The possibility of using a very fine mesh around the area of interest, while demanding few computational resources is a significant advantage in this approach. Yet, the 3D effects such as circumferential flow or ring end gap effect on flow field cannot be captured with this model. Another approach would be a complete 3D model which provides a comprehensive consideration of the circumferential effect on the flow field which would require a high number of computational cells if accurate solution of the flow field is desired.

In this study, we first create the 3D geometry of a cylinder-kit using the Link program and then

cut a narrow section of it to generate the 2D representation of the 3D geometry. The goal is to investigate the flow field in 2D and 3D and establish a framework to capture the 3D effects in a cylinder kit assembly.

3.4 Geometry of the proposed problem

A small-bore supercharged cylinder-kit assembly that operates in 2000 RPM is considered and the geometry of the problem is created in STL format by employing the Link program. The piston ring pack is comprised of a keystone, scraper and oil control rings that are allowed to be twisted. Piston ring twist is calculated using Cheng et al. method described in [20] while the first and third ring is assumed to be untwisted and seated on the lower surface of its groove, only the second ring twist is considered. The initial temperature of the surfaces of the ring pack, the inlet pressure trace and crank case pressures are assumed to be known and given. The dimension of the rings, grooves, piston skirt and the clearance between the cylinder liner and piston is shown in the Figure 3.17.

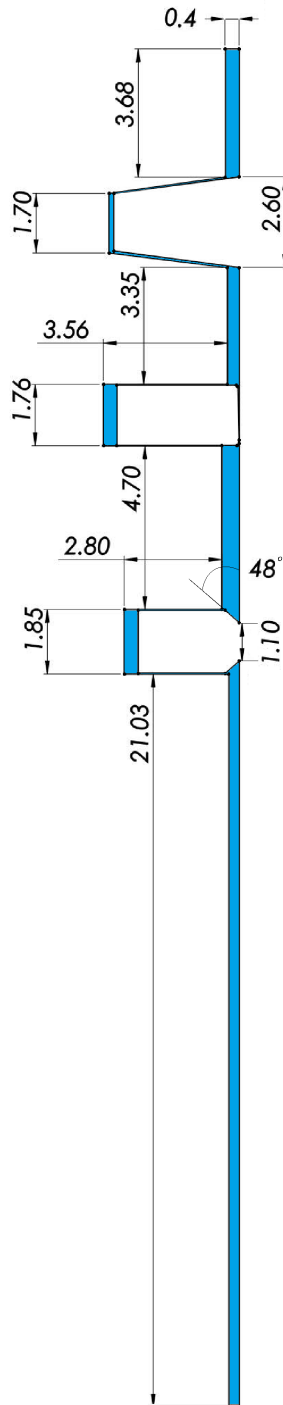


Figure 3.17 Cross section of the studied geometry (units are *mm*)

Since the flow simulation in the ring pack is performed in 2D and 3D separately; to make a comparison between the simulated geometries, the 2D cut and 3D representations of the studied cylinder kit are shown in Figures 3.18 and 3.19.

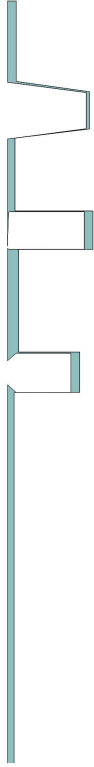


Figure 3.18 2D-cut of the cylinder-kit

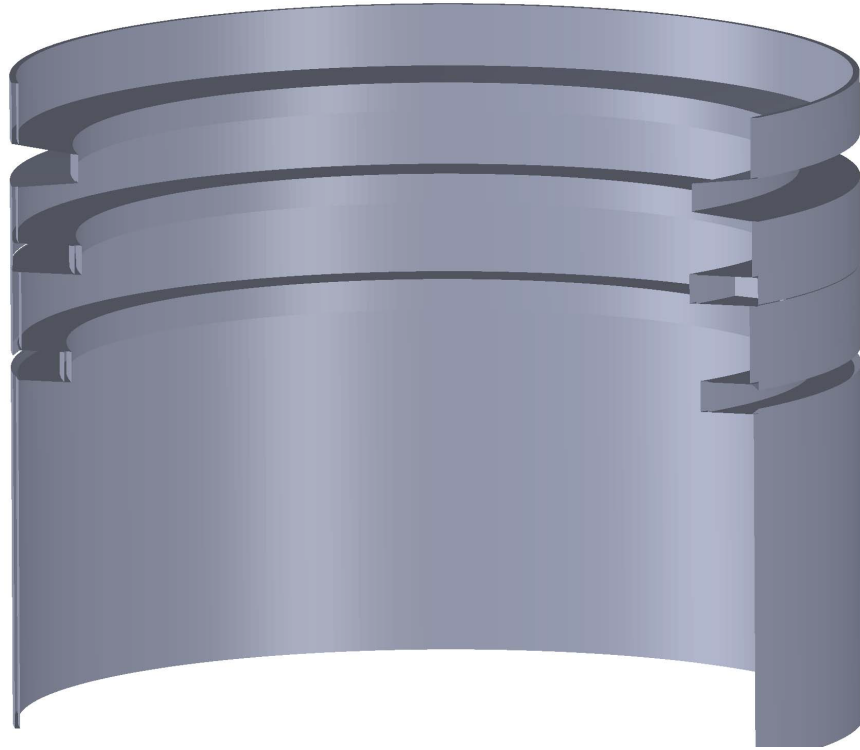


Figure 3.19 Complete 3D cylinder-kit geometry (sectioned)

In the following sections, the available tools and the proposed assumptions as well as the governing equations and boundary conditions are discussed alongside with the grid study for 2D and 3D geometries.

3.4.1 In-cylinder pressure "Binning"

A four-stroke engine rotates 720 crank angle degrees to complete its cycle. While the combustion chamber pressure varies throughout the cycle, it nearly follows an identical behavior for each cycle of the engine. Here, the pressure trace curve is assumed to be known for each RPM and depicted in Figure 3.20. It is clear from the curve that the in-cylinder pressure is different for each crank

angle. Using a "Binning" concept, instead of changing the pressure for each crank angle degree of the cycle, the pressure curve is divided into 10 bins with different sizes as shown in Figure 3.21. For crank angles falling in the same bin, the mean average of the all pressures inside that bin is considered as the in-cylinder pressure of those crank angles. For example, the in-cylinder pressure pertaining to the first bin ranges from 0.0 to 5.1364 bars and encompasses the crank angles from 1 to 300 and 430 to 720.

On one hand, by employing the above binning procedure, the calculated flow field is automatically assumed to hold for all the crank angles that fall in the same bin regardless of the discrepancy between the pressure associated with the crank angle from the pressure trace graph and the averaged bin pressure. This will result in fewer simulations to model the flow for the complete cycle. On the other hand, because of the piston ring twist, the geometry of the problem might be different for the same bin pressure and therefore, the calculated flow field does not hold true for all the crank angles of the same bin pressure. To overcome this situation, a new simulation is added with the same bin pressure but different geometries. In other words, the total number of simulations to model the complete cycle is increased to accommodate for the geometry change within the bin.

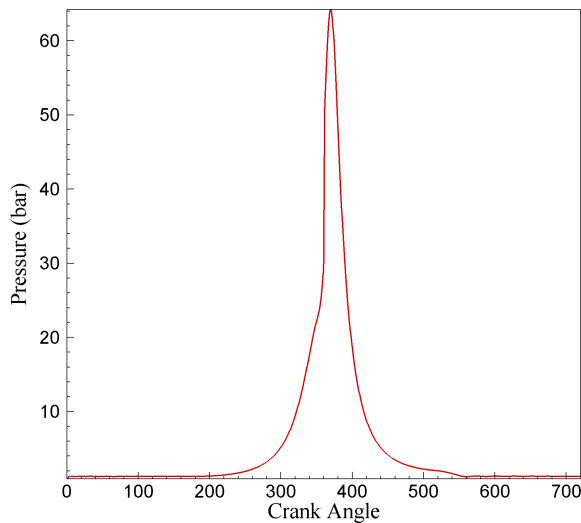


Figure 3.20 Pressure trace curve

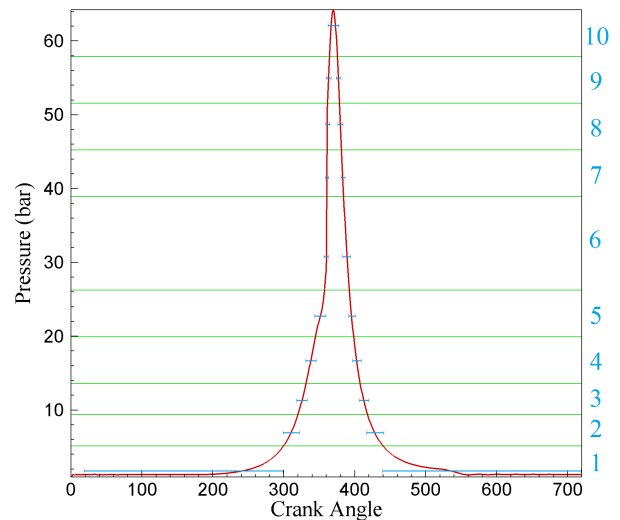


Figure 3.21 Binned pressure trace

In conclusion, The accuracy of the complete cycle results depends on the resolution of the in-cylinder binning width and variation in ring twist and deformation.

3.4.2 Governing equations

The flow is assumed to be quasi-steady for each bin pressure and the domain of the problem is solved for a constant inlet pressure. Using the pressure binning approximation, one can simulate 10+ different flow fields to resolve the flow for the whole cycle. These cases include the 10 in-cylinder pressure binning as well as the variation of the geometry within the same bin pressure.

Transient and steady solver is available in CONVERGE. While these solvers are similar in formulation they have notable differences.

$$\frac{\partial \rho \Phi}{\partial t} + \frac{\partial \rho u_i \Phi}{\partial x_i} = \frac{\partial}{\partial x_i} \left(\rho D \frac{\partial \Phi}{\partial x_i} \right) \quad , \quad \frac{\partial \rho u_i \Phi}{\partial x_i} = \left(\rho D \frac{\partial \Phi}{\partial x_i} \right) \quad (3.1)$$

where ρ is density, u_i is velocity, D is diffusion coefficient and ϕ is any transported quantity.

Although a time term has been removed from the transport equation in steady-state (equation on the right of 3.1), a pseudo time-step is used when solving the transport equations to aid in numerical convergence. The size of the pseudo time-step for each cycle is dictated by the maximum CFL (Courant–Friedrichs–Lewy) numbers which is explained in the next paragraph. Because a pseudo time-step is introduced, the steady-state solver works in a conceptually similar manner as the transient solver, however, the steady-state solver is not required to be time-accurate while it proceeds in pseudo time to a steady solution [74]. This introduces numerical instability in steady-state solution and therefore the transient solver is used instead. The transient solver that is implemented in CONVERGE employs PISO algorithm (Pressure Implicit with Splitting of Operator) which is explained later in this section [74].

The CFL numbers estimate the number of cells through which the related quantity will move in a single time-step. A higher number generally yields a less computationally expensive simulation. The convective CFL number, the speed of sound CFL number, and the diffusive CFL number are given respectively as [74]:

$$cfl_u = u \frac{\Delta t}{\Delta x} \quad (3.2)$$

$$cfl_{mach} = c \frac{\Delta t}{\Delta x} \quad (3.3)$$

$$cfl_v = v \frac{\Delta t}{\Delta x} \quad (3.4)$$

where Δt is the time-step, Δx is the grid spacing, u is the cell velocity, c is the speed of sound, and v is the viscosity.

The compressible equations for mass and momentum transport are given by:

$$\frac{\partial \rho}{\partial t} + \frac{\partial \rho u_i}{\partial x_i} = S \quad (3.5)$$

and

$$\frac{\partial \rho u_i}{\partial t} + \frac{\partial \rho u_i u_j}{\partial x_j} = -\frac{\partial P}{\partial x_i} + \frac{\partial \sigma_{ij}}{\partial x_j} + S_i \quad (3.6)$$

Where the viscous stress tensor is given by:

$$\sigma_{ij} = \mu \left(\frac{\partial u_i}{\partial x_j} + \frac{\partial u_j}{\partial x_i} \right) + \left(\hat{\mu} - \frac{2}{3}\mu \right) \left(\frac{\partial u_k}{\partial x_k} \delta_{ij} \right) \quad (3.7)$$

In the above equations, u is velocity, ρ is density, S is the source term, P is pressure, μ is viscosity, $\hat{\mu}$ is the dilatational viscosity (set to zero), and δ_{ij} is the so-called Kronecker delta. Since the turbulent model is used the viscosity is replaced by the turbulent viscosity given by:

$$\mu_t = \mu + C_\mu \rho \frac{k^2}{\varepsilon} \quad (3.8)$$

where C_μ is a turbulence model constant, k is the turbulent kinetic energy, and ε is the turbulent dissipation.

The commonly used cubic equation of state (Redlich-Kwong) is utilized to couple the density, pressure and temperature equations:

$$P = \frac{RT}{v-b} + \frac{a}{v^2 + ubv + \omega b^2} \quad (3.9)$$

A more extensive explanation of the relation (3.9) can be found in [75].

The pressure is not calculated directly from the equation of state but instead is used indirectly in the PISO algorithm to ensure that the equation of state is satisfied. The PISO algorithm as implemented in CONVERGE starts with a predictor step where the momentum equation is solved.

After the predictor, a pressure equation is derived and solved, which leads to a correction, which is applied to the momentum equation. This process of correcting the momentum equation and re-solving can be repeated as many times as necessary to achieve the desired accuracy. After the momentum predictor and first corrector step have been completed, the other transport equations are solved in series. It is necessary to solve the mass and momentum equations together for the proper calculation of the pressure gradient in the momentum equation [74].

Energy equation is given by :

$$\frac{\partial \rho e}{\partial t} + \frac{\partial u_j \rho e}{\partial x_j} = -P \frac{\partial u_j}{\partial x_j} + \sigma_{ij} \frac{\partial u_i}{\partial x_j} + \frac{\partial}{\partial x_j} \left(K \frac{\partial T}{\partial x_j} \right) + \frac{\partial}{\partial x_j} \left(\rho D \sum_m h_m \frac{\partial Y_m}{\partial x_j} \right) + S \quad (3.10)$$

where ρ is density, Y_m is the mass fraction of species m , D is the mass diffusion coefficient, S is the source term, P is the pressure, e is the specific internal energy, K is the conductivity, h_m is the species enthalpy, σ_{ij} is the stress tensor, and T is temperature. The conductivity is replaced by turbulent conductivity given by:

$$K_t = K + c_p \frac{\mu_t}{Pr_t} \quad (3.11)$$

where Pr_t is the turbulent Prandtl number and μ_t is the turbulent viscosity.

Reynolds Averaged Navier-stokes (RANS) turbulence model of standard $k - \varepsilon$ is utilized to model the turbulency of the flow. Because of the existence of very small length scale in the flow domain, the LES (Large Eddy Simulation) turbulence model, can capture the flow details more accurately; however, due to its high computation cost it is not pursued in this study.

3.4.3 Boundary conditions

In CONVERGE each boundary, regardless of type, is assigned a boundary condition for the partial differential conservation equations as either Dirichlet (specified value) or Neumann (specified first derivative value). Mathematically, these boundary conditions are given as:

$$\phi = f(\text{Dirichlet}) \quad (3.12)$$

and

$$\frac{\partial \phi}{\partial x} = f(\text{Neuman}) \quad (3.13)$$

where ϕ is a solved quantity (e.g., pressure, energy, velocity, or species) and f is the specified value or specified derivative on the boundary.

A schematic view of the boundary conditions used in this problem is illustrated in Figure 3.22.

The fixed *wall* boundary condition is applied at cylinder liner, piston and rings surface. The velocity is assumed to be zero on the wall for momentum equations, hence no slip wall boundary condition (a.k.a. Dirichlet boundary type). However, since there are very small regions in the domain that has high Reynolds number the flow is not resolved down to the viscous sub-layer, a law-of-the-wall boundary condition is specified [74, 76]. There are three law-of-the-wall models available in CONVERGE: one for $k - \varepsilon$ turbulence models, and two for *LES* turbulence models. When a $k - \varepsilon$ turbulence model is used, the standard law-of-the-wall with turbulence is used [77]:

$$u^* = \begin{cases} \frac{1}{\kappa} \ln(Ey^+) & y^+ > 11.2 \\ y^+ & y^+ \leq 11.2 \end{cases} \quad (3.14)$$

where κ is the Von Karman constant (0.4187) and y^+ is defined in equation with C_μ being the model constant from $k - \varepsilon$ model

$$y^+ = \frac{y\rho u\tau}{\mu}, \quad u\tau = c_\mu \kappa \quad (3.15)$$

The heat transfer at the wall occurs by conduction which is a Dirichlet boundary type and is given by equation (3.16)

$$q = -k \frac{\partial T}{\partial x_i} = -k \frac{(T - T_w)}{(x - x_w)} \mathbf{n}_i \quad (3.16)$$

This boundary condition can be accurately applied when there is adequate near-wall resolution (i.e., the viscous sub-layer is resolved). Since the near-wall resolution is not adequate in this study, the law-of-the-wall temperature boundary condition is used which is given by:

$$k \frac{\partial T}{\partial x_i} = \frac{\mu_m c_p F (T_f - T_w)}{\text{Pr}_m y} \mathbf{n}_i \quad (3.17)$$

More information about the above parameters can be found in [78].

The *Inflow* boundary condition is applied at the Inlet of the cylinder kit assembly and *Outflow* at the outlet as shown in Figure 3.22. There are several types of Inflow boundary conditions available for the velocity equation: Dirichlet, Neumann, mass flow, pump, Normal Neumann, and average velocity. For the Outflow velocity boundary condition, the only options are Neumann, mass flow, and average velocity.

When the pressure Dirichlet value is specified and a Neumann condition for velocity, the velocity will adjust its magnitude and direction depending upon the values of pressure gradient in the vicinity. If the steady state solution is desired, the pressure at the inlet is set to the value according to the bin pressure and kept constant through the simulation. If the transient solution is demanded, a separate input file that contains the temporal variation of the pressure trace is created and CONVERGE will pick the pressure values from the new input file as the simulation marches in time.

There are two types of Inflow boundary conditions available for the energy equation: Dirichlet and Neumann. The recommended temperature boundary condition configuration is Dirichlet for the Inflow boundary and Neumann for the Outflow boundary.

The static temperature is determined from:

$$T_{static} = T_{global} \left(1.0 + \frac{\gamma - 1}{2} \frac{u_i^2}{\gamma RT} \right)^{-1} \quad (3.18)$$

where γ is the ratio of specific heats and R is the gas constant.

The temperature of the wall were set to 300 °K all around, as well as the temperature of the Inlet gas. The fluid is air and is assumed to consists of 77% Nitrogen and 23% Oxygen.

3.4.4 Grid generation

The grid generation method used by CONVERGE, eliminates the need to manually generate a grid and provides additional tools to manipulate it. Traditionally, boundary-fitted grids morph the

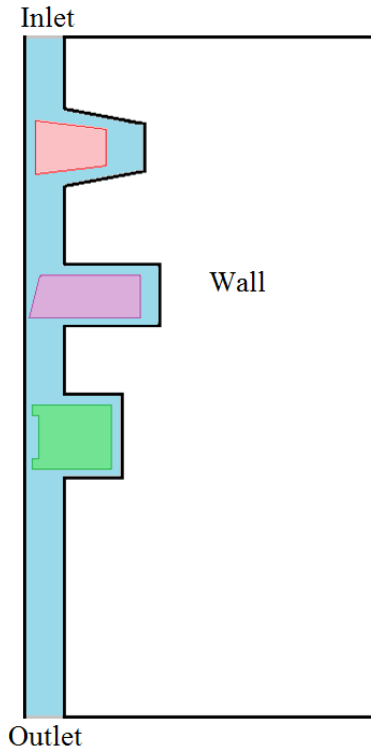


Figure 3.22 Schematic view of the boundary conditions

vertices and cells in the interior of the domain to conform to the shape of the geometry. Because of the disadvantages associated with this approach CONVERGE uses an improved boundary-fitted strategy that eliminates the need for computational grid to coincide with the geometry of interest. Also by creating orthogonal grid internally at runtime, the grid is allowed to adapt to the simulation by coarsening or refining through adaptive mesh refinement tool [74].

Grid size is established by setting dx , dy and dz to a known value in an input file. Fixed or time-dependent refinements (embedding) can be configured in the grid when and where it is needed especially for the situations where a finer resolution is critical to the accuracy and precision of the solution. For each section of the fixed embedding, a scaling parameter is set to indicate how many levels of embedding are used to refine that section of the domain. Each additional increment of the scaling value divides the dx , dy , and dz in half according to the equation given by:

$$dx_{embedded} = dx_{base} \times 2^{-(embedded_scale)} \quad (3.19)$$

An example of a grid system before and after embedding is shown in Figure 3.23 .

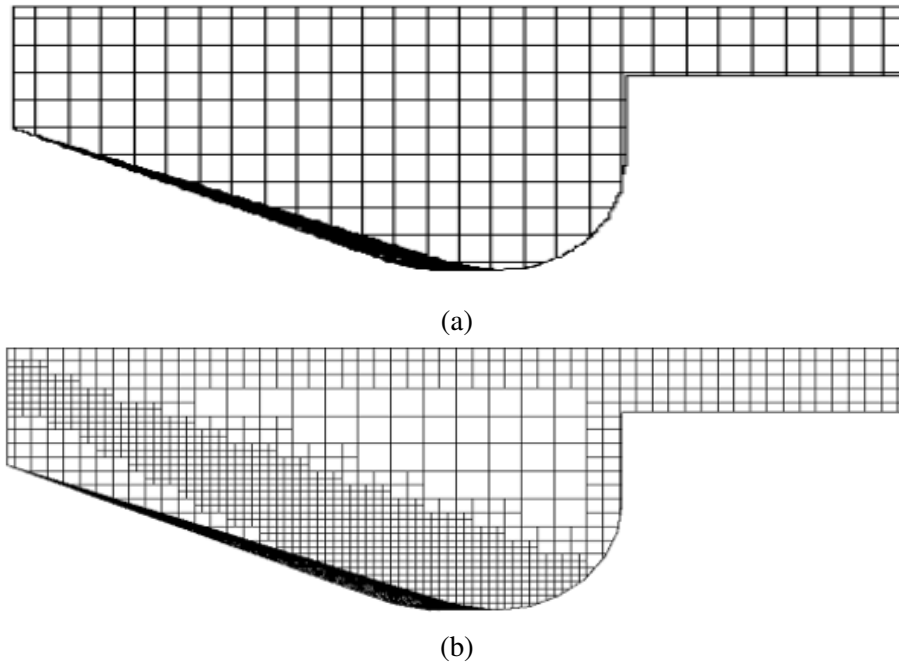


Figure 3.23 An example of grid embedding (a) before and (b) after

Another useful tool that automatically refines the grid based on fluctuating and moving conditions such as temperature or velocity is the Adaptive Mesh Refinement (AMR). This option is useful for using a highly refined grid to accurately simulate complex phenomena such as flame propagation or high-velocity flow without unnecessarily slowing the simulation with a globally refined grid.

3.4.4.1 2D and 3D Geometries grid

The most influential part of the solving a CFD problem is grid generating process. The number of cells dictates the simulation time and accuracy of the results. The simulation grid is generated internally in CONVERGE where various levels of the grid size are examined to compare the simulation time. Additionally, the grid is refined in locations close to the first ring because of the high pressure gradient by setting the embedding parameter. The embedding is done around the top and bottom surfaces of the first and second ring. The dimension of the grid size is specified in table 3.1.

Case No.	dx (mm)	dy (mm)	dz (mm)	Embedding scale	Embedding Layers	Total Cells
1	0.000025	0.000025	0.000025	2	1	581 880
2	0.000012	0.000025	0.000012	2	1	1 725 358
3	0.000025	0.000025	0.000012	2	1	986 448
4	0.00001	0.00001	0.000025	0	0	1 288 508

Table 3.1 Grid specification for 2D cylinder-kit assembly

The configuration of the grid systems that are internally generated in CONVERGE by setting the parameters according to the Table 3.1, is shown in Figure 3.24 through Figure 3.31. The focus of these pictures are around the areas of large gradients.

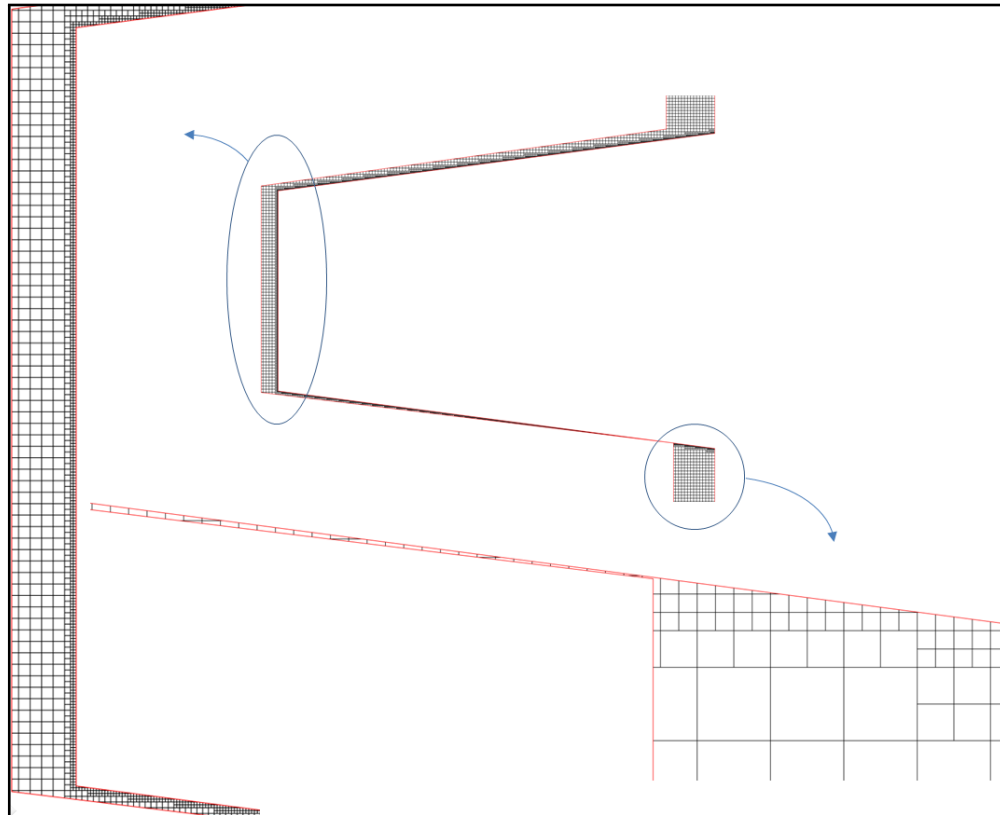


Figure 3.24 Grid around ring 1 - Case No. 1

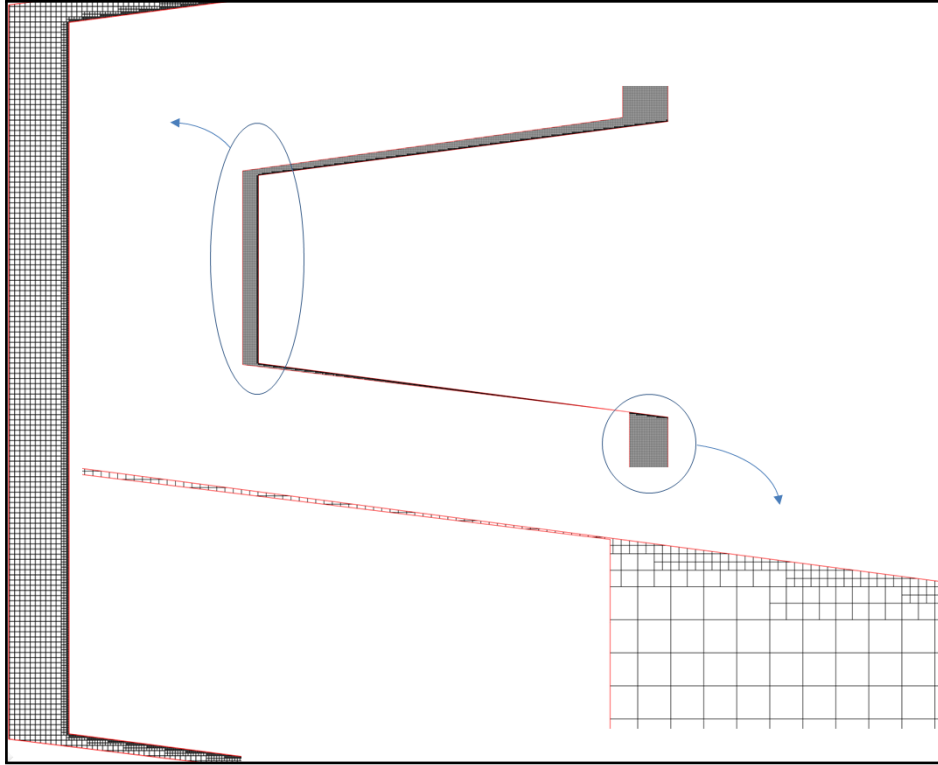


Figure 3.25 Grid around ring 1 - Case No. 2

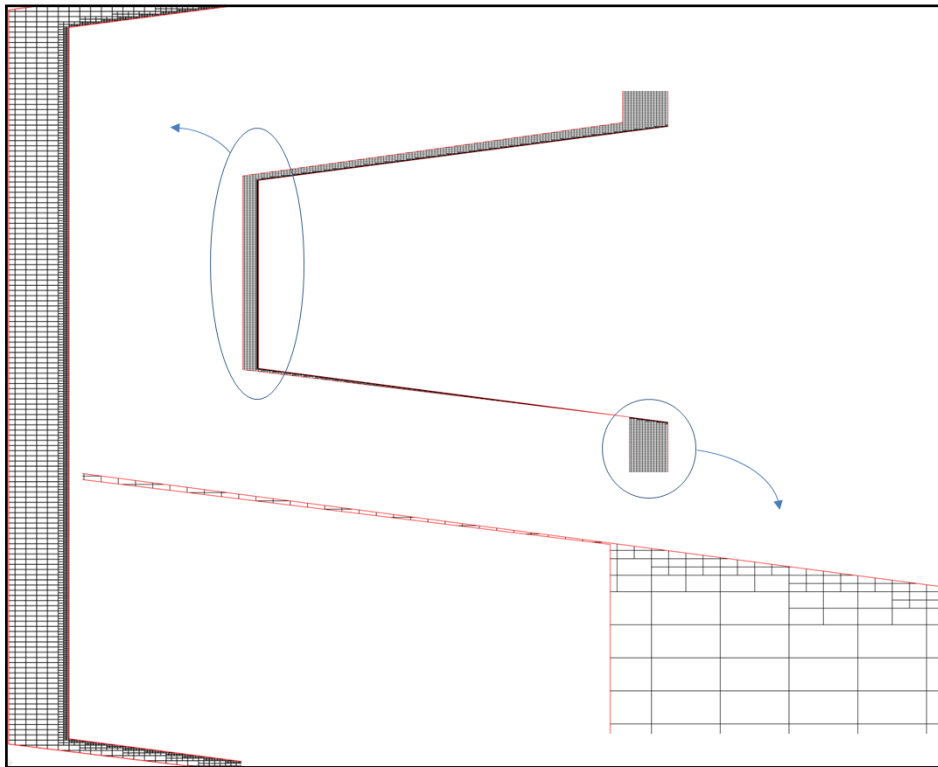


Figure 3.26 Grid around ring 1 - Case No. 3

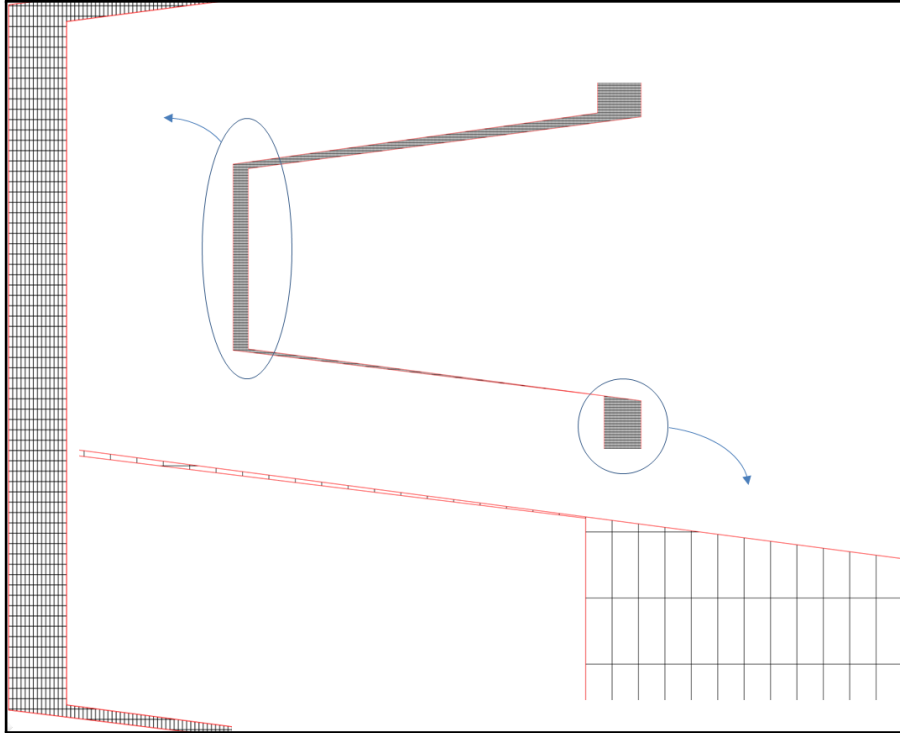


Figure 3.27 Grid around ring 1 - Case No. 4

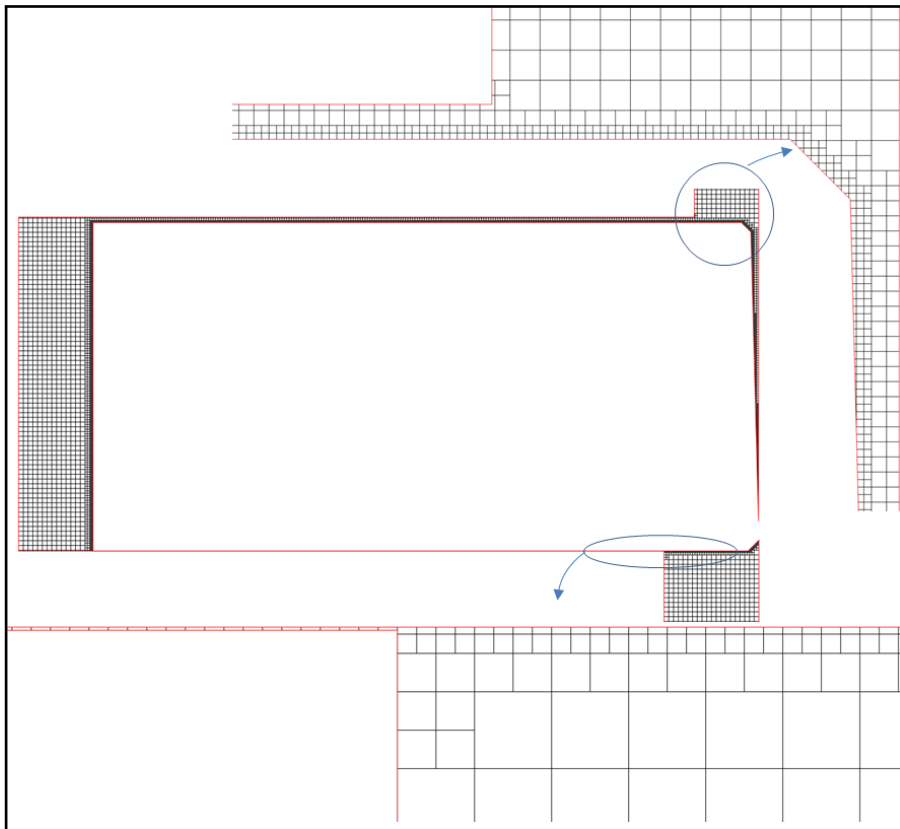


Figure 3.28 Grid around ring 2 - Case No. 1

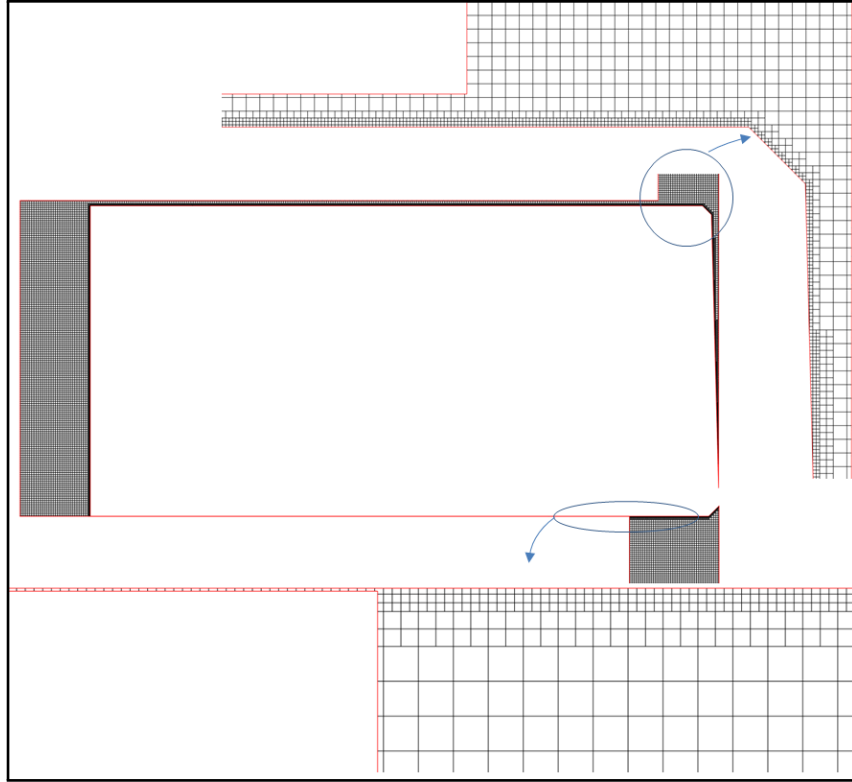


Figure 3.29 Grid around ring 2 - Case No. 2

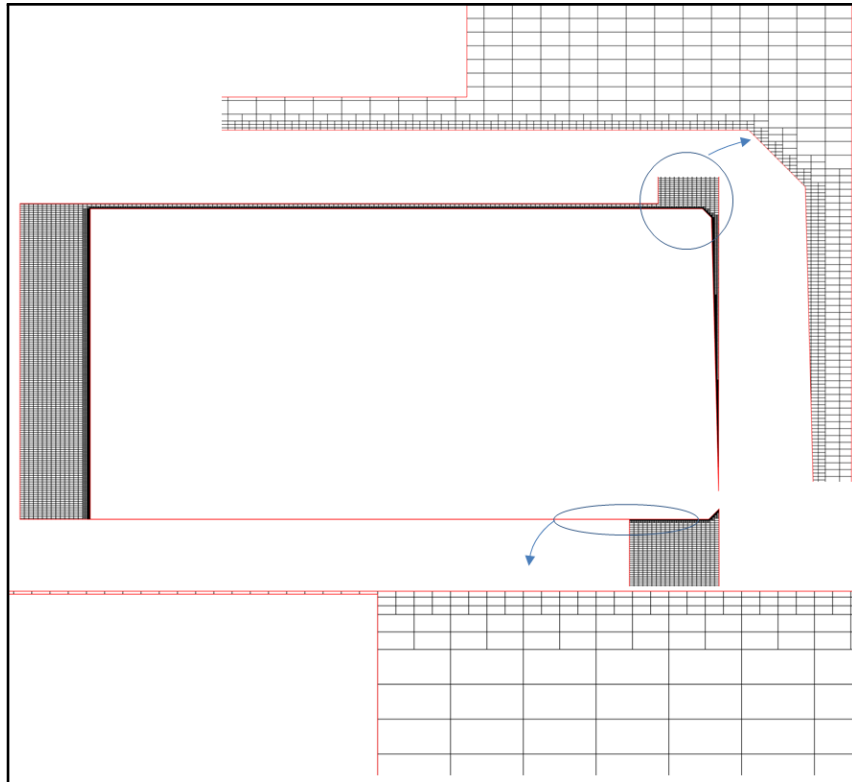


Figure 3.30 Grid around ring 2 - Case No. 3

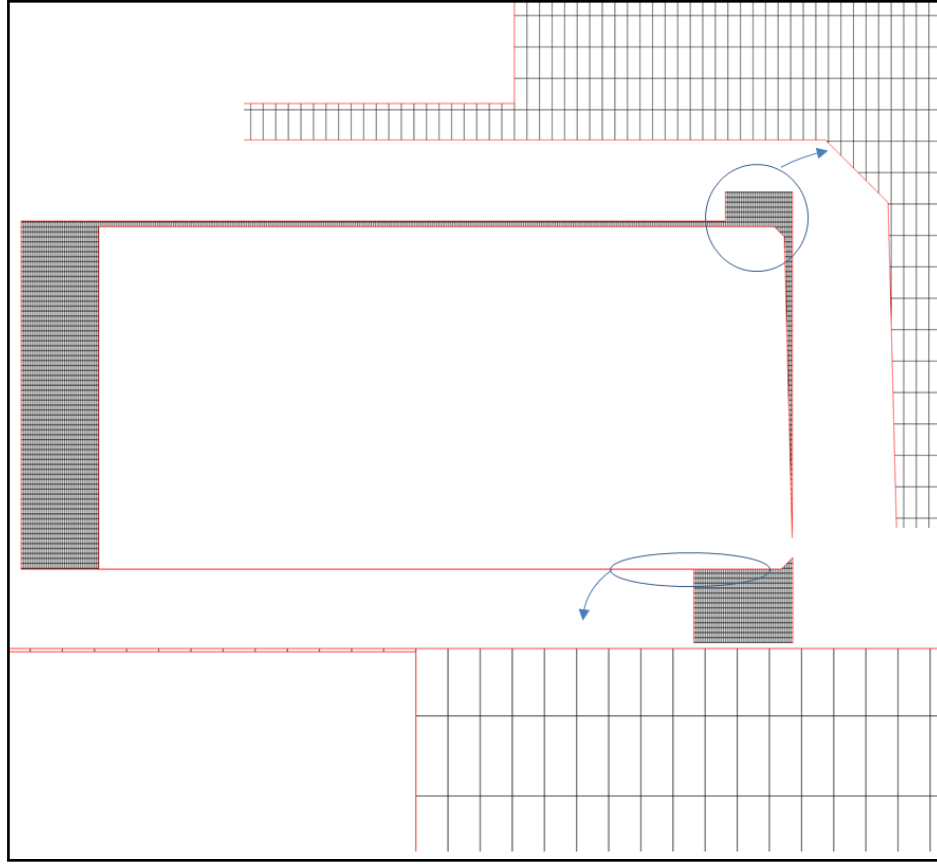


Figure 3.31 Grid around ring 2 - Case No. 4

The outlet Mass flow rate for different grid size but similar inlet pressure is plotted in Figure 3.32 for the 2D geometry. The inlet pressure is set to a known value based on in-cylinder pressure trace and the mass flow rate at the outlet is computed as the simulation progresses in time. The simulation for each grid system is considered completed when the mass flow rate converges to a constant value as shown in the figure 3.32. The inlet pressure of bin #1 was used to plot the mass flow rate for different grid sizes,

As shown in Figure 3.32 it is observed that refinement of the grid size shows significant changes in outlet mass flow rates for the 2D geometry, implying that a grid independent solution requires a very refined grid. Increasing the refinement provides for a converging solution which strongly asserts the need for extremely small grid size. Simulation of the 3D geometry was carried out with different grid levels according to Table 3.2.

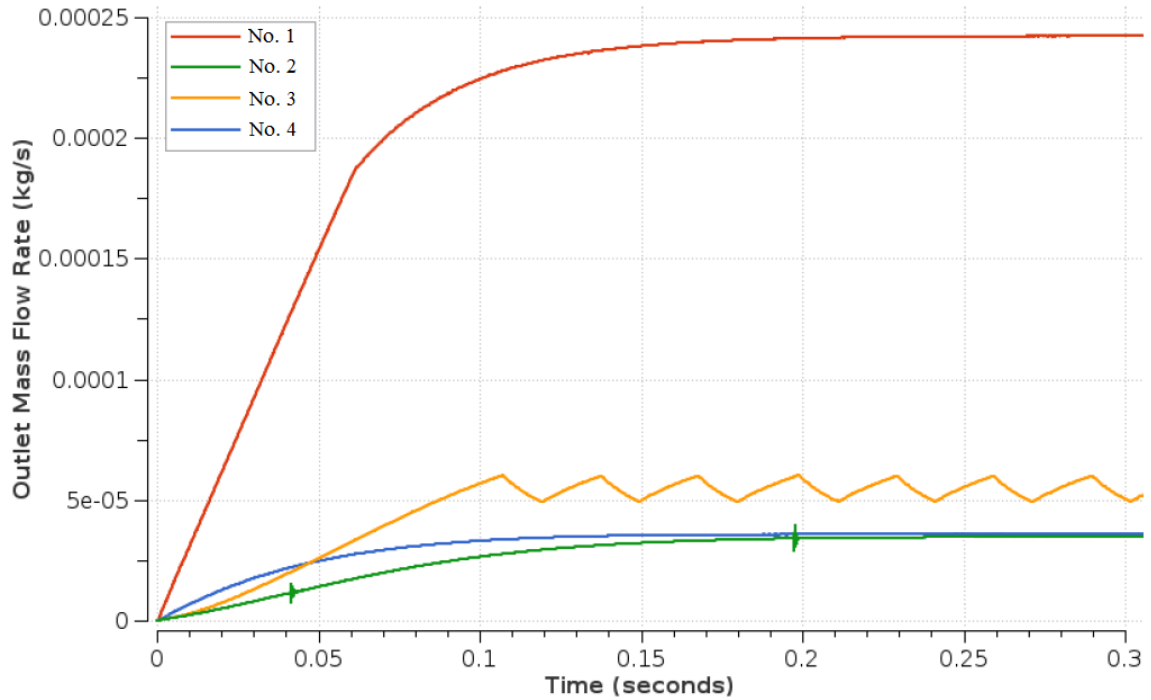


Figure 3.32 Calculated mass flow rate of 2D geometry and various levels of grid size

Case No.	dx(mm)	dy(mm)	dz(mm)	Embedding scale	Total Cells
1	0.0002	0.0002	0.0005	1	257 798
2	0.0002	0.0002	0.0001	1	1 021 623
3	0.0001	0.0001	0.0001	1	3 236 808
4	0.000075	0.000075	0.0001	0	5 393 644
5	0.000075	0.000075	0.0001	1	7 508 871
6	0.00005	0.00005	0.0001	0	11 335 292

Table 3.2 Grid specification for 3D cylinder-kit assembly

Additionally, the grid is refined in locations close to the first ring because of the high pressure gradient by setting the embedding parameter. The embedding is done around the top and bottom surfaces of the first and second ring similar to the 2D geometry. These locations are defined as narrow cylinders that contain the top and bottom surfaces of the rings as shown in Figure 3.33 by hatched area

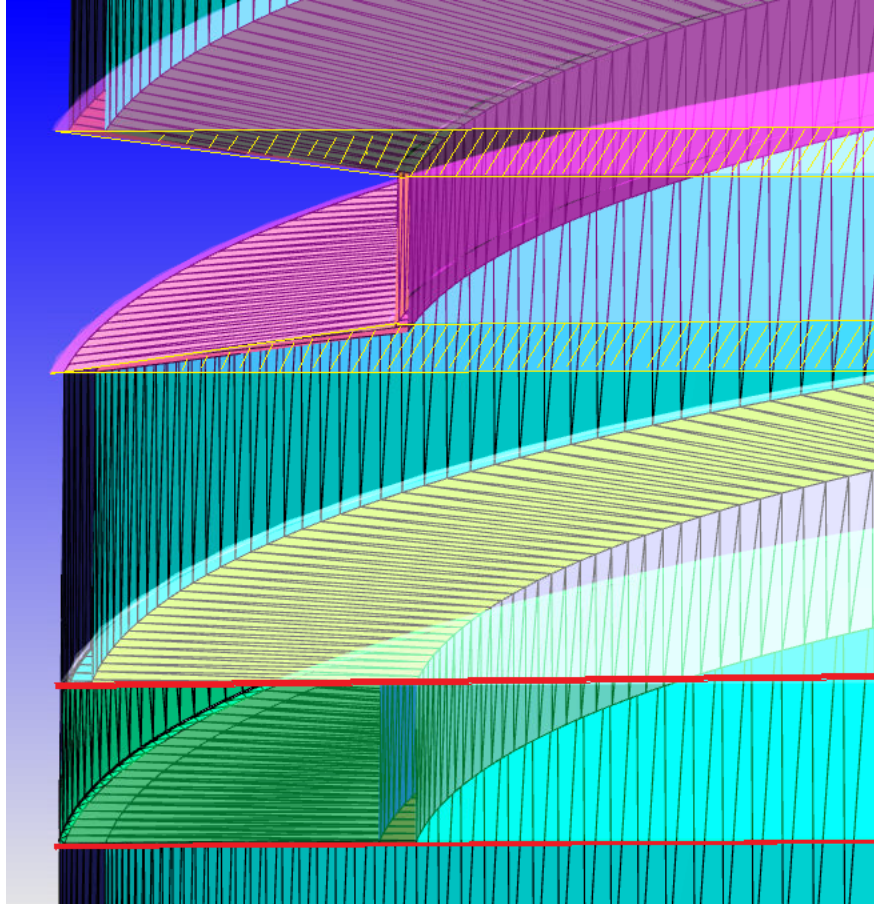


Figure 3.33 Fixed embedding location (hatched area) in 3D geometry

The density of the examined grid systems are shown in Figure 3.34 through Figure 3.37. The geometry is cut in axial direction for a better view of the generated grid.

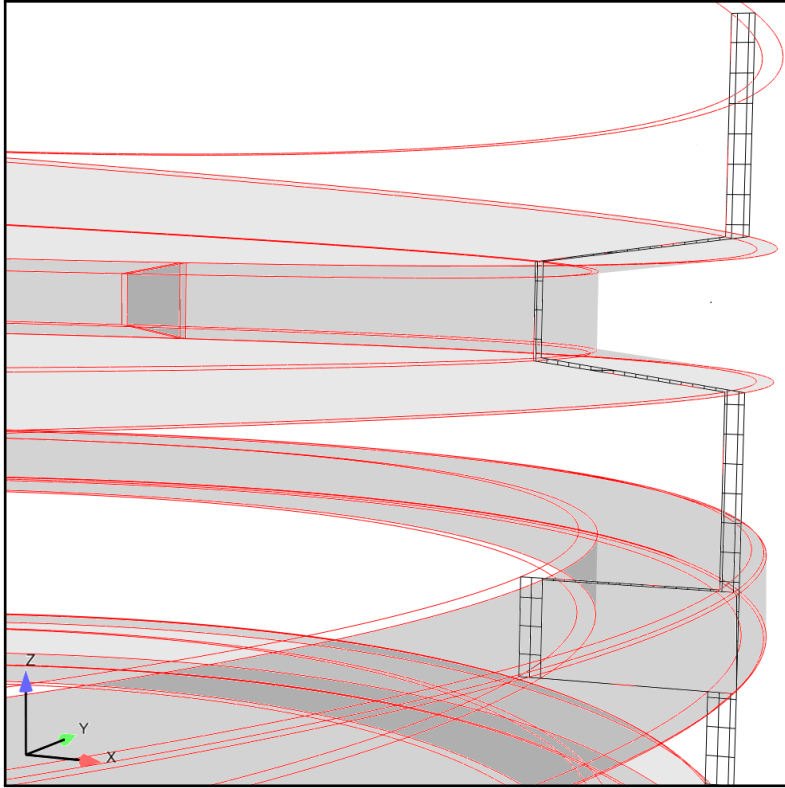


Figure 3.34 The 3D grid system - Case No.1

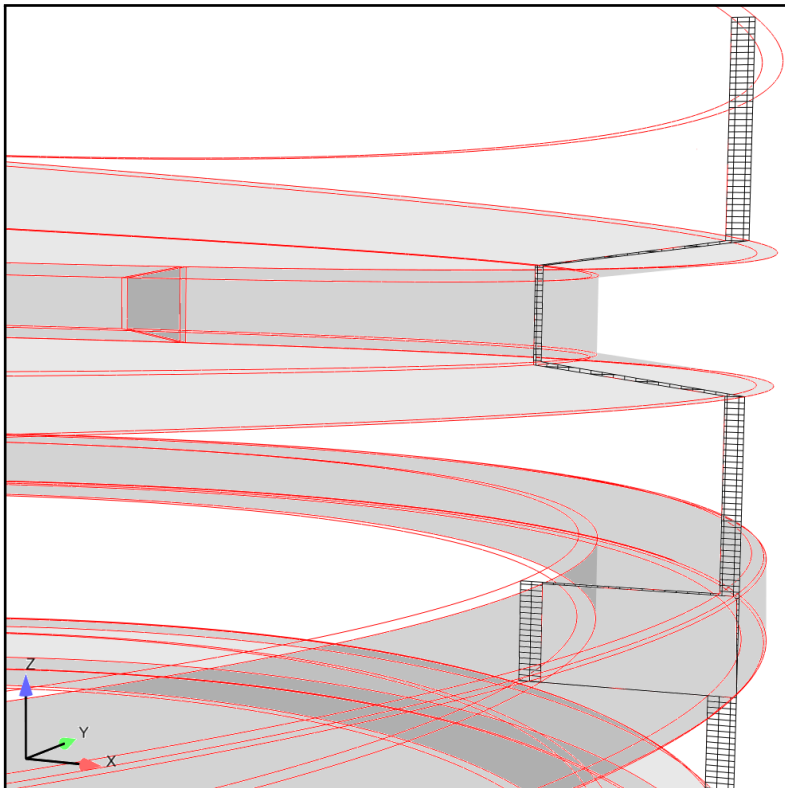


Figure 3.35 The 3D grid system - Case No.2

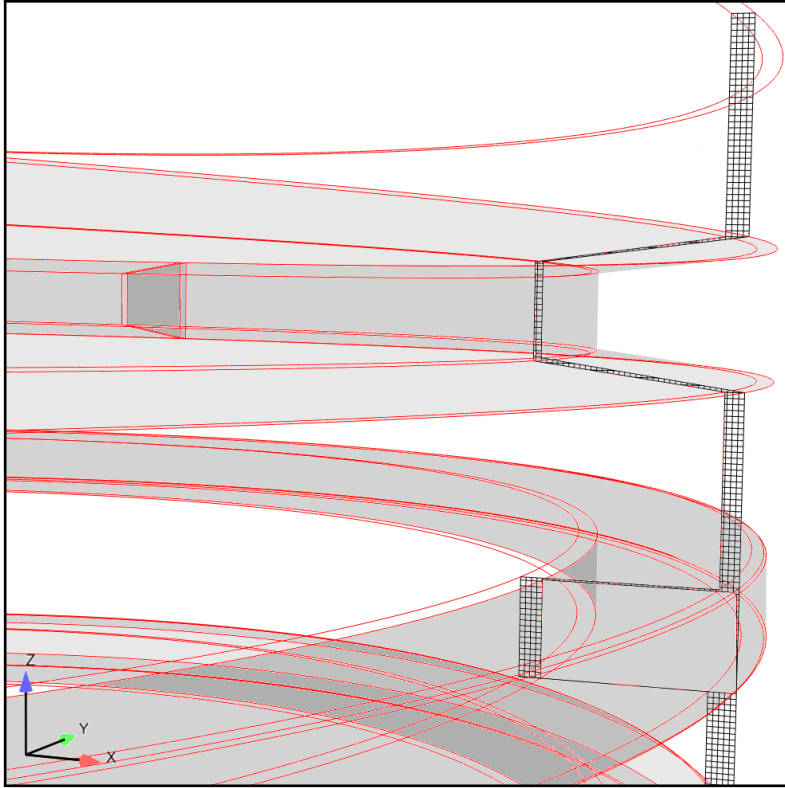


Figure 3.36 The 3D Grid system - Case No.3

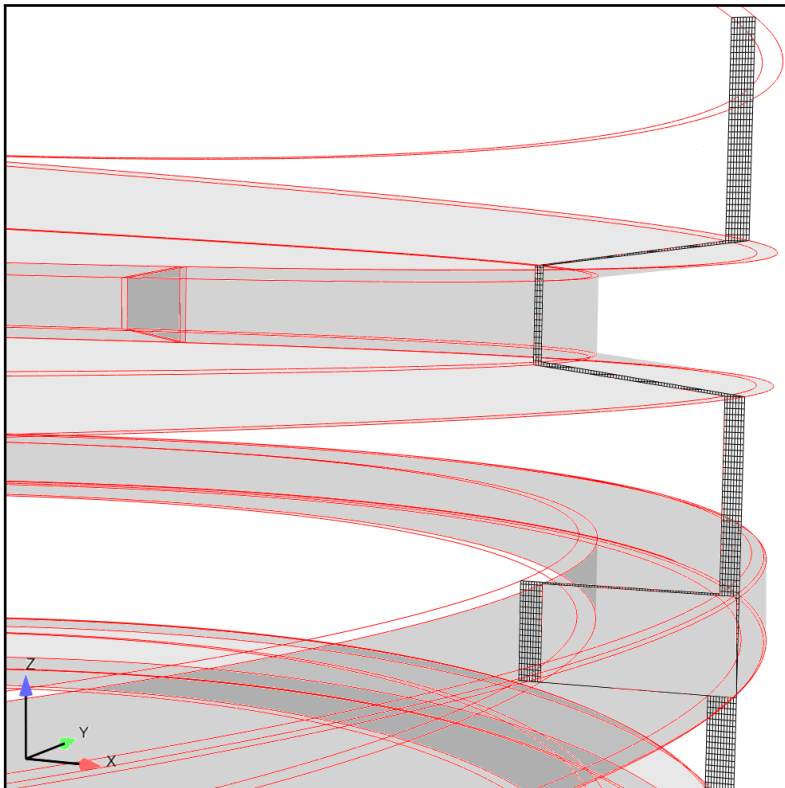


Figure 3.37 The 3D grid system - Case No.6

A quick observation of the grid systems reveals that the 6th grid system is more suited to resolve the flow in small areas. However, the high simulation time of that grid system has refrain us from pursuing high cell numbers in our simulation.

3.5 Simulation time of the 3D geometry

In order to investigate the simulation time of the different grid levels explained in Table 3.2, a benchmark example problem is introduced as follow.

For each grid level, the in-cylinder pressure of the first and last bin was applied at the inlet and the geometry was simulated for 4 hours. The development time of each hardware setup for different grid systems in a 4 hours wall clock simulation is shown in Table 3.3. Due to the limitation on the available memory, some of the below computation setups were unable to produce any meaningful results and therefore, were removed. The run time is extracted and compared for different cases. The highest run time indicates a faster simulation which is highlighted in the Table 3.3. It is observed that for each case, different setups must be tested to find the quickest simulation. For example, for the grid system of No. 5, 16 processors setup runs faster than 32 processors, while this conclusion does not hold true for the grid system of No. 3. Moreover, it is found to be impossible to predict the fastest computational setup for each grid systems before performing a benchmark example problem. In order to find the optimized hardware setup for the 3D simulations pursued in this study, a quick benchmark simulation were established and the simulation times were compared to find the quickest hardware setup.

All the simulations on this study were performed in the High Performance Computing Center (HPCC) of Michigan State University and the jobs were submitted to the system and computational resources were provided based on the availability. HPCC is comprised of different clusters. Each cluster runs the Community Enterprise Operating System (CentOS) 6.6, each with a different combination of memory and interconnects and use TORQUE for resource management, and Moab for job management. The number of nodes for the cluster used in this study is 128 which use two

Case No.	Run time 16 Procs. (sec)	Run time 32 Procs. (sec)	Run time 64 Procs. (sec)
1	6.30E-03	1.95E-03	1.43E-03
2	7.80E-04	1.60E-03	7.60E-04
3	8.41E-05	3.36E-04	3.39E-04
4	4.25E-05	6.12E-05	6.72E-05
5	7.12E-05	2.38E-05	-
6	-	7.20E-05	-

Table 3.3 Simulation time for different grid levels of bin #1 inlet pressure

2.5 GHz 10-core Intel Xeon E5 for its processor and 51 TFLOP for the bandwidth.

3.6 Parallel computing

This section briefly describes the differences in classification of parallel computer architectures and discusses the message passing and data parallel programming paradigms. Then the issues in the parallel programs are discussed and finally the obstacles in decreasing the simulation time of CONVERGE are reviewed.

Parallel computing is the simultaneous operation of multiple computational tasks on a computer system. In the simplest sense, parallel computing is the simultaneous use of multiple compute resources to solve a computational problem:

- A problem is broken into discrete parts that can be solved concurrently.
- Each part is further broken down to a series of instructions.
- Instructions from each part execute simultaneously on different processors.
- An overall control/coordination mechanism is employed.

The computational problem should be able to be broken apart into discrete pieces of work that can be solved simultaneously [79]. For example:

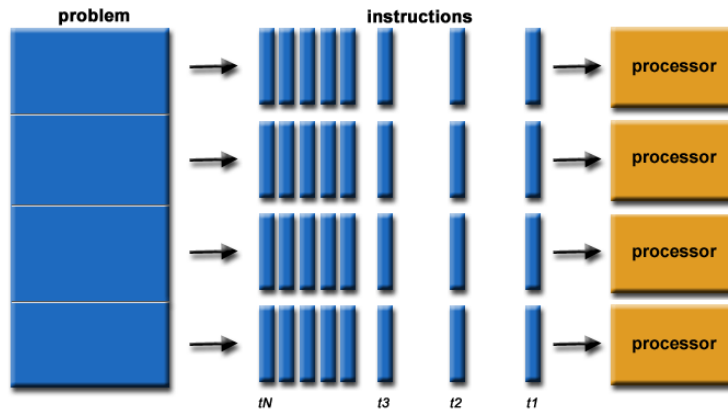


Figure 3.38 Parallel computing

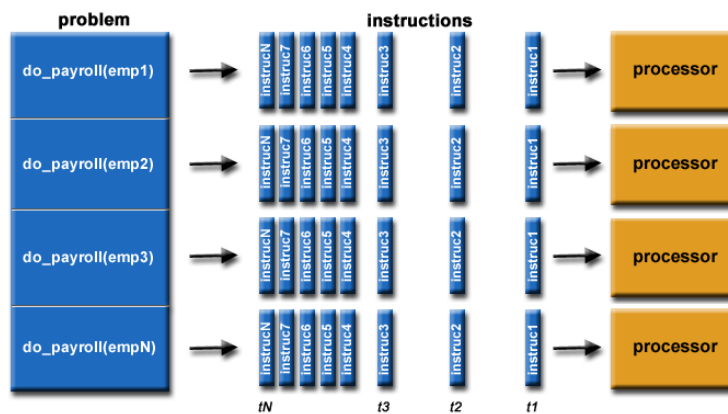


Figure 3.39 Example of parallel Computing

3.6.1 Classification of parallel computer architecture

There are **four** distinct levels of parallelism [80]. The highest level is *job*, where the computer system operates simultaneously on unrelated tasks (e.g., a CFD simulation for an F18 airplane). The second level is *program*, where the computer system operates simultaneously on different parts of the same program (e.g., the parallelization of a do loop across multiple processors). The third level is *instruction*, where the different instructions are performed in parallel (i.e., fetching one instruction from memory while performing an arithmetic operation). The fourth level is *arithmetic and bit*, where parallelism is achieved within an individual arithmetic or bit instruction.

Flynn [81] originated a classification of parallel architectures which has become widely accepted (See Table 3.4).

<i>Acronym</i>	<i>Definition</i>
SISD	Single Instruction Stream – Single Data Stream
SIMD	Single Instruction Stream – Multiple Data Stream
MISD	Multiple Instruction Stream – Single Data Stream
MIMD	Multiple Instruction Stream – Multiple Data Stream

Table 3.4 Flynn’s Taxonomy

Bell [82] subdivides the MIMD category into two subcategories as indicated in Figure 3.40.

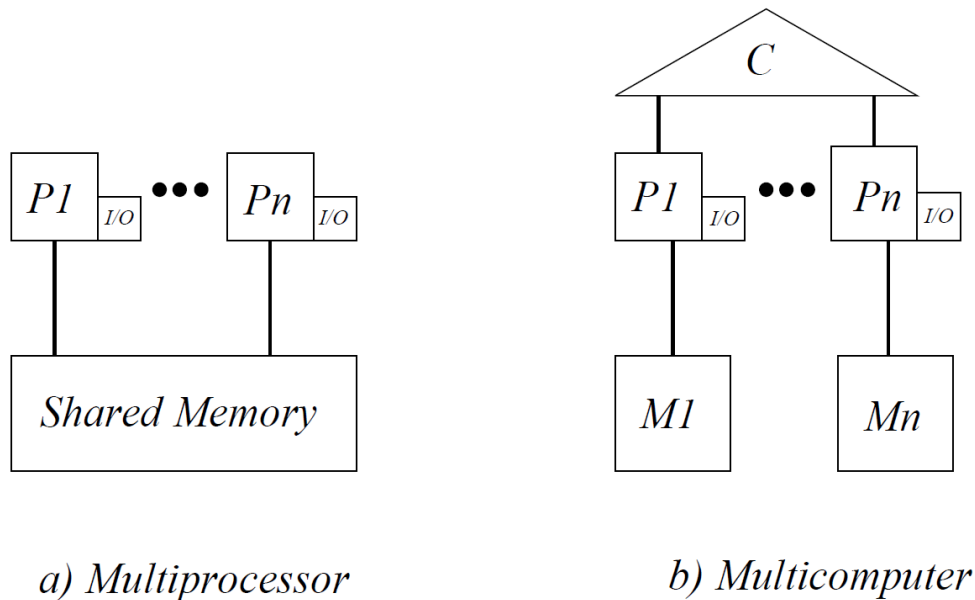


Figure 3.40 Multiprocessor and Multicomputer

Multi-processors are parallel computers with a single address memory (shared memory), i.e., the central memory (RAM) is organized into a single logical address domain which is accessible to all of the processors. Processors $P_1; \dots; P_n$ can access the same data in memory (i.e., the same address location), albeit not simultaneously.

Multicomputers are parallel computers with multiple distributed memory address spaces. Processor $P_1; \dots; P_n$ have dedicated, independent memories $M_1; \dots; M_n$ which are not directly accessible by each other. If processor P_1 needs to access data in the memory assigned to processor P_n

, it sends a message to P_n requesting the data, and P_n complies. The transfer of data from the memory of one processor to the memory of another is denoted message passing, and is a principal characteristic of multi-computers.

All communications between processors occur through a communications network C in Figure 3.40.

For a multi-processor, the shared memory eliminates the computational cost and program complexity of message passing. However, a multi-processor with a single shared memory is not scalable, i.e., the architecture cannot simply be scaled to an arbitrary number of processors and arbitrary memory size. This arises from the limitation on data transfer rate (bandwidth) between memory and processors.

For a multi-computer, the distributed memory eliminates the scalability problem (see section 3.6.3) associated with a single memory of limited bandwidth. However, multi-computers incur the computational cost and program complexity of message passing.

3.6.2 Issues in parallel computing

The partitioning of data and computational tasks among multiple processors is denoted *domain decomposition*. The principal objective of domain decomposition is to maintain uniform computational activity on all processors. This is known as *load balancing*. The idea is to decompose the domain of a partial differential equation and after discretization one obtains a linear system which is also decomposed. Depending on the decomposition method, the computations of the domains may not depend on each other. In other words: to solve a linear system of equations, an appropriate domain decomposition method has to be chosen [83].

Several factors can complicate load balancing. For example the nature of the governing equations can change during the computation as seen in combustion where the chemical reaction source terms are not always computed; or when the number of governing equations changes in a given subdomain.

The key issue is the performance of a CFD code on a parallel computer. In solving a given problem the true measure of performance is simply the wall clock time to completion. In other words, given the opportunity to choose among different computational resources, the individual typically selects the resource which yields the answer in the shortest elapsed time, subject to existing constraints (e.g., budget, system load, etc).

3.6.3 Scalability

In the context of high performance computing *scalability* is the ability of the system to accommodate larger loads just by adding resources either making hardware stronger (scale up) or adding additional nodes (scale out).

The impact of scaling a given parallel computer architecture to increasingly larger number of processors is a key concern. Consider the solution of a given computational fluid dynamics problem, e.g., a Reynolds-Averaged Navier-Stokes simulation of an aircraft. How does the efficiency of the computation depend on the number of processors? Assume that an analysis of the program and algorithm structure indicated that a portion of the code could be reprogrammed for parallel execution. Neglecting the cost of scheduling processors, communications between processors (if any) and synchronization time (i.e., the time required to allow all processors to reach a common point following execution of the parallel section of code), and the efficiency of a parallel computation with n processors is increased. In some cases, the relative cost of communication increases rapidly and efficiency drops when increasing the number of processors [84] .

3.6.4 Parallel processing in CONVERGE

For parallelization, the CONVERGE employs an automatic domain decomposition algorithm. The parallel blocks begin at the same size as the base grid cells. CONVERGE then coarsens the parallel blocks by combining eight child cells into a single parent cell. The coarsening continues up to the specified level. At this point, each cell is a parallel block, each of which can be assigned to a

processor. Figure 11.1 below shows an example of the parallel automatic domain decomposition for a four-processor case modeling flow in a duct [74].

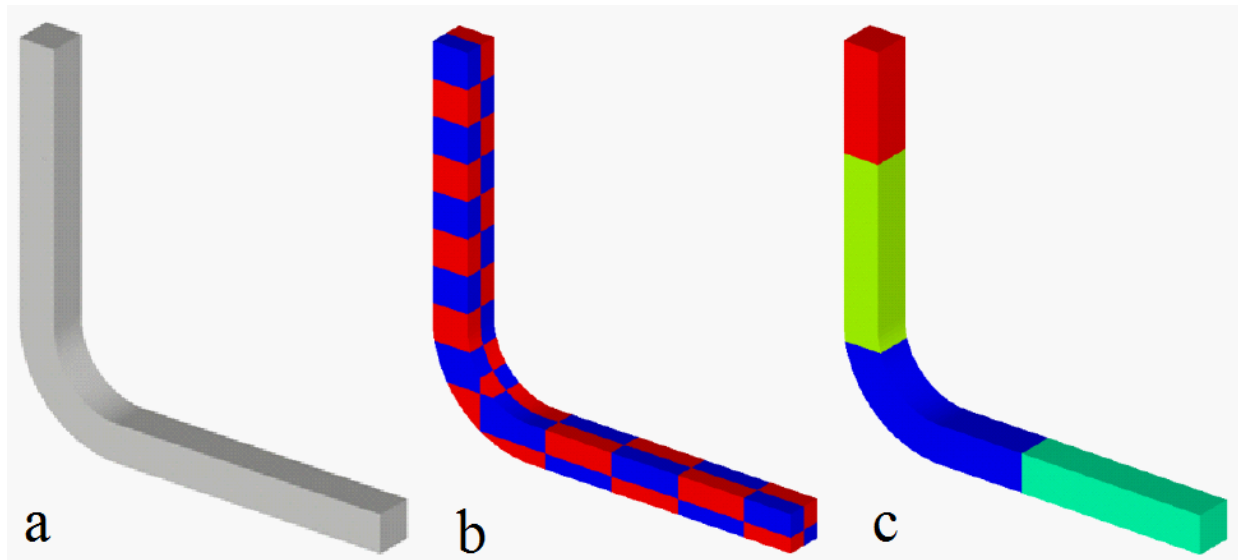


Figure 3.41 An example of automatic parallel domain decomposition of a duct: (a) duct surface geometry; (b) parallel blocks from user-specified *parallel_scale*, where each blue or red section represent a single parallel block; (c) assigned domain for four processors, where each color represents the computational region for a single processor (which is made up of several parallel blocks).

In CONVERGE, each processor contains the entire surface and coarsens in the described manner to the user-specified value of *parallel_scale*. For example, if the initial grid consists of 32,768 cells and *parallel_scale* = -3, the initial grid will be coarsened three times to yield a parallel grid of 64 parallel blocks ($8^{-3} = 1/512$) [74].

When the domain is subdivided into parallel load blocks, CONVERGE performs a load balance. Once the grid is created, the load balancing procedure assigns the block to the processors to achieve two main goals:

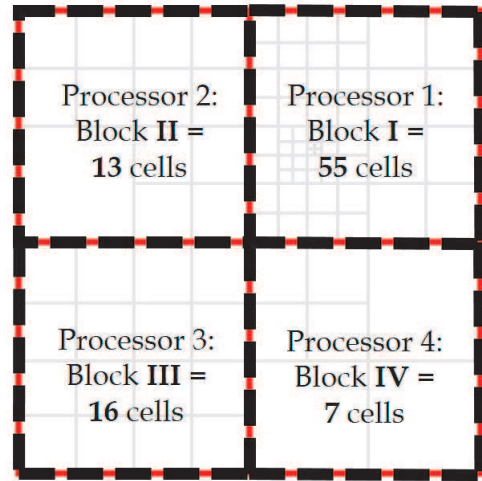
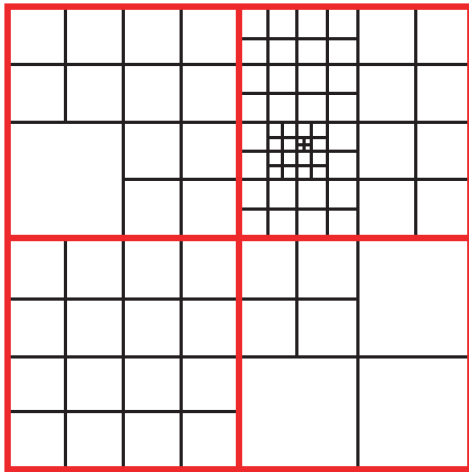
1. Balance the number of computations so that they are the same on all machines.
2. Minimize the amount of information that will need to be passed between machines by minimizing the block interface area, (i.e., group neighboring parallel blocks together on the same processor as much as possible).

The load balance algorithm that is currently used in this version of the CONVERGE, assumes that each processor used in the simulation has the same speed. As a result, the overall job speed of a perfectly balanced case will be limited by the speed of the slowest machine.

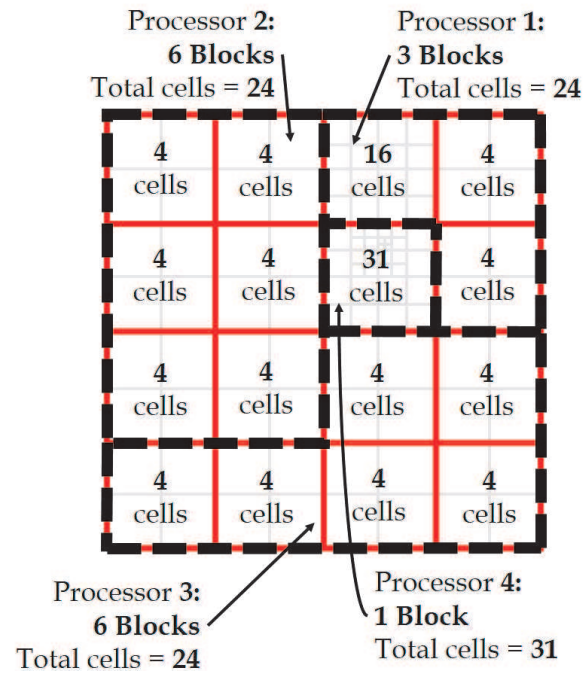
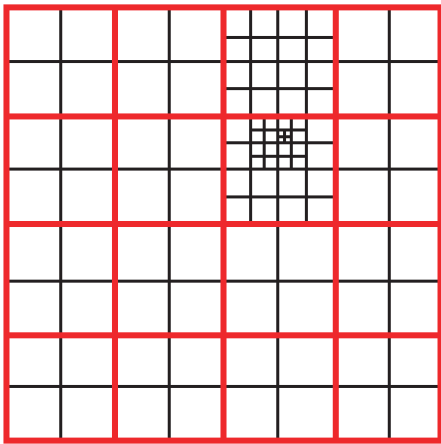
The load balancing algorithm in CONVERGE places highest priority on getting the cell count down on the processors with the highest cell count. Due to this type of prioritization algorithm, once there is a single processor with a cell count much higher than the average, the balancing of the remaining blocks is random. In this scenario, one processor with a cell count much higher than the average is much worse than having one processor with a cell count much lower than the average.

Figure 3.42 graphically describes how reducing the size of the base grid can help to reduce the load balancing bottleneck in parallel processing.

In this example, even though the total cell count for the configuration on the left (91 cells) is lower than the total cell count for the configuration on the right (103 cells), the simulation with the smaller base grid (Figure 3.42b) will run faster. This is because the most heavily-loaded processor in Figure 3.42b (31 cells) has fewer cells than the most heavily-loaded processor in Figure 3.42a (55 cells).



(a)



(b)

Figure 3.42 Load balancing for two different base grid sizes. Red lines demarcate parallel blocks, which can be assigned to different processors. Processor distributions are indicated by heavy dashed lines. Because the base grid size of (b) is half that of (a), parallel blocks can be more evenly distributed. In (a), note the bottleneck in Processor I, which has more than three times more cells than any other processor. Due to the large amount of cells in this processor, (a) has a longer runtime than (b).

CHAPTER 4

RESULTS AND DISCUSSION

4.1 Introduction

In this chapter, different test runs are established and the simulation process is explained to understand how CONVERGE works and verify the validity of the CFD solver. Then the geometry of the proposed problem is created using Link program by importing the CASE input file as discussed in chapter 3. Finally, the simulation results are discussed and conclusions are presented.

4.1.1 Test run 1 (Narrow channel)

The validity of the CONVERGE solution is first tested by simulating the air flow in a narrow slab with $45 \times 30 \times 0.57$ mm dimensions (Figure 4.1) and obtained results are compared with analytical solutions. The pressure at the outlet is set to atmospheric pressure and the inlet to 102 kPa to maintain a 2 kPa pressure difference at both ends of the channel.

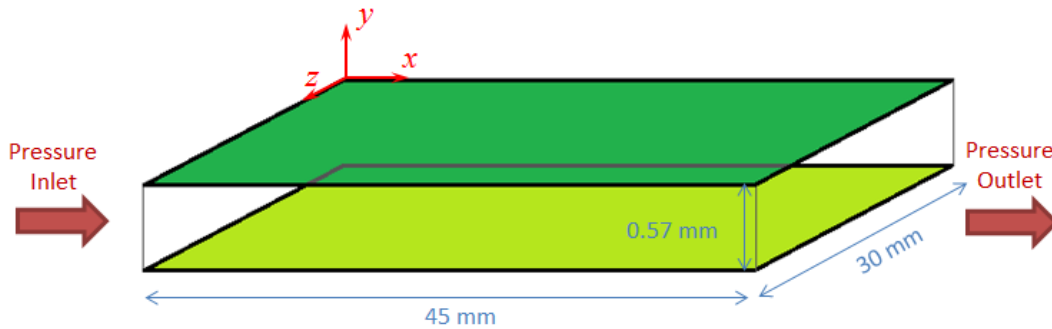


Figure 4.1 Geometry of the test run 1 - Narrow channel

Different grid systems were examined according to Table 4.1 and the configuration of the generated grid systems are shown in Figure 4.2.

The Air composition is selected as 77% Nitrogen and 23% Oxygen and the Redlich-Kwong cubic equation of state (equation 3.9) is used to couple the density and temperature of air. Flow is assumed to be Laminar and unsteady. The outlet mass flow rate is calculated at each time and the

Case No.	dx(mm)	dy(mm)	dz(mm)	Embedding scale	Embedding Layers	Total Cells
1	0.0005	0.0001	0.005	2	1	46 564
2	0.0005	0.0001	0.005	2	2	82 886
3	0.0005	0.0001	0.001	2	1	212 116

Table 4.1 Grid systems used for test run 1 - Narrow channel

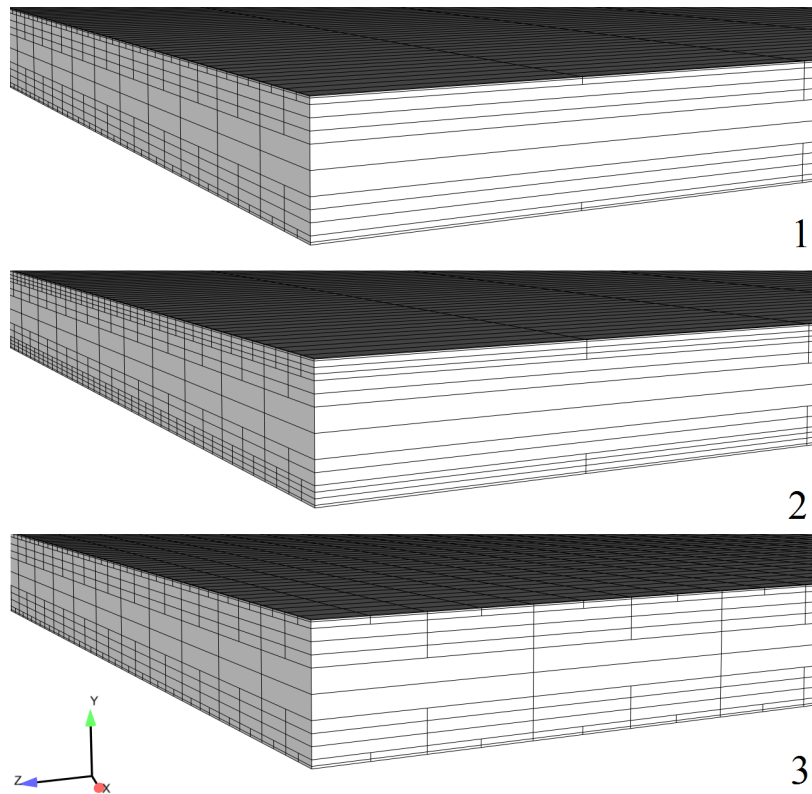


Figure 4.2 Snapshot of the grid systems used for test run 1 - Narrow channel

flow is fully developed. These conditions are chosen to be similar to the cylinder kit problem so that the mechanism of the available tools in CONVERGE are understood better.

The velocity vector at the channel outlet as well as the pressure distribution across the channel is shown in Figure 4.3. As predicted by analytical results, the velocity profile follows the hyperbolic function (see Figure 4.4). This results shows that CONVERGE can easily model the unsteady flow of air in a narrow channel.

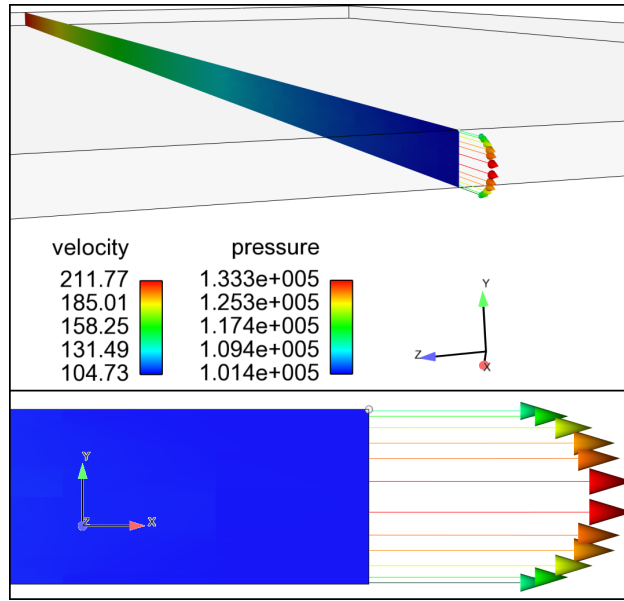


Figure 4.3 Velocity profile at the outlet for test run 1 - Narrow channel

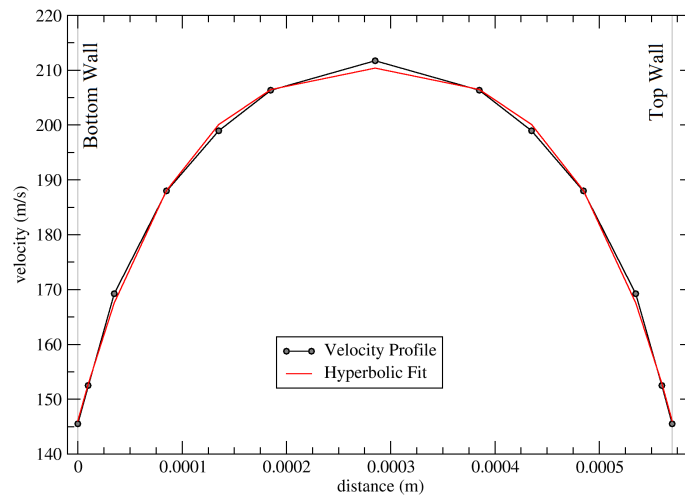


Figure 4.4 Outlet velocity profile curve fit for test run 1 - Narrow channel

4.1.2 Test run 2 (Hollow Cylinder)

In another attempt, air is allowed to pass through a hollow cylinder with the same boundary conditions described in the narrow channel test run. No slip wall boundary condition was applied at the inner and outer surface of the cylinder and Inflow and Outflow boundary conditions were imposed on the inlet and outlet of the geometry. the temperature is set to 300 °K all around and the pressure difference of 2 kPa is maintained between both ends of the cylinder. Then the transient

solver of CONVERGE were utilized and the flow were simulated until it was fully developed. The schematic view of the geometry is shown in Figure 4.5.

Two different grid systems were examined for this geometry with the specifications explained in Table 4.2. The density of the generated grid systems were shown in axial and circumferential direction by two cut planes as illustrated in Figure 4.6.

Case No.	dx(mm)	dy(mm)	dz(mm)	Embedding scale	Embedding Layers	Total Cells
1	0.0003	0.001	0.0003	1	2	401 620
2	0.0001	0.002	0.0001	1	2	777 552

Table 4.2 Grid systems used for test run 2 - Hollow cylinder

The velocity flow field near the inlet is shown by cutting the flow field in transverse direction and drawing the velocity vectors. the magnitude of the velocity and the location of cut surface is shown in Figure 4.7.

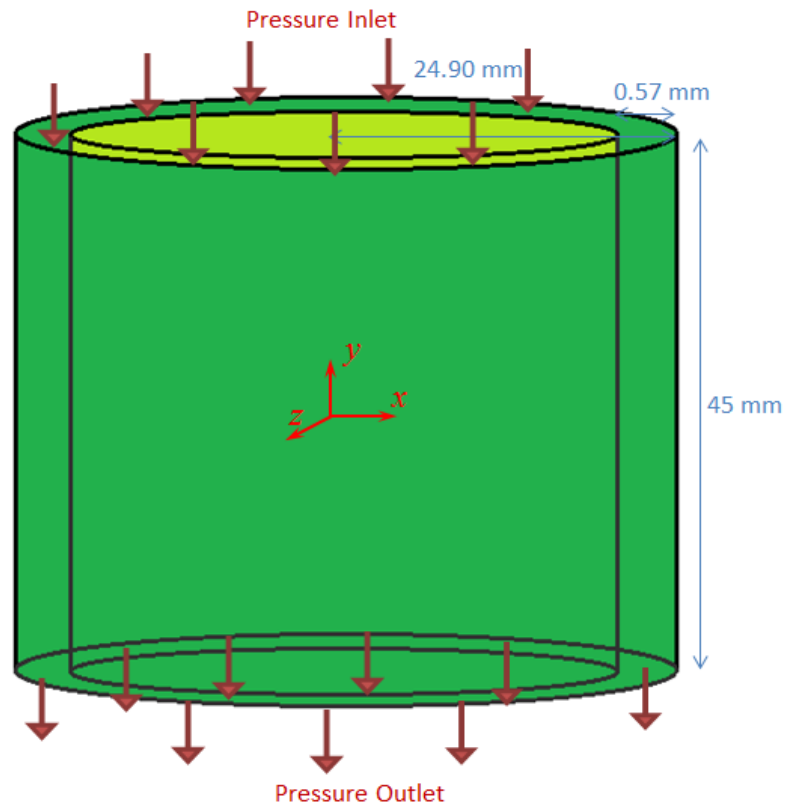


Figure 4.5 Geometry of the test run 2 - Hollow Cylinder

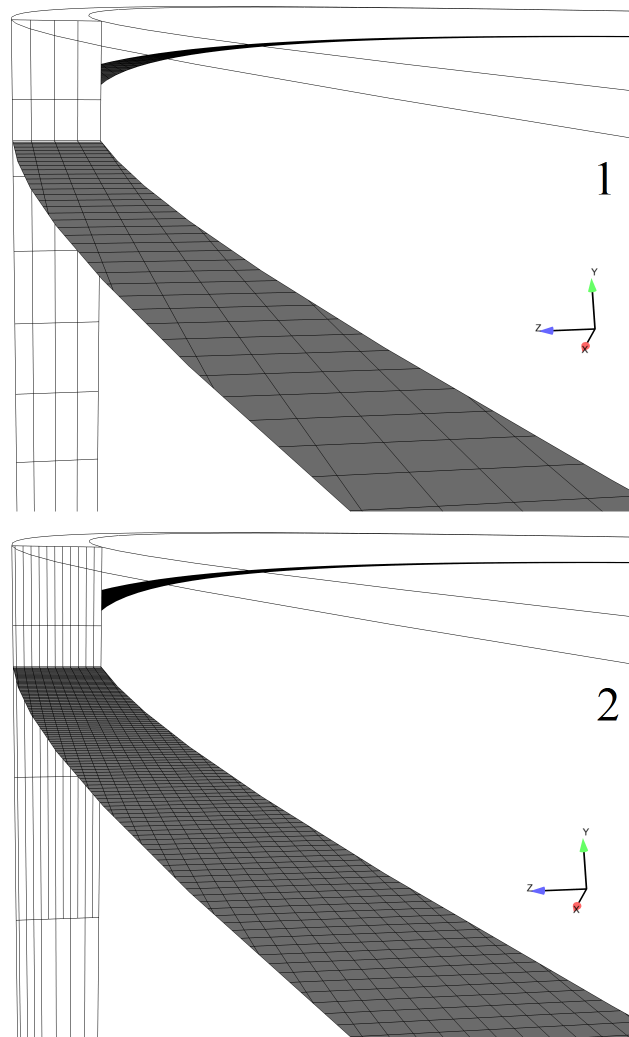


Figure 4.6 Snapshot of the grid systems used for test run 2 - Hollow cylinder

The main purpose of this simulation was to examine the the structured grid that is internally created in CONVERGE in a circular shaped geometry. It is found that the available tools in CONVERGE can provide enough flexibility for determining the desired grid system. It is also found that the calculated results are grid independent.

4.1.3 Test run 3 (Channel with Obstacle)

A typical CFD simulation should restart several times due to hardware limitations. This requires saving the intermediate results and restarting the simulation from the stored ones. CONVERGE can restart a simulation from a restart file.

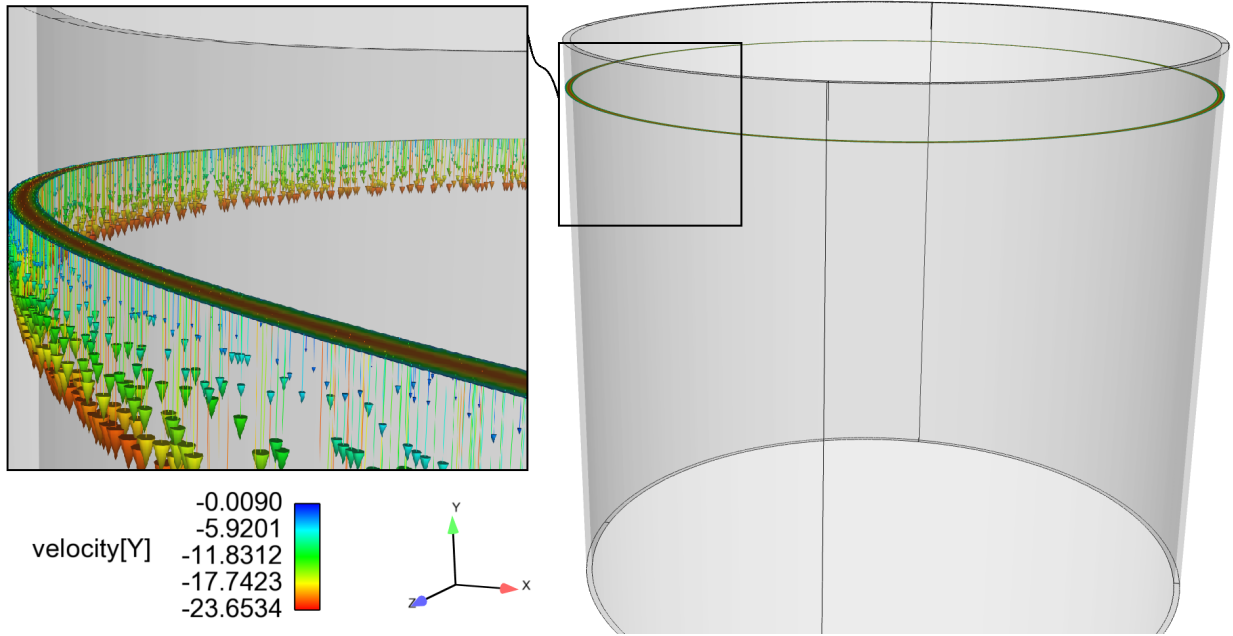


Figure 4.7 Velocity vector of the cut surface close to the inlet for test run 2 - Hollow cylinder

CONVERGE allows initialization of any number of flow field variables via mapping. The mapping option is useful if a new simulation is beginning from the output of another CFD simulation. This tool can be specially used in cylinder kit assembly simulation when the ring is twisted. In this case, the result of the normal ring (untwisted) can be mapped to begin the simulation of the twisted ring geometry.

In order to exploit the different available tools in CONVERGE, a 3D channel with an obstacle in the middle is considered to undergo a Poiseuille flow (Figure 4.8). The size of the obstacle grows to allow for testing the “mapping” concept of CONVERGE. The dimension of the geometry is shown in Figure 4.9.

The channel is first simulated by setting the inlet and outlet pressure to 150 *kPa* and 101 *kPa* respectively. In the first simulation, the obstacle height is set to 1.0 *mm* while in the second simulation the outlet pressure and channel height were increased to 250 *kPa* and 1.20 *mm* respectively.

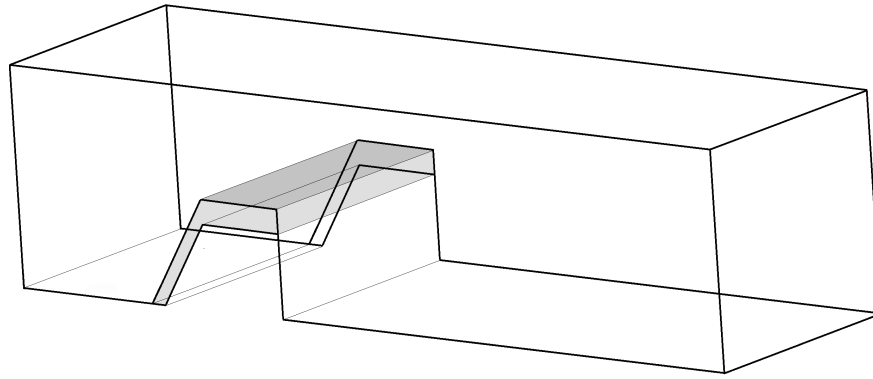


Figure 4.8 3D channel with different obstacle heights

Similar to the previous test runs, air with 77% Nitrogen and 23% Oxygen composition were selected as the working fluid. No slip wall boundary conditions as well as Inflow and Outflow boundary conditions were applied at the surrounding surfaces, inlet and outlet of the channel respectively. Unsteady solver were employed and the flow were assumed to be fully developed when exit mass flow rate does not change with time. In order to understand the benefit of the mapping tool, the second simulation (Obstacle height = 1.20 mm) were performed in two ways. In the first run, the flow field is obtained by mapping the result of the first simulation (Obstacle height = 1.00 mm) while in the second run, the flow was obtained by initializing the flow with uniform values.

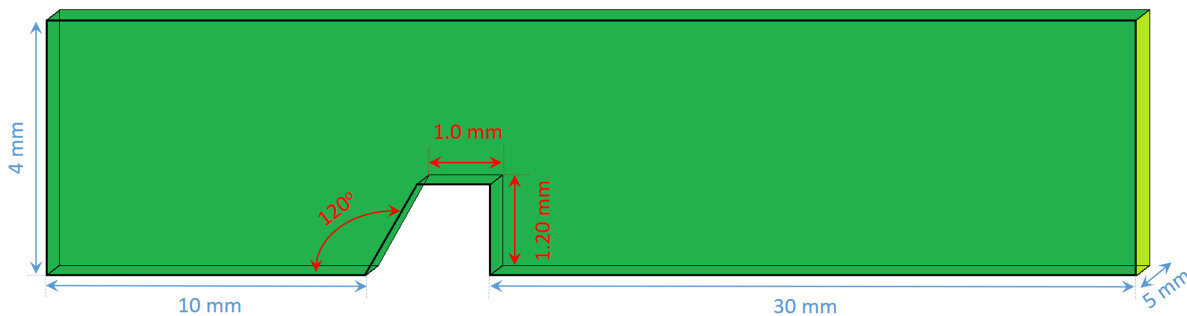


Figure 4.9 Dimensions of the 3D channel with obstacle

It has been observed that the velocity field is identical for both simulation runs at different cross sections of the geometry as shown in Figure 4.10. In this figure, the velocity profile for both simulations is compared for the cross section A-A and found to be completely equal.

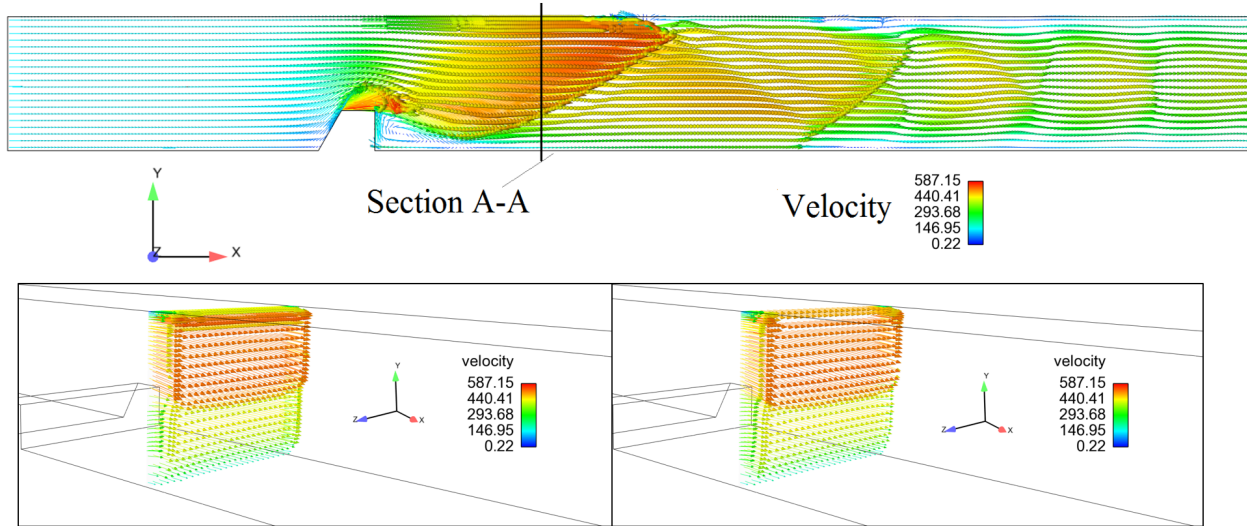


Figure 4.10 Velocity field of the 3D channel for different simulation. On the left, uniform initialization simulation result is shown. On the right, the mapping simulation result is depicted

It is also observed that the vortex eye location occurs at the same location in both simulations which is shown in Figure 4.11.

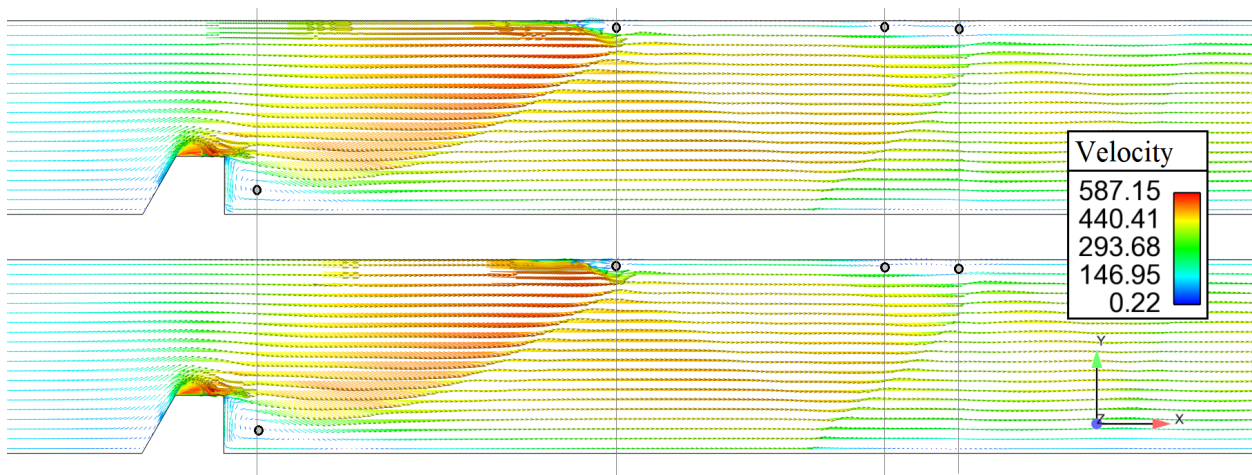


Figure 4.11 Velocity field and vortex eye location of 3D channel simulation

comparing the simulation time of the first and second run reveals that the time saved by mapping the results is significant. Therefore “mapping” can be used extensively to decrease the simulation time of a problem if the geometry change is not substantial.

4.2 Cylinder kit assembly Results

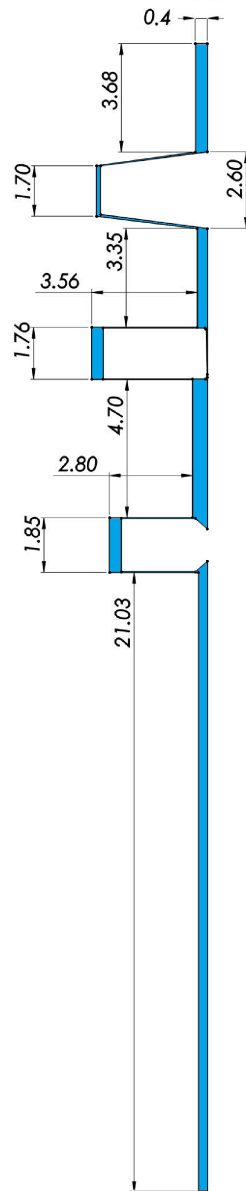


Figure 4.12 Cross section of the studied geometry

For selecting an adequate modeling option, it is essential to analyze the possible flow paths for the fluid from the combustion chamber to the crankcase as commonly known from the literature [24, 85]:

- Through the ring gap.

- Via the ring grooves in axial direction.
- Through the gaps between the ring and liner.
- Circumferentially along the ring lands.

The cross section of the studied ring pack is shown here again in 4.12. The pressure trace is considered known which is drawn in 4.13. Using the binning concept of section 3.4.1 the pressure trace is divided into 10 bins with varying thickness as shown in Table 4.3.

A quick observation of Table 4.3 reveals that 77% of the total crank angles fall into the first bin. Therefore, the result of the whole cycle is greatly affected by the accuracy of the solution of the first bin's result. One can divide the first bin into smaller divisions and solve the flow domain for each divisions separately. This will however, increase the resolution of the answer for the first bin at the cost of increasing the simulation time that has to be considered.

Bin	Pressure (bar)	Total no. of C.A.
1	1.6926	580
2	6.9165	41
3	11.299	23
4	16.6408	22
5	22.7334	19
6	30.7804	11
7	41.4608	3
8	48.6353	4
9	54.9357	6
10	62.1078	11

Table 4.3 Pressure bins after binning process

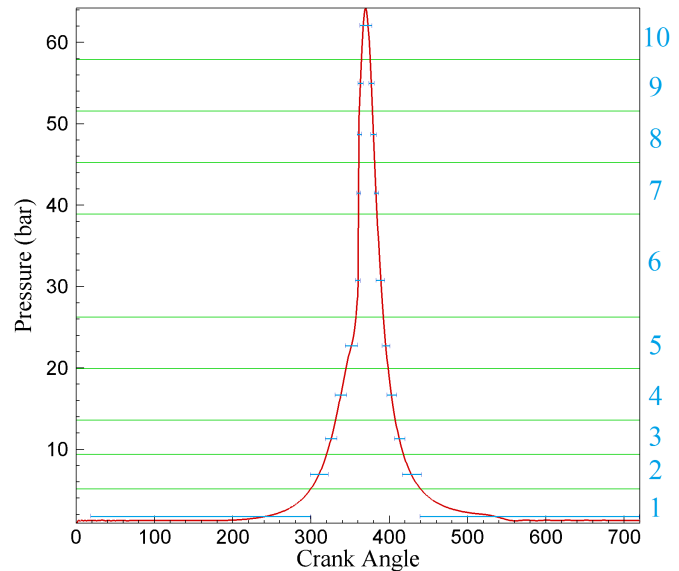


Figure 4.13 Binned pressure trace

The simulation of the flow in the cylinder kit assembly is divided into two main parts. First the 2D results of the problem is considered where a thin slice of the geometry is cut and simulated using the aforementioned boundary and fluid conditions. Because of the relative reduction in computational grid cells in the 2D geometry, the decrease in the simulation time is exploited to analyze the flow in the crevice regions and around the rings where the gradients are larger. However, the

3D effects as well as the ring end gap effect on flow field could not be established in this method. Therefore the complete 3D geometry of the ring pack is simulated to resolve the circumferential flow where different approaches were applied.

In the steady approach, the flow is considered to be steady for each bin pressure and the flow field is simulated until a steady state is reached for each bin pressure individually. The flow field for the whole cycle is evaluated by adding up the results of each bin. This will allow the solution of each bin to be performed independently, resulting in a faster simulation time.

In the transient method the input pressure is assumed to vary with time and therefore the in-cylinder pressure is computed for each time according to the engine RPM and applied at the inlet. The flow is then solved by marching in time and the results are calculated for each timestep. This method will not only resolve the 3D effects of the flow but also is capable of explaining the blow-by and blow-backs and quantify them for each crank angles; However, this approach requires more time to analyze the flow and depends on the total number of grid cells.

In the following sections the flow parameters that were computed using the above methods are discussed. First the 2D results are presented and then the 3D solutions are considered.

4.2.1 2D Results

In this section, the flow field is briefly examined by exploring the velocity profile and the mass flow rate of bin pressure #1. Air with 77% Nitrogen and 23% Oxygen composition is allowed to pass from the inlet surface of the geometry to the outlet. The 2nd grid system from 3.1 were chosen where the flow is solved unsteady while the inlet pressure was set constant and equal to 1.6926 *bar* according to Table 4.3. The k- ϵ turbulent model was employed and consequently the law-of-wall boundary conditions were used to model the flow adjacent to the wall. STL files are only available in three dimensions and therefore a thin section of the geometry with periodic boundary conditions and thickness of 0.2207 *mm* were simulated to remove any perpendicular variation of the flow. The above thickness represents a 0.5 degree slice of the complete 360 degree geometry.

The simulation timestep were set to vary between 1×10^{-8} and 1.0 seconds which is adjusted

automatically based on CFL numbers. The simulation was carried out at MSU HPCC with 16 processors and 250 Gbytes of RAM. The results were post processed by home written codes, Tecplot 10.0 [86] and Ensignt 10.2 [87] and the flow parameters were extracted and plotted mainly by Ensignt.

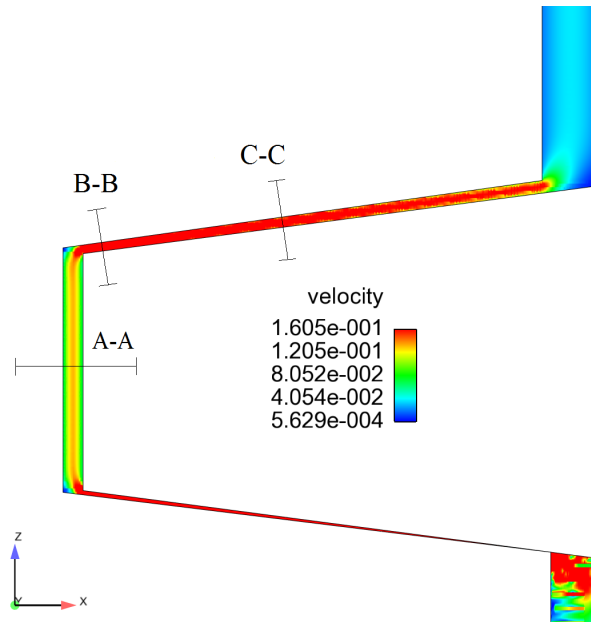


Figure 4.14 Velocity field around the first ring in 2D simulation

4.2.2 2D Velocity Profile

The velocity profile of the gas flow for the inlet pressure of first bin in the first ring is shown in Figure 4.14. It has been observed that the velocity increases between the ring and groove surfaces as expected. The velocity profile of the cross section of A-A, B-B and C-C of Figure 4.14 is shown separately in Figures 4.15, 4.16 and 4.17 respectively. It is discovered that the velocity increases on the upper surface of the ring and decreases behind it.

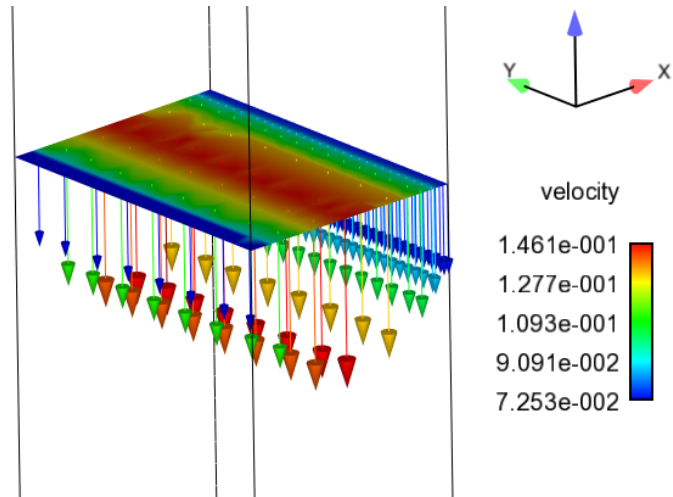


Figure 4.15 Velocity profile at cross section A-A of figure 4.14

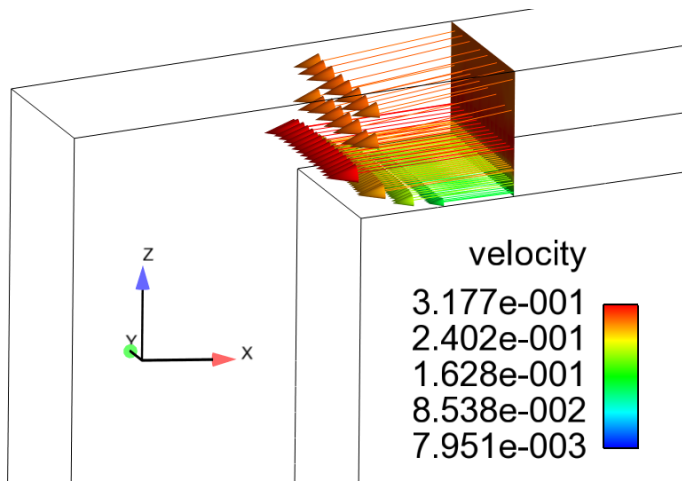


Figure 4.16 Velocity profile at cross section B-B of figure 4.14

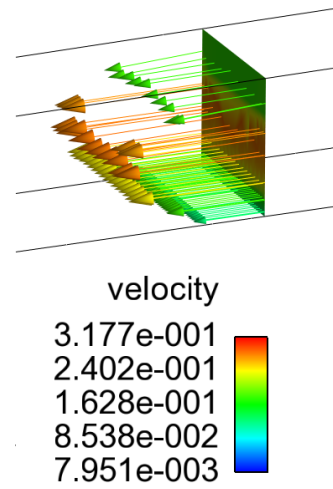


Figure 4.17 Velocity profile at cross section C-C of figure 4.14

Because of the small clearance between the lower surface of the second ring and its groove, a small vortex forms that is shown in Figure 4.18.

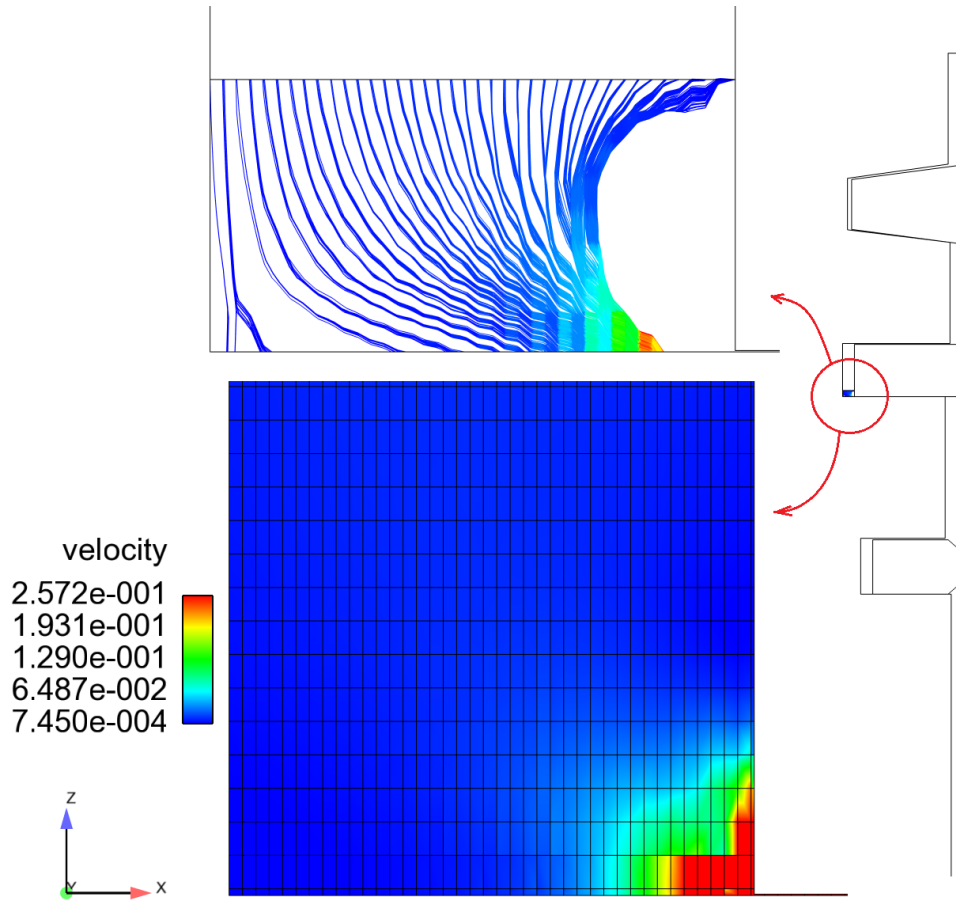


Figure 4.18 Velocity field around the second ring in 2D simulation

4.2.3 2D Blow-By calculation

In order to calculate the blow-by the results of the 2D geometry has to be translated to a 3D geometry. Since the thickness of the 2D geometry is 0.5 degree of the complete 3D geometry and the obtained mass mass flow of 2D geometry is 2.00×10^{-10} [kg/s], extrapolating this value will 1.4×10^{-7} [kg/s]. Therefore, The output mass flow rate of bin #1 pressure calculated by the 2D approach is 1.4×10^{-7} [kg/s] as opposed to the value of 1.2×10^{-6} [kg/s] computed by 3D-steady approach. A quick comparison between the obtained results reveals that there is an order of magnitude difference between the mass flow rates. The disparity between the results comes form the higher restriction on the flow in 2D approach compared to the 3D approach because of removal of ring end gaps. Therefore, it can be concluded that ring end gap has a substantial effect

on predicting the blow-by and its influence on the mass flow rate can not be neglected.

4.2.4 3D-Steady results

In this section the steady solution of the 3D geometry flow field is presented. Verification of the evaluated flow parameters are done by comparing the obtained results with the solution of the available 1D models i.e. CASE. Pressure distribution and blow-by is calculated using the steady approach to the problem which is discussed in sections 4.2.4.1 to 4.2.4.4.

4.2.4.1 Convergence of the results

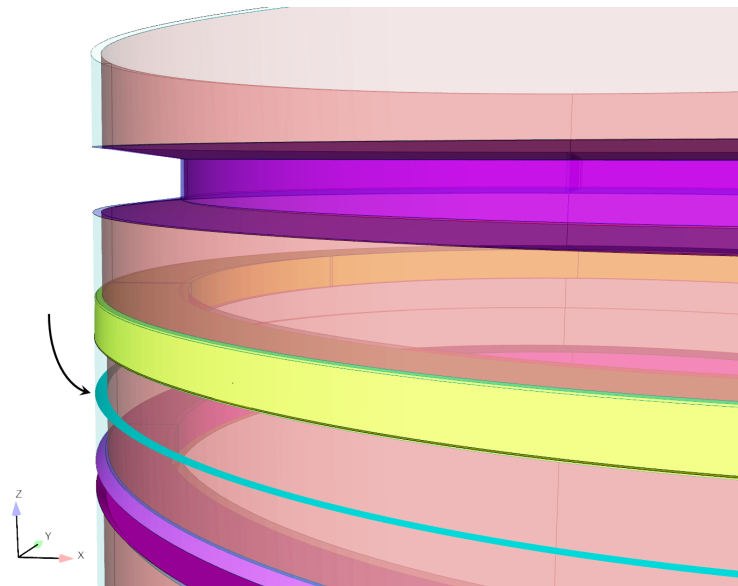


Figure 4.19 Averaging surface that cuts geometry in z direction, shown by green color

In the steady approach, the steady state solution is reached when the flow parameters do not change with time. This is confirmed by monitoring the averaged pressure and velocity at different axial locations with respect to time or by tracking the outlet mass flow rate variation with time. The flow parameter averaging is performed over a circular surface that cuts the geometry in z direction and shown in Figure 4.19.

The variation of averaged pressure versus time is shown in Figure 4.20 for different bin pressures and z locations. This graph indicates the development of steady-state solution when the tails become constant. It should be noted that the time axis in Figures 4.20 & 4.21 does not represent the simulation time, but rather measures the progress of steady-state solution. Since the transient solver of CONVERGE were utilized to simulate the flow, the simulation time is merely the transient solver time step. The same behavior is also observed when the averaged axial velocity is plotted versus time as depicted in Figure 4.21.

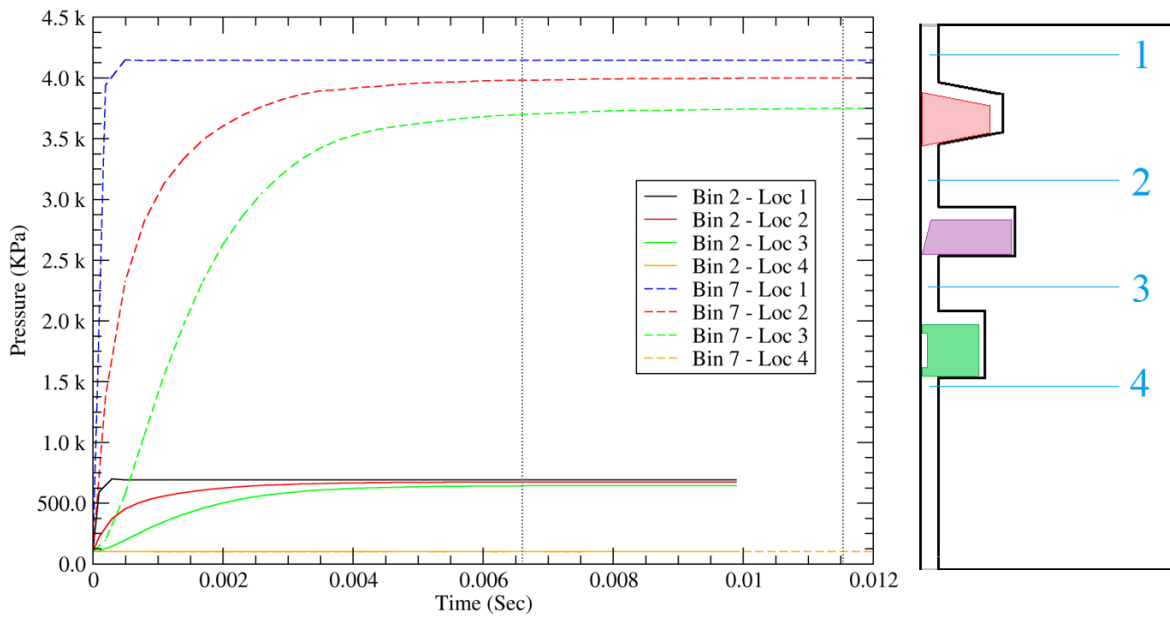


Figure 4.20 Average pressure vs. time for 3D-steady simulation at different locations and pressure bins

A useful inspection of the validity of the results is to check the conservation of mass and confirm if the continuity equation holds for the final results. The same cut surface that is introduced in Figure 4.19 is located at the inlet and outlet of the geometry and the density and velocity is averaged over the surface. By measuring the surface area of the cut surface, the mass flow rate can be computed from equation (4.1).

$$\rho \cdot V \cdot A|_{inlet} = \rho \cdot V \cdot A|_{outlet} \quad (4.1)$$

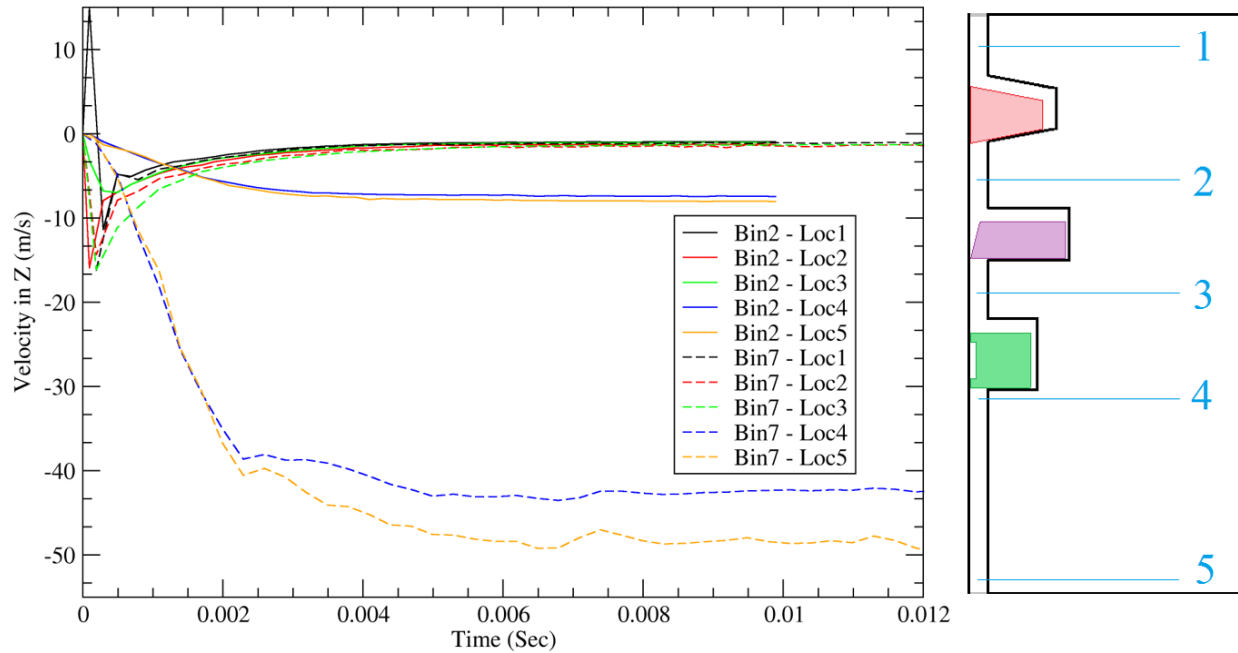


Figure 4.21 Average axial velocity vs. time for 3D-steady simulation at different locations and pressure bins

The Reynolds [88] number was calculated using equation (4.2).

$$Re = \frac{\rho V D}{\mu} \quad (4.2)$$

where ρ is the gas density, V is the magnitude of velocity, D is the characteristic length and μ is the viscosity.

By assuming the Distance between the bore and the cylinder as the characteristic length and calculating the air density at $300^{\circ}k$ the Reynolds number is evaluated as below:

$$D = 0.0004m \quad , \quad \rho = 1.846 \times 10^{-5} kg/m^3 \quad (4.3)$$

The range of the Reynolds number over the cut surface is shown in Figure 4.22 and Figure 4.23. It is found that Reynolds number stays less than 700 throughout the simulation for the inlet pressure of bin #1.

Although the flow is not turbulent but the addition of turbulent model will help with the stability of the CFD solver by introducing artificial diffusion to the system of equations.

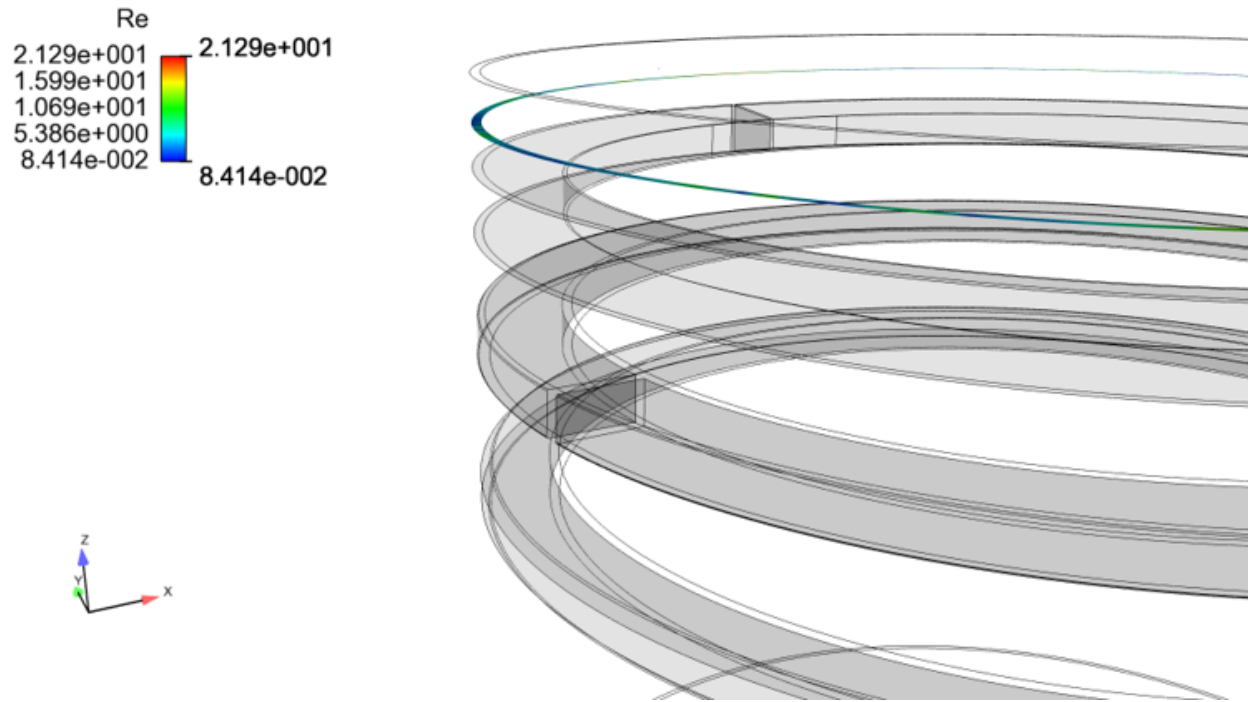


Figure 4.22 Variation of Reynolds number over the cut surface - first land

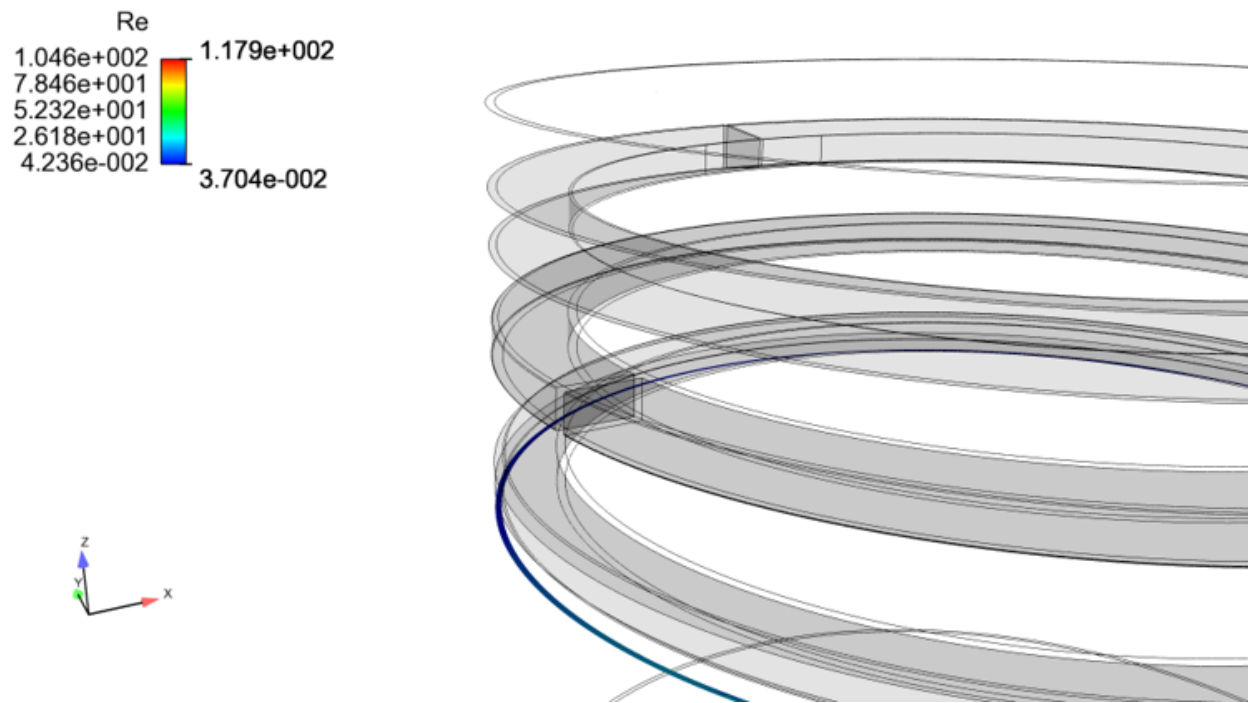


Figure 4.23 Variation of Reynolds number over the cut surface - skirt

4.2.4.2 Pressure distribution

The pressure distribution across the length of the piston in the domain of the problem, is found for different bin pressures and were compared with the answers from CASE solution. Since the results from CASE is only evaluated in 1D and are only available at certain locations across the piston, the obtained pressure is averaged circumferentially over a cut surface that is shown in Figure 4.19. By changing the location of the cut surface vertically, the averaged pressure can be found at different locations. Three different inlet bin pressures were chosen from Table 4.3 and the CASE results and current results were compared at the locations that CASE results were available (see Table 4.4).

CASE is only capable of predicting the pressure at certain important locations across the ring pack that are shown approximately in Figure 4.24. Because of the capability of the current simulation to predict pressure at any given z direction, three pressures were reported for first groove to show that the pressure variation across the first groove is large and can not be presented by only one pressure.

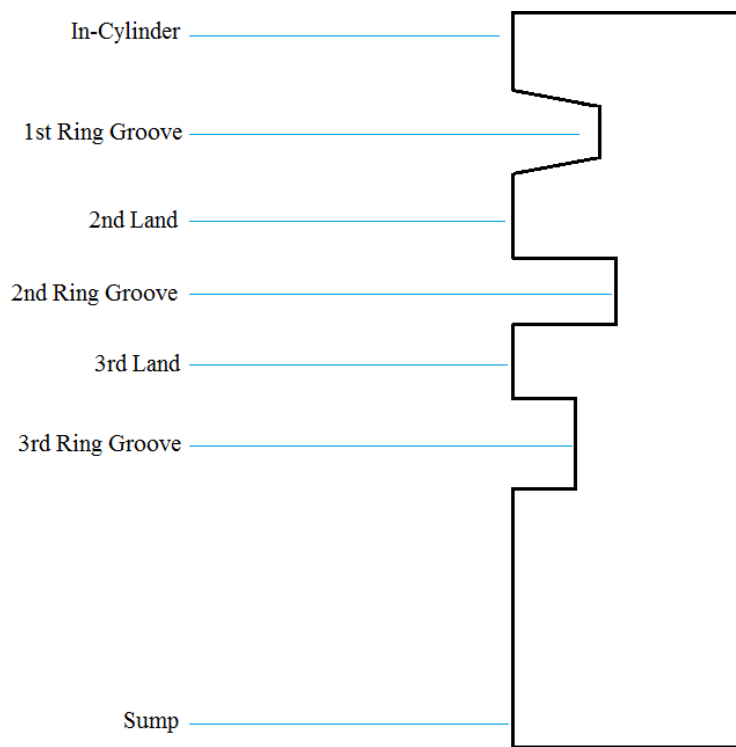


Figure 4.24 Location of calculated pressure across the piston using CASE

Bin10		Bin3		Bin 1		
3D-Steady	CASE	3D-Steady	CASE	3D-Steady	CASE	Loc
3 129 546	3 080 610	896 167	886 709	248 048	250 890	1
2 840 948	3 085 725	860 051	883 880	220 092	250 442	2
1 262 797		397 877		146 320		3
1 205 828		388 088		133 341		4
695 979	510 029	225 099	156 083	133 340	109 503	5
415 353	509 658	165 896	120 322	126 961	109 465	6
103 704	136 463	102 027	119 105	101 916	101 449	7
102 659	102 465	101 446	101 311	101 464	101 345	8
101 325	101 281	101 325	101 281	101 325	101 281	9

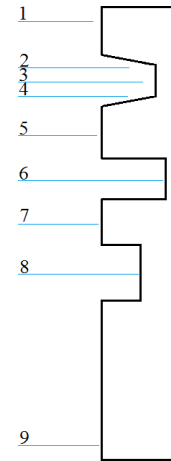


Table 4.4 Comparison between the 3D-steady and CASE pressure results (pressures are in *kPa*)

The averaged pressure calculated from current study and the predicted pressure from CASE calculations are shown in Table 4.4 for different in-cylinder pressures. It is found that the variation of the pressure across the top groove is substantial and which is not captured in CASE. Therefore, three pressures are reported for the first groove pertaining to the top, middle and bottom part of the first groove.

The disparities between the CASE and 3D-steady approach results arises from two facts. The circumferential variation of the pressure that is prominent at ring end gap is completely disappeared when the averaged pressure is calculated. Additionally, the leakage and discharge coefficients that should be set in CASE, are found empirically while in this study, there is no need to set any experimentally driven coefficients.

Whenever a ring is seated against the top or bottom of its groove, a perfect seal is not always accurate. The LEAKAGE data line is used in CASE to define the sealing coefficients between rings and grooves by defining the leakage area between the ring and its groove whenever it is seated at the top or bottom of its groove. The flow of gas through the ring end gaps is calculated using orifice method that requires a discharge coefficient. This value is set via DCOEF dataline in CASE.

The effect of ring leakage on the pressure profile is investigated by changing the leakage area of the second ring. The second ring is moved by 10% to increase the area between the lower surface

of the ring and lower surface of the groove. It is found that different configuration of leakage area can change pressure profile and consequently the mass flow rate in a cylinder kit assembly. As shown in Figure 4.25 the pressure profile is decreased in the areas surrounding the 2nd ring when the leakage area is increased.

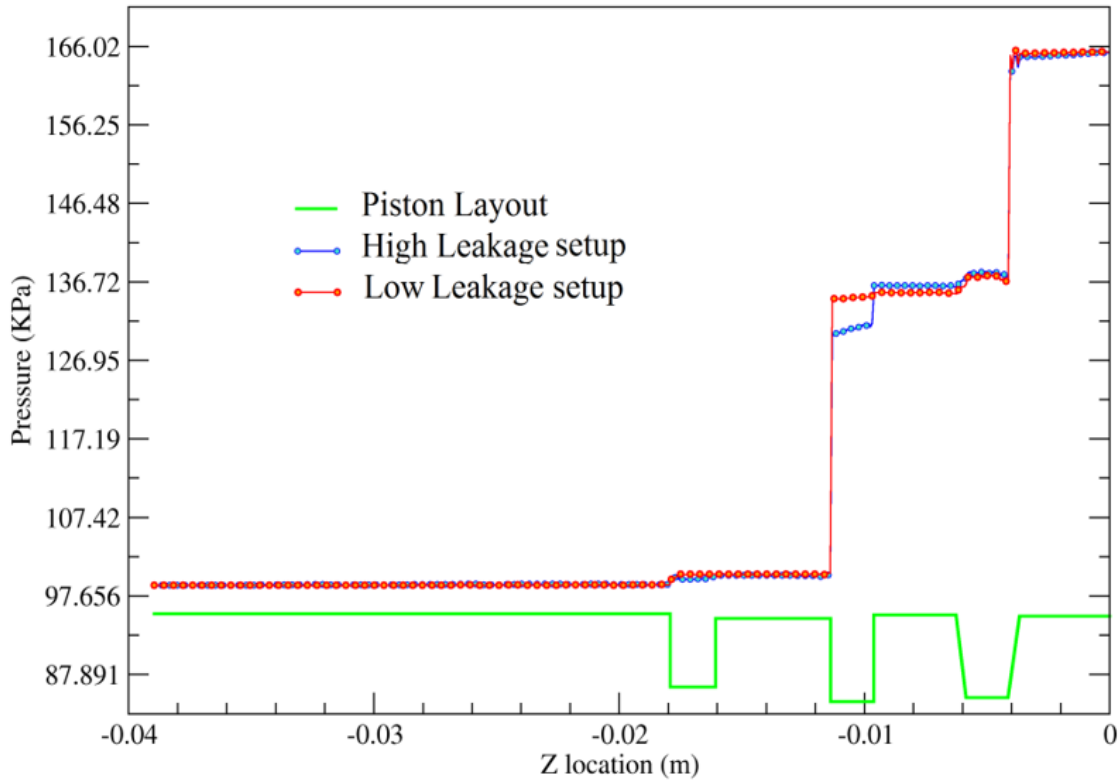


Figure 4.25 Pressure profile for similar cylinder-kit assemblies but different 2nd ring leakage area

4.2.4.3 Circumferential flow

An important advantage of a 3D simulation is the capability of resolving 3D effects of flow. In particular, the circumferential flow between the rings, grooves and lands can greatly impact the blow-by and heat transfer rate.

The circumferential flow in the studied ring pack geometry were obtained using the 3D-steady approach and the flow streamlines were plotted and colored according to the magnitude of velocity. An example of flow field inside the ring pack for bin pressure of #1 is shown in Figures 4.26 through 4.29. As shown in Figure 4.26, four vortices form on the 2nd land below the 1st ring end

gap. On each side of the ring end gap, two vortices are visible that rotate in opposite directions. This causes a substantial percentage of the gas to flow in circumferential direction in the second land.

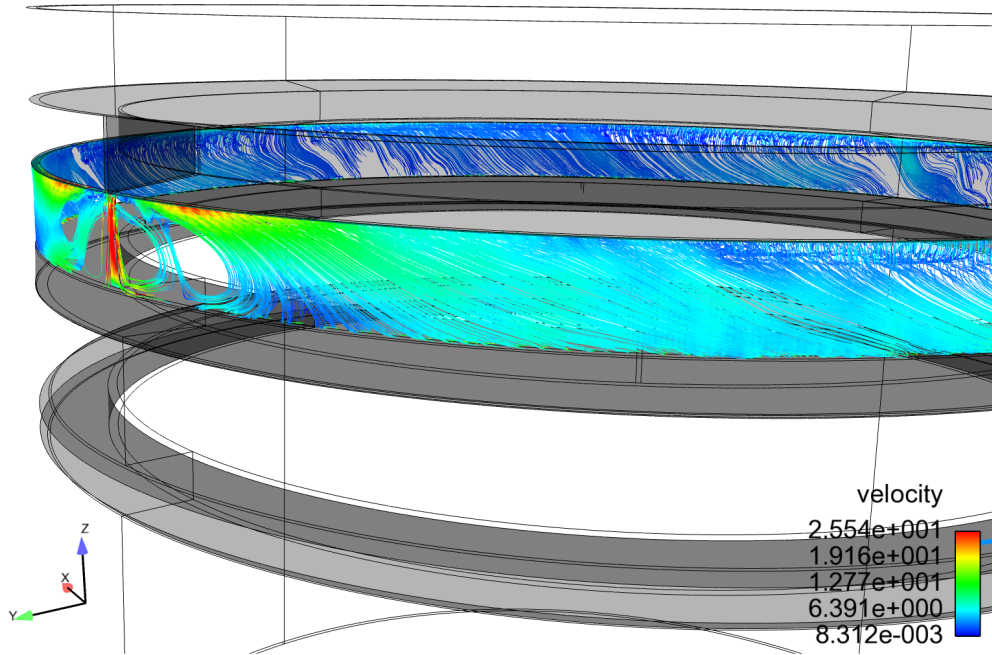


Figure 4.26 Circumferential flow in 2nd land

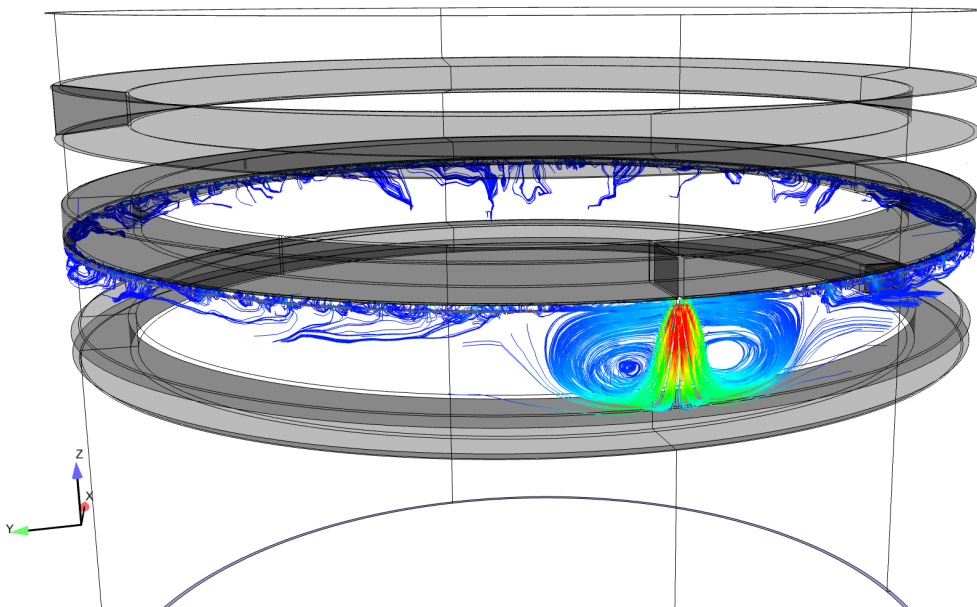


Figure 4.27 Circumferential flow in 3rd land

As shown in Figure 4.27 the same conditions are true for the 3rd land but only one vortex forms on each side of the 2nd ring end gap.

In order to compare the effect of ring twist on the flow field and particularly the circumferential flow, the 2nd ring is twisted according to Cheng et al. [61]. The velocity streamlines in the 2nd and 3rd lands are shown in Figures 4.28 and 4.29 respectively. The same flow structures that were observed in the untwisted ring geometry, is also observed here. Vortices are formed in the 2nd and 3rd lands right after the 1st and 2nd ring end gaps.

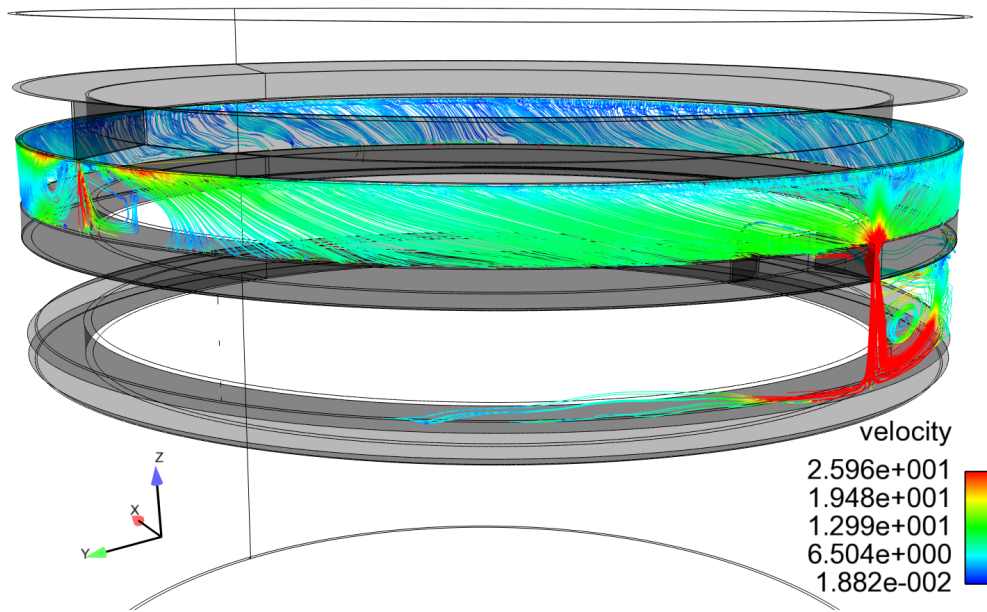


Figure 4.28 Circumferential flow in the 2nd land with twisted 2nd ring

It can be concluded that the ring twist has little impact on the circumferential flow while the ring end gaps geometry and their respective location with each other plays an important role in determining the circumferential flow in cylinder kit assembly.

The instantaneous mass flow rate is calculated for the cylinder-kit of inlet pressure of bin #1 for the twisted and untwisted second rings and plotted in Figure 4.30 using the 3D-steady approach.

The above result, suggests that the flow rate decreases in the 1st land when the 2nd ring is twisted. This is because of the decrease in the crevice volumes which causes smaller leakage areas around the second ring and consequently decreases the mass flow rate. This conclusion is

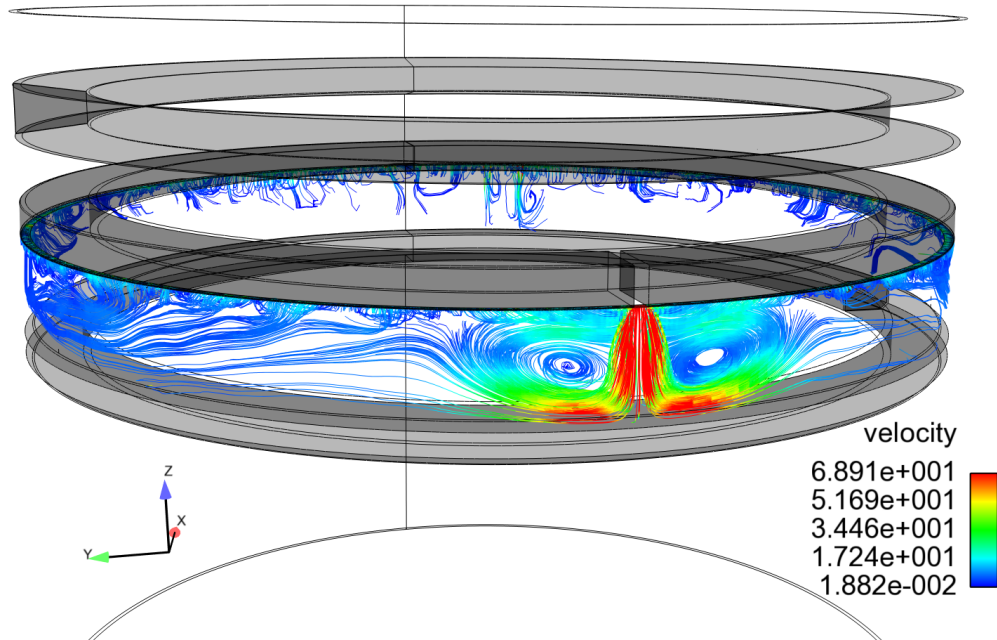


Figure 4.29 Circumferential flow in the 3rd land with twisted 2nd ring

case sensitive and a different cylinder-kit setup can results in a completely different mass flow rate behavior when the rings are twisted (i.e. an increase in mass flow rate for the twisted ring geometry).

4.2.4.4 Blow-by calculation

A crucial measurement that is mostly associated with the cylinder-kit assembly design is the blow-by. Calculation of blow-by requires measurement of the amount of the gas that passes from the combustion chamber through the ring pack into the crank case during a complete cycle. After solving the flow for each bin using the 3D-steady approach, the blow-by is calculated by summing the mass flow rate that goes through the outlet boundary, over the whole cycle. A program is developed to extract flow parameters form the last layer of the computational cells that are closest to the outlet boundary condition. Velocity vector and surface areas were calculated and the mass flow rate were computed as below:

$$\dot{m} = \rho \mathbf{V}_n A \quad [kg/s] \quad (4.4)$$

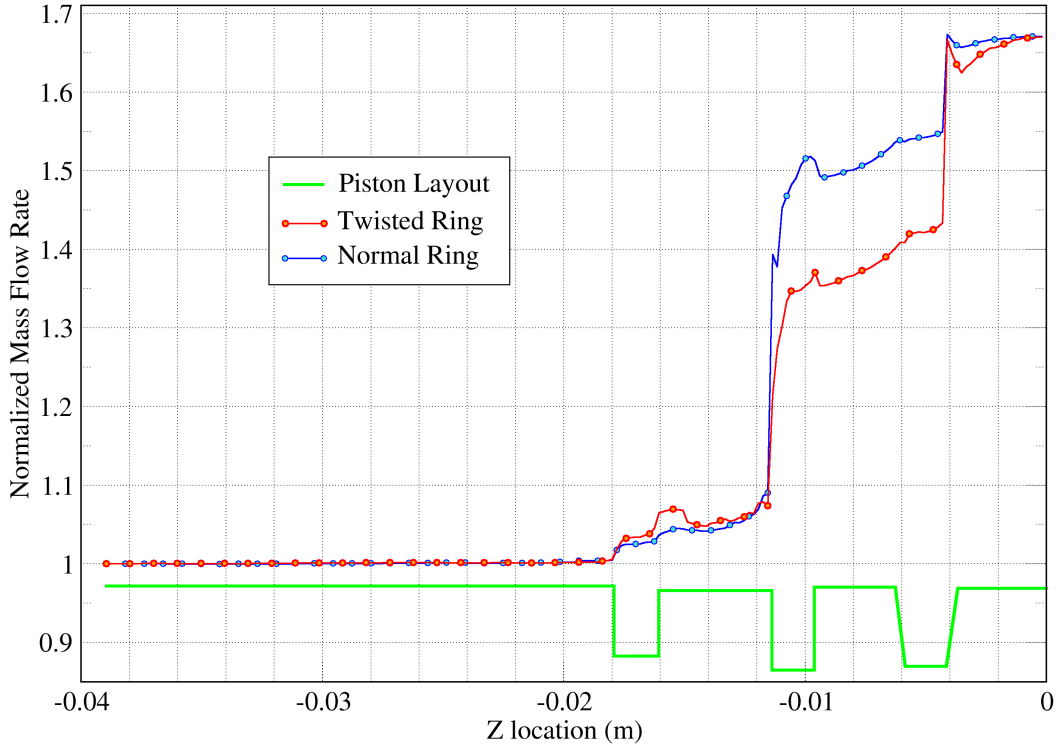


Figure 4.30 Mass flow rate comparison in twisted and untwisted 2nd ring geometries

Where A is the surface area of the outlet boundary and \mathbf{V}_n is the component of the velocity perpendicular to the surface.

Mass flow rate for each bin pressure is then multiplied by its weight and summed over total bins to evaluate the blow-by for the whole cycle:

$$\dot{m}_{cycle} = \sum_{bin\#1}^{bin\#10} \dot{m}_{bin} \times w_{bin} \quad (4.5)$$

Bin weight is the total number of crank angles that fall in the same bin and is found from Table 4.3. The final step is to convert the mass flow rate from $[kg/s]$ to $[liter/min]$ which requires the dependency of the density of the air on the temperature to do the conversion. In this study $1.177 [kg/m^3]$ were employed as the conversion factor which is the air density at $300 \text{ }^\circ\text{K}$ and 101325 kPa . The mass flow rate for each bin pressure is calculated and reported in Table 4.5.

By having the crank angles that each bin encompasses and knowing the RPM of the engine, the associated time for each bin pressure can be found as shown in Table 4.6. The *spent time in each bin* is calculated by counting the total number of crank angles in which the inlet pressure falls

Bin #	Pressure (Pa)	\dot{m} (kg/s)
1	169 260	7.15E-05
2	691 650	0.0004775
3	1 129 900	2.22E-05
4	1 664 080	0.001331
5	2 273 340	1.84E-03
6	3 078 040	0.0026455
7	4 146 080	3.69E-03
8	4 863 530	0.0044126
9	5 493 570	0.005048326
10	6 210 780	0.005764691

Table 4.5 Calculated mass flow rate for each bin pressure

within the same bin. For example 580 out of 720 crank angles of the complete cycle falls inside bin #1 and therefore the spent time is $(580/720)$ % of the cycle time.

Bin #	Pressure (bar)	C.A.s	Time spent in bin (sec)	
1	1.6926	[1-299] , [440-720]	580	0.048333
2	6.9165	[300-319] , [419-439]	41	0.003417
3	11.299	[320-331] , [408-418]	23	0.001917
4	16.6408	[332-344] , [399-407]	22	0.001833
5	22.7334	[345-357] , [393-398]	19	0.001583
6	30.7804	[358-360] , [385-392]	11	0.000917
7	41.4608	382 , 383 , 384	3	0.00025
8	48.6353	361 , 379 , 380 , 381	4	0.000333
9	54.9357	[362-364] , [376-378]	6	0.0005
10	62.1078	[365-375]	11	0.000917
			Total=	0.06

Table 4.6 Calculated discharged mass for each bin pressure

The discharged mass for each bin can be easily calculated by having the time and mass flow rate of each bin. The blow-by is the summation of discharged mass divided by the total time of cycle converted to liter per minute.

In this study, the engines RPM is set to 2000 which takes 0.06 seconds to complete a cycle and results in a 136 [liter/min] blow-by.

4.2.5 3D-Unsteady results

In this approach, The same binning concept of section 3.4.1 is employed with a little modification. The pressure trace is divided into two main parts: steady and unsteady. As shown in Figure 4.31 The inlet pressure is assumed to be constant in regions 1 and 3 where the pressure is low and its variation is negligible while it is considered a function of time in region 2 where the its variation is high. Therefore, the simulation time of regions 1 and 3 will be dominated by the steady-state solution time which is generally lower than unsteady solutions while the simulation time of region 2 is controlled by the transient simulation time. This approach will benefit from the reduction of simulation time using steady-state solution in the regions where the variations are not substantial while uses the more detailed, accurate and time consuming unsteady solution in the regions where the gradients are larger. In Figure 4.31 the unsteady and steady regions are illustrated by red and green lines respectively. The evaluated constant pressure that is used in regions 1 and 3 is shown by a blue strait line.

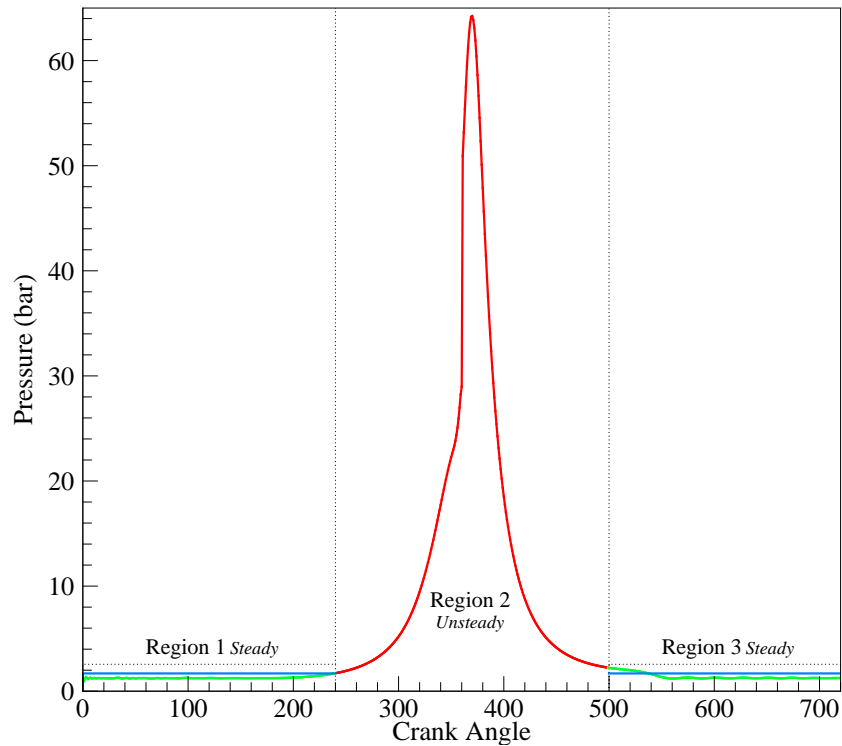


Figure 4.31 Different regions of pressure trace in 3D-unsteady approach

The Air composition is selected as 77% Nitrogen and 23% Oxygen and the Redlich-Kwong cubic equation of state (equation 3.9) is used to couple the density and temperature of air. Flow is assumed to be turbulent in all regions with $k - \epsilon$ model. Unsteady solver is employed for all regions. The flow is solved until fully developed condition is reached in steady regions and solved until the ending simulation time is reached in unsteady region. The same boundary conditions that was explained in sec 3.4.3 is employed for each regions separately. The inlet pressure for steady regions are set to a constant value while the unsteady region utilizes a temporal description of the in-cylinder pressure that follows the pressure trace associated with the engine RPM time. The simulation was carried out at MSU HPCC with 16 processors and 250 Gbytes of RAM. The results were post processed by home written codes, Tecplot 10.0 [86] and Ensign 10.2 [87] and the flow parameters were extracted and plotted mainly by Ensign. In the following sections the main conclusions are discussed

4.2.5.1 Blow-by calculation

Similar to the section 4.2.4.4, blow-by is calculated by summing the total mass flow rate that goes through the outlet boundary, over the complete cycle. The total discharged mass from regions 1 and 3 are found by multiplying the mass flow rate by the time spent in each regions while the discharged mass from unsteady region is found by integrating the area under the mass flow rate versus time graph. This graph is shown in Figure 4.32 where the pressure trace is shown on the top and the mass flow rate is depicted on the bottom part.

The total mass flow rate of the cycle is then calculated by dividing the summation of discharged mass form all the regions by the time of taken by each cycle to complete. Therefore, blow-by equals to:

$$\dot{m} = 7.08 \times 10^{-5} [kg/s] = 50.1 [Litre/min] \quad (4.6)$$

An interesting representation of the blow-by is to calculate the discharged mass per cycle for current engine RPM. Each cycle requires 0.06 seconds to complete for the engine at 2000 RPM.

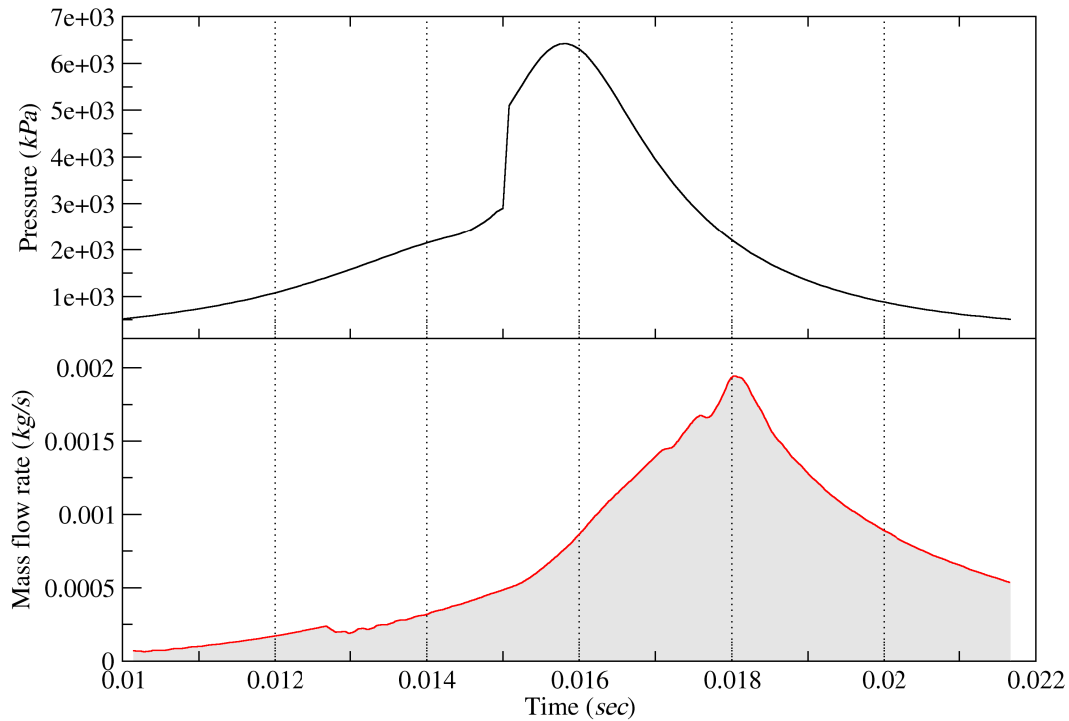


Figure 4.32 Mass flow rate in Region 2 in 3D-unsteady approach

Therefore:

$$\dot{m} = 0.4248 \times 10^{-5} [\text{kg}/\text{cycle}] \quad (4.7)$$

4.2.5.2 Blow-back

Blow-back (or sometimes referred as reverse blow-by) is the amount of gas that blows back from the inter-ring pack to the combustion chamber. Blow-back is found to play an important role in determining the oil consumption in Internal combustion engines. As researches show, oil consumption in ring pack has three ways: oil evaporation, oil throwing and oil blowing. The third one is the major of oil consumption. Therefore, the blow-back through ring pack is the key point to reduce oil consumption, and needs to be strictly controlled [89]. Therefore, a great deal of attention is focused on improving blow-back through top ring to reduce oil consumption and pollutant emission.

One of the important outcome of the 3D-unsteady approach is the prediction of blow-back that could help in minimizing the oil consumption in an engine. Quick observation of the flow in this

study reveals that the blow-back increases as the in-cylinder pressure decreases from its peak value (i.e. crank angles larger than 360 in Figure 4.31). Because of the pressure difference between the 1st and 2nd land, an upward jet of flow forms at the 1st ring end gap that drives the flow to the combustion chamber. This information can be useful in determining the oil source in studying the super knock phenomena in internal combustion engines [90]. The blow-back at two different times are shown in Figure 4.33 and 4.34.

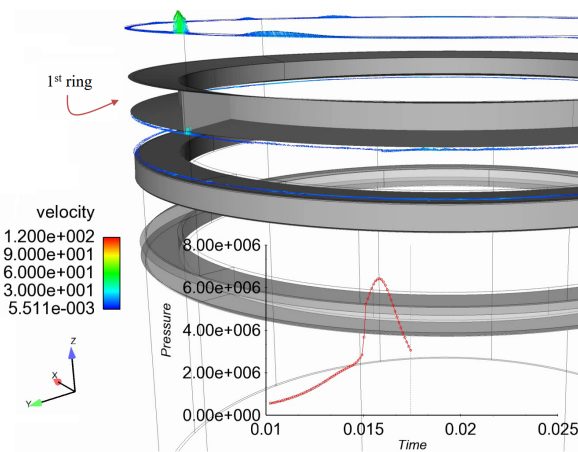


Figure 4.33 Velocity profile at the inlet showing blow-back

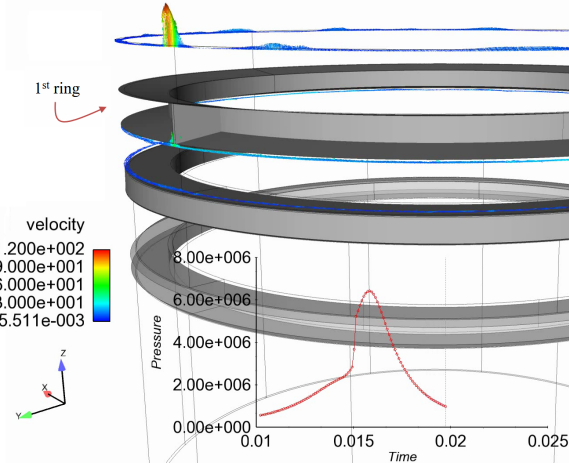


Figure 4.34 Velocity profile at the inlet showing blow-back

4.3 Conclusions

In this dissertation the flow inside a cylinder-kit assembly is calculated using a CFD model. The geometry of the problem is created via LINK program which includes the geometrical details of the cylinder-kit such as ring twist, bore distortion, ring/bore and ring/groove conformability. LINK creates arbitrary geometry of cylinder-kit assembly in an automated way and converts the surfaces into STL format. CONVERGE was employed to solve the flow field where different approaches were employed. The computational domain is discretized using the built-in grid generator of the CONVERGE that creates a structured grid.

In the first approach, Using a "Binning" concept, the in-cylinder pressure is divided into finite number of bins with different sizes where the pressure is assumed to be constant. Each bin is

considered a separate problem and the flow is assumed to be steady with constant inlet pressure. Air is used as the working fluid and the steady state is presumed when the fully developed condition is achieved. The comparison between the calculated pressure using this approach and the results of CASE simulation shows a good agreements between the outcomes of both models. Blow-by is predicted by summing the mass flow rate that goes through the outlet boundary, over the whole cycle. This is done first by determining the discharged mass from the outlet boundary for each bin separately and then dividing the total discharged mass by the total cycle time to calculate the blow-by.

In the second approach the pressure trace is considered a function of time and the flow is assumed to be unsteady. The blow-by calculated by this approach is found to be smaller than the value predicted by the steady approach mainly because of the overestimation associated with the steady assumption. Due to the large variation in the pressure trace, the mass flow rate changes drastically near the peak value of the pressure curve. In the unsteady approach, there is not enough time for the flow to fully develop when pressure gradient is at its maximum value (i.e. near the peak value of pressure trace) while in the steady approach, each bin is solved separately until fully developed flow is achieved that requires the flow to be fully developed and therefore increasing the mass flow rate computation. Among other results of this approach, prediction of blow-back is a major outcome that plays an important role in quantifying the transport processes by which oil is consumed by engines. It is found that the blow-back is significant and the gas continues to blow back into the combustion chamber well after the peak value of the pressure trace curve.

4.3.1 Wall clock time

The 3D-steady approach requires 48 hours to complete simulation for each bin pressure. Since each bin pressure can be considered a separate problem, simultaneous simulations of the different geometries with different boundary conditions are possible. Therefore, the flow can be simulated for the whole cycle in 48 hours. in another word, the whole cycle simulation time depends on the maximum simulation time of each bin-pressure.

On the other hand, the 3D-unsteady approach that consists of three different regions, requires more time compared to the 3D-steady approach. The simulation in each region is carried out one after another because the results of each regions is used to initialize the next region and therefore, the whole cycle simulation time is the summation of simulation time of each regions. The steady regions (regions 1 & 3) requires 24 hours to complete the simulation while the unsteady region (region 2) need 108 hours. When compared to the 3D-steady approach the whole cycle simulation for 3D-unsteady approach is 3.25 times longer.

All the simulations were performed at HPCC at MSU and the simulation times were calculated based on the available hardware.

4.3.2 Flow structure

An important advantage of a 3D simulation is the capability of resolving 3D effects of flow. Aside from prediction of blow-by and blow-back, the circumferential flow were obtained using the 3D-steady approach which was not simulated before. It is observed that the ring end gaps geometry and their respective location with each other characterizes the circumferential flow in cylinder kit assembly. Moreover, the velocity vectors were found to be about 45 degree in the 2nd land, implying equal axial and circumferential velocity magnitude in the region. It is also found that in our setup the ring twist has negligible effects in changing the circumferential flow behavior while it can be significant by changing the clearance volume and hence increasing the mass flow rate. This is shown by measuring the instantaneous mass flow rate, pressure profile and examining the flow field in the 2nd land for normal and twisted 2nd ring. It is concluded that, although the flow structure remains almost the same, the mass flow rate decreases by 13% when the 2nd ring is twisted.

4.3.3 Blow-by and blow-backs

Blow-by and Blow-back is among the primary outcomes of this study. Blow-by is calculated using both 3D-steady and 3D-unsteady approaches. It is observed that the blow-by is overestimated in 3D-steady approach which can be caused by the assumption that flow is considered steady for each bin pressure. This requires the fluid to reach fully develop condition to reach a steady state. However, in reality the flow parameter gradients are so high that flow does not reach a fully developed condition. The blow-by prediction in 3D-steady approach, is 2.7 times larger than 3D-unsteady approach which shows the importance of unsteady assumption in accurate calculation of blow-by.

Blow-back is calculated using 3D-unsteady approach. It is found that the blow-back is significant and the gas continues to blow back into the combustion chamber well after the peak value of the pressure trace curve. Tracing the fluid particles reveals that part of the fluid that exist in the 1st and 2nd is blown back to the combustion chamber via the 1st ring end gap and the fluid in 3rd land do not find their ways to the combustion chamber.

The knowledge from this study should lead to a better understanding of the flow phenomena in the piston ring pack and can be used for further calculations containing oil flow such as oil consumption.

CHAPTER 5

SUMMARY, CONCLUSIONS AND FUTURE WORK

5.1 Summary

In this dissertation, numerical models for the assessment of cylinder-kit performance of four-stroke internal combustion engines were explored. A novel 3-D numerical model for predicting the gas flow through cylinder kit assembly was examined and a program was developed to link the output of the CASE program to CONVERGE. Both steady and unsteady approaches were considered and the advantage and disadvantages of each methods were discussed. Pressure distribution and blow-by were calculated by utilizing CONVERGE as the CFD flow solver while pressure binning method was used to reduce the computation cost. It is found that a complete 3D solution that takes into account all of the flow behavior effect is extremely time consuming. However, it is shown that the introduced approximations in setting up the model can greatly decrease the simulation time at a negligible accuracy lost expense.

The calculation of circumferential variation in pressure and velocity, is the first noticeable results captured by current model. This will enhance the understanding of the effect of ring end gap and ring twist on the flow behavior. Blow-by and blow-back are among other important outcome of this study. In fact, blow-back that measures the thrown back gas from ring pack to the combustion chamber can only be calculated accurately if a 3D model is employed. Moreover, a quick comparison between the CASE results and the proposed 3D approach shows good agreements in the predication of the pressure field.

5.2 Future work

The main drawback of the proposed model is the simulation time which inhibits the user to implement it for further optimization schemes. This is mainly because of first, the high complexity level

of the geometry that requires a very small grid size to accurately model the crevice regions and second, the high in-cylinder pressure gradients that demands small marching time. Generally an optimization problem consists of maximizing or minimizing a variable by systematically choosing input values from within an allowed set and computing the value of the function. This will require multiple solutions of the same problem with different sets of variables in order to optimize the objective function.

Different ideas are proposed in sections 5.2.1 and 5.2.2 to remedy the above issue which mainly leads to decreasing the simulation time.

Another contributing factor in increasing the simulation time is the load balancing issue which is inherent in CONVERGE 2.3. The load balancing algorithm is explained in section 3.6.4. When the domain is subdivided into parallel load blocks, CONVERGE performs a load balance. Once the grid is created, the load balancing procedure assigns the block to the processors to achieve two main goals:

1. Balance the number of computations so that they are the same on all machines.
2. Minimize the amount of information that will need to be passed between machines by minimizing the block interface area, (i.e., group neighboring parallel blocks together on the same processor as much as possible).

This procedure is not robust for the systems that contains length scales with greater than 100 order difference in magnitudes such as cylinder kit assemblies.

5.2.1 Simplifying the geometry

Careful review of the CFD simulation reveals that the tiny areas between the ring surface and the groove that defines the leakage areas are responsible for determining the simulation speed of the problem. The vast difference in the existing length scales of the cylinder kit geometry presents major challenges in grid generation of the CFD solver. Fitting enough grids in the microscopic

regions requires small grid size that dominates the total simulation time. Therefore, by removing the tiny areas from the geometry, larger grid sizes can be utilized and consequently simulation time will be reduced. The process of removing small areas are shown in Figure which involves identifying the small areas based on a criteria, considering them as overlapping surfaces and finally removing them.

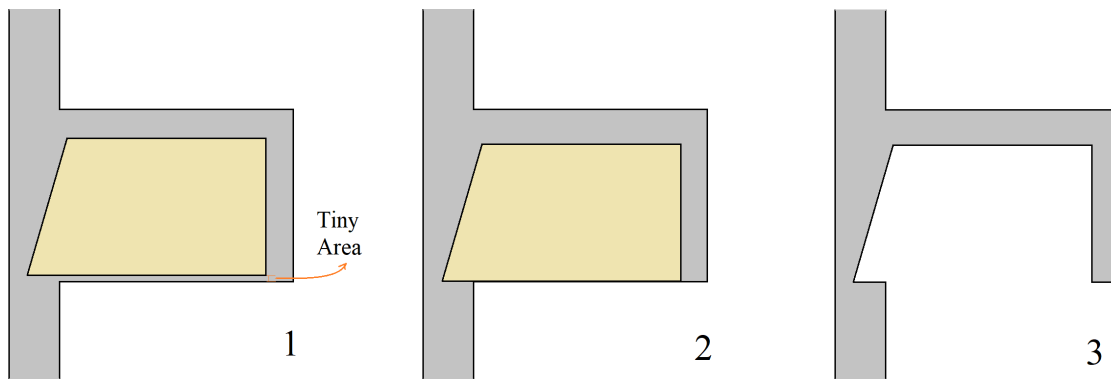


Figure 5.1 Removal procedure of the tiny areas in cylinder kit assembly

Modifying the geometry using the above procedure can potentially increase the minimum grid size 100 times larger than the original size which will drastically decrease the simulation time .

5.2.2 Alternative method

In this method, because of the symmetrical characteristic of the cylinder, Instead of considering the complete geometry, a slice of the problem is solved. A schematic view of a slice of geometry is shown in Figure 5.2 where the surfaces are colored differently.

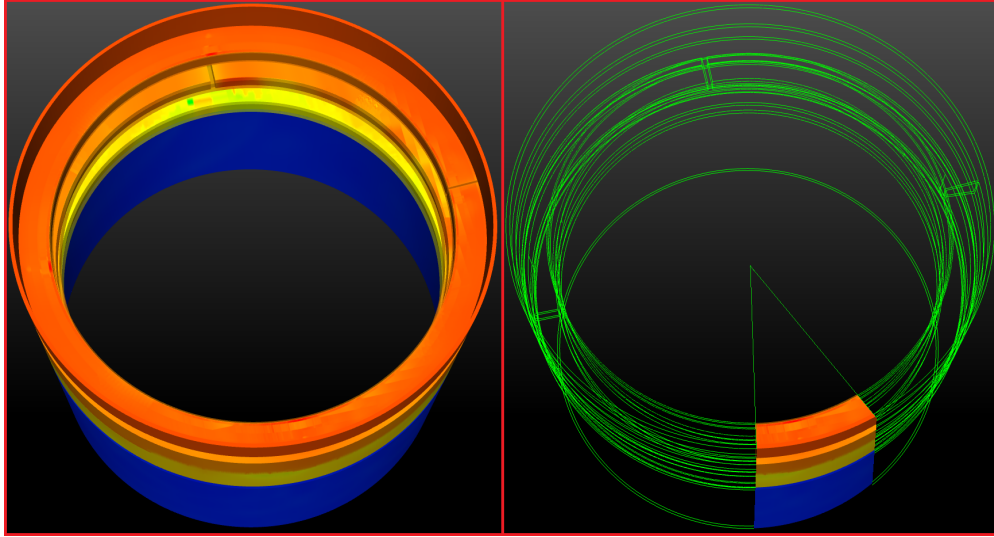


Figure 5.2 Sliced geometry of the full 3D geometry

The twist angle of the rings are assumed to be constant throughout the simulation slice but in order to account for the twist angle, various slices with different twist angle of the ring are solved. Then the final result is aggravated based on the weight of the twist angle. For instance, if a ring is installed in a groove and in a specific operating condition experiences three major twist angle across its circumference, three major geometries are solved to account for the twist angle. (see Figure 5.3).

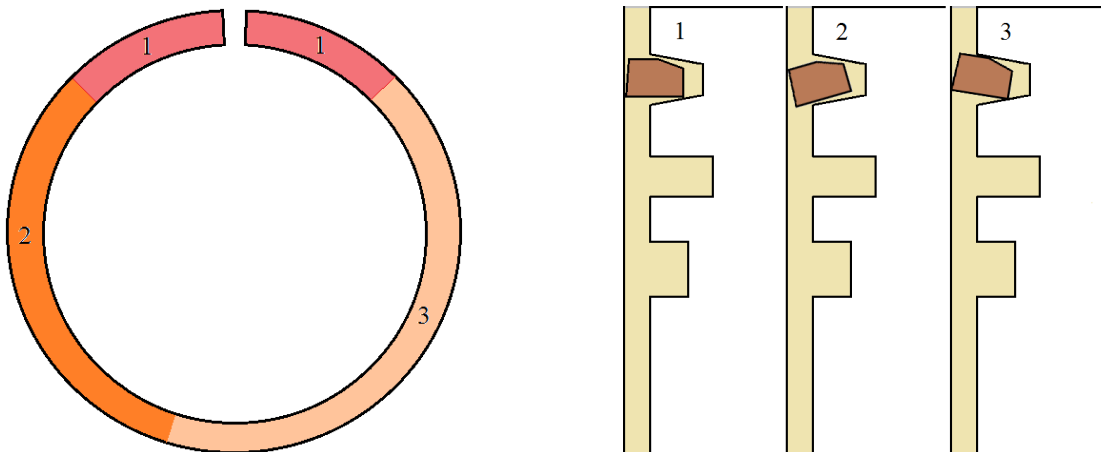


Figure 5.3 Various slices of the 3D geometry with different twisted 1st ring

5.2.3 Fluent as the CFD solver

Fluent can be used as an alternative CFD solver. This program has been used by engineers for almost two decades and more man-hours has been put in its development compared to CONVERGE. It is a powerful tool in load balancing and applying different models such as two-phase flow. However, the grid generation is not automatic in this program. Fluent can be employed to solve the two-phase flow that contains oil and gas in cylinder-kit assemblies. this can greatly enhance the capacity of this study to model the oil consumption in the ring packs.

BIBLIOGRAPHY

BIBLIOGRAPHY

- [1] AVL Products. Avl advanced simulation technologies, 06 2016. URL <https://www.avl.com/>.
- [2] Federal Mogul. Piston ring handbook. URL <http://korihandbook.federalmogul.com/en/index.htm>.
- [3] Marcus Kennedy, Steffen Hoppe, and Johannes Esser. Lower friction losses with new piston ring coating. *Auto Tech Review*, 3(10):30–35, 2014. doi: 10.1365/s40112-014-0760-1.
- [4] Alex Weiss. *Bearings*. Special Interest Model, Poole, 2008. ISBN 978-1854862501.
- [5] M Priest and C.m Taylor. Automobile engine tribology - approaching the surface. *Wear*, 241(2):193–203, 2000. doi: 10.1016/s0043-1648(00)00375-6.
- [6] Piston ring, Apr 2017. URL https://en.wikipedia.org/wiki/Piston_ring.
- [7] Max M. Roensch. Piston-ring coatings and their effect on ring and bore wear. 1940. doi: 10.4271/400143.
- [8] R Jakobs. Ein beitrag zur wirkungsweise von negativ vertwistenden minutenringen in der zweiten nut von pkw-dieselmotoren. *Fachschrift*, 41, 1988.
- [9] Shoichi Furuhashi and Hiroshi Ichikawa. L-ring effect on air-cooled two-stroke gasoline engines. *SAE Technical Paper Series*, 1 1973. doi: 10.4271/730188.
- [10] Yukio Tateishi. Tribological issues in reducing piston ring friction losses. *Tribology International*, 27(1):17–23, 1994. doi: 10.1016/0301-679x(94)90058-2.
- [11] Marlan Davis. Piston ring tech - the latest developments in cylinder sealing, 9 2008. URL <http://www.hotrod.com/articles/hrdp-0910-piston-ring-tech/>.
- [12] D. E. Richardson. Comparison of measured and theoretical inter-ring gas pressure on a diesel engine. *SAE Technical Paper Series*, Jan 1996. doi: 10.4271/961909.
- [13] Liu N., Zheng Z.C., and Li G.X. Analysis of the blow-by in piston ring pack of the diesel engine. *Chemical Engineering Transactions*, 46:1045–1050, Dec 2015. doi: 10.3303/CET1546175. URL <http://doi.org/10.3303/CET1546175>.
- [14] R. W. Miller. *Flow measurement engineering handbook*. McGraw-Hill, New York, 1996. ISBN 978-0070423664.
- [15] MAHLE GmbH. *Cylinder components : properties, applications, materials*. Vieweg+Teubner, Wiesbaden, 2010. ISBN 9783834807854.
- [16] Mikhail A. Ejakov, Harold J. Schock, and Lawrence J. Brombolich. Modeling of ring twist for an ic engine. *SAE Technical Paper Series*, 1998. doi: 10.4271/982693.

- [17] T. Tian, L. B. Noordzij, V. W. Wong, and J. B. Heywood. Modeling piston-ring dynamics, blowby, and ring-twist effects. *Journal of Engineering for Gas Turbines and Power*, 120(4): 843, 1998. doi: 10.1115/1.2818477.
- [18] T. Tian. Dynamic behaviours of piston rings and their practical impact. part 1: Ring flutter and ring collapse and their effects on gas flow and oil transport. *Proceedings of the Institution of Mechanical Engineers, Part J: Journal of Engineering Tribology*, 216(4):209–228, 2002. doi: 10.1243/135065002760199961.
- [19] Four-stroke engine, 4 2017. URL https://en.wikipedia.org/wiki/Four-stroke_engine.
- [20] Cheng Chao. *Numerical modeling of the power cylinder system for internal combustion engine with an emphasis on ring pack design*. Phd dissertation, Michigan State University, Mechanical Engineering Department, East Lansing, Michigan, USA, 2015.
- [21] Naoki Iijima, Tomohiro Miyamoto, Masaaki Takiguchi, Ryoji Kai, and Masaharu Sato. An experimental study on phenomena of piston ring collapse. *SAE Technical Paper Series*, 4 2002. doi: 10.4271/2002-01-0483.
- [22] Richard Mittler, Albin Mierbach, and Dan Richardson. Understanding the fundamentals of piston ring axial motion and twist and the effects on blow-by. *ASME 2009 Internal Combustion Engine Division Spring Technical Conference*, 2009. doi: 10.1115/ices2009-76080.
- [23] R. Rabute. Ring manufacturers’ perspective: Technical issues of interest and comparison of gas flow, oil consumption model results with engine measurements. *internal report, Dana Perfect Circle Europe*, 78301(1231), 1995.
- [24] Benoist (Benoist Pierre) Thirouard. *Characterization and modeling of the fundamental aspects of oil transport in the piston ring pack of internal combustion engines*. Phd dissertation, Massachusetts Institute of Technology. Dept. of Mechanical Engineering, Boston, Massachusetts, USA, 1972.
- [25] Goro Tamai. Experimental study of engine oil film thickness dependence on liner location, oil properties and operating conditions. <http://mit.dspace.org/handle/1721.1/31066>, 1995.
- [26] L. Bouke Noordzij. Measurement and analysis of piston inter-ring pressures and oil film thickness and their effects on engine oil consumption. <https://dspace.mit.edu/handle/1721.1/10925>, 1996.
- [27] T. Tian. *Modeling the Performance of the Piston Ring-pack in Internal Combustion Engines*. Massachusetts Institute of Technology, Department of Mechanical Engineering, 1997. URL <https://books.google.com/books?id=lJeFpwAACAAJ>.
- [28] Hideki Yoshida, Kazunori Kusama, and Hiroyuki Kobayashi. Diesel engine oil consumption depending on piston ring design. *SAE Technical Paper Series*, 1 1991. doi: 10.4271/911699.

- [29] Robert C. Fesser. Small engine piston ring design for reduced oil consumption. *SAE Technical Paper Series*, 1 1988. doi: 10.4271/881327.
- [30] Tian Tian, Remi Rabute, Victor W. Wong, and John B. Heywood. Effects of piston-ring dynamics on ring/groove wear and oil consumption in a diesel engine. *SAE Technical Paper Series*, 1997. doi: 10.4271/970835.
- [31] R. Rabute and T. Tian. Challenges involved in piston top ring designs for modern si engines. *Journal of Engineering for Gas Turbines and Power*, 123(2):448, 2001. doi: 10.1115/1.1364520.
- [32] H Yoshida. Effect of piston second land volume and land shape on oil consumption. *JSAE Review*, 16(3):326, 1995. doi: 10.1016/0389-4304(95)95177-v.
- [33] Eric W. Schneider, Daniel H. Blossfeld, Donald C. Lechman, Robert F. Hill, Richard F. Reising, and John E. Brevick. Effect of cylinder bore out-of-roundness on piston ring rotation and engine oil consumption. *SAE Technical Paper Series*, 1 1993. doi: 10.4271/930796.
- [34] Y. Ishizuki, F. Sato, and K. Takase. Effect of cylinder liner wear on oil consumption in heavy duty diesel engines. *SAE Technical Paper Series*, 1 1981. doi: 10.4271/810931.
- [35] Y. Chung. *Development and Analysis of a fire ring wear model for a piston engine*. Phd dissertation, Michigan State University, Mechanical Engineering Department, East Lansing, Michigan, USA, 1992.
- [36] L. J. Brombolich. Effect of cylinder distortion and piston ring effects on oil consumption and friction losses in automobile engines. *Tribology Project Research Report, Argonne National Laboratory*, 1989.
- [37] Mid Michigan Research. *CASE Theoretical Manual V5.3*. Mid Michigan Research Company, Okemos, Michigan, USA, 2007.
- [38] Ejakov Mikhail A. *Ring Pack Behavior and Oil Consumption Modeling in IC Engines*. Phd dissertation, Michigan State University, Mechanical Engineering Department, East Lansing, Michigan, USA, 2006.
- [39] Benoist Thirouard, Tian Tian, and Douglas P. Hart. Investigation of oil transport mechanisms in the piston ring pack of a single cylinder diesel engine, using two dimensional laser induced fluorescence. *SAE Technical Paper Series*, 1998. doi: 10.4271/982658.
- [40] What is ringpak. URL <https://www.software.ricardo.com/Products/RINGPAK>.
- [41] Mid Michigan Research. *CASE-RING*. Mid Michigan Research Company, Okemos, Michigan, USA, 2007.
- [42] Mahesh Puthiya Veettil and Fanghui Shi. Cfd analysis of oil/gas flow in piston ring-pack. *SAE Technical Paper Series*, 12 2011. doi: 10.4271/2011-01-1406.

- [43] Shoichi FURUHAMA. A dynamic theory of piston-ring lubrication : 2nd report, experiment. *Bulletin of JSME*, 3(10):291–297, 1960. doi: 10.1299/jsme1958.3.291.
- [44] P. N. Dowson, D. and Economou, B. L. Ruddy, P. J. Strachan, and A. J. S Baker. Piston ring lubrication - part iii: the influence of ring dynamics and ring twist. *Proceedings of Energy conservation through fluid film technology*, page 191, 1979.
- [45] B. L. Ruddy, D. Dowson, P. N. Economou, and Baker. The influence of thermal distortion and wear of piston ring grooves upon the lubrication of piston rings in diesel engines. *Energy Conservation Through Fluid Film Lubrication Technology: Frontiers in Research and Design, ASME Winter Meeting, ASME*, pages 191–215, 1979.
- [46] P. N. Dowson, D. and Economou, B. L. Ruddy, P. J. Strachan, and A. J. S Baker. Piston ring lubrication - part ii: theoretical analysis of a single ring and a complete ring pack. *Proceedings of Energy conservation through fluid film technology*, page 23, 1979.
- [47] M. Namazian and John B. Heywood. Flow in the piston-cylinder-ring crevices of a spark-ignition engine: Effect on hydrocarbon emissions, efficiency and power. *SAE Technical Paper Series*, 1 1982. doi: 10.4271/820088.
- [48] C. Chucholowski, H. Kornprobst, K. Zellinger, and Kolbenring. Kolbensekundarbewegung, 1982.
- [49] H. Kornprobst and K. Zellinger. Ringbewegung, 1987.
- [50] Tian Tian, Victor W. Wong, and John B. Heywood. A piston ring-pack film thickness and friction model for multigrade oils and rough surfaces. *SAE Technical Paper Series*, 1 1996. doi: 10.4271/962032.
- [51] T Tian. Dynamic behaviours of piston rings and their practical impact. part 2: Oil transport, friction and wear of ring/liner interface and the effects of piston and ring dynamics. *Proceedings of the Institution of Mechanical Engineers, Part J: Journal of Engineering Tribology*, 216(4):229–248, 2002. doi: 10.1243/135065002760199970.
- [52] Zafer Dursunkaya, Rifat Keribar, and Dana E. Richardson. Experimental and numerical investigation of inter-ring gas pressures and blowby in a diesel engine. *SAE Technical Paper Series*, 1 1993. doi: 10.4271/930792.
- [53] V. V. Dunaevsky, J. T. Sawicki, J. Frater, and H. Chen. Analysis of elastic distortions of a piston ring in the reciprocating air brake compressor due to the installation stresses. *SAE Technical Paper Series*, 1999. doi: 10.4271/1999-01-3770.
- [54] M. A. Ejakov, H. J. Schock, L. J. Brombolich, C. M. Carlstrom, and R. L. Williams. Simulation analysis of inter-ring gas pressure and ring dynamics and their effect on blow-by. In *19th Annual Fall Technical Conference of the ASME Internal Combustion Division*, volume 29 of 3, pages 107–123, Madison, WI, 9 1997. ASME.
- [55] Liang Liu, Tian Tian, and Remi Rabute. Development and applications of an analytical tool for piston ring design. *SAE Technical Paper Series*, 2003. doi: 10.4271/2003-01-3112.

- [56] Jan Hronza and David Bell. A lubrication and oil transport model for piston rings using a navier-stokes equation with surface tension. *SAE Technical Paper Series*, 2007. doi: 10.4271/2007-01-1053.
- [57] Christian Lotz Felter. Numerical simulation of piston ring lubrication. *Tribology International*, 41(9-10):914–919, 2008. doi: 10.1016/j.triboint.2007.11.018.
- [58] Hamed Shahmohamadi, Ramin Rahmani, Homer Rahnejat, Paul King, and Colin Garner. Cavitating flow in engine piston ring-cylinder liner conjunction. *Volume 7A: Fluids Engineering Systems and Technologies*, 2013. doi: 10.1115/imece2013-62395.
- [59] Y. K. Jiang, J. P. Zhang, G. Hong, L. P. Wan, and X. Liu. 3d ehd lubrication and wear for piston ring-cylinder liner on diesel engines. *International Journal of Automotive Technology*, 16(1):1–15, 2015. doi: 10.1007/s12239-015-0001-x.
- [60] Alexander Oliva, Stefan Held, Anatoli Herdt, and Georg Wachtmeister. Numerical simulation of the gas flow through the piston ring pack of an internal combustion engine. *SAE Technical Paper Series*, 2015. doi: 10.4271/2015-01-1302.
- [61] Chao Cheng, Ali Kharazmi, Harold Schock, Richard Wineland, and Larry Brombolich. Three dimensional piston ring-cylinder bore contact modeling. *Volume 2: Instrumentation, Controls, and Hybrids; Numerical Simulation; Engine Design and Mechanical Development; Keynote Papers*, 2014. doi: 10.1115/icef2014-5672.
- [62] Chao Cheng, Harold Schock, and Dan Richardson. The dynamics of second ring flutter and collapse in modern diesel engines. *Journal of Engineering for Gas Turbines and Power*, 137(11):111504, 12 2015. doi: 10.1115/1.4030291.
- [63] Mulyanto Poort, Chao Cheng, Dan Richardson, and Harold Schock. Piston ring and groove side wear analysis for diesel engines. *Journal of Engineering for Gas Turbines and Power*, 137(11):111503, 12 2015. doi: 10.1115/1.4030290.
- [64] Alice E. Smith and David W. Coit. *Penalty Function - Handbook of Evolutionary Computation, Section C 5.2*. A Joint Publication of Oxford University Press and Institute of Physics, 1996. URL <http://140.138.143.31/teachers/ycliang/heuristic%20optimization%20912/penalty%20function.pdf>.
- [65] Pavlo Lyubarsky and Dirk Bartel. 2d cfd-model of the piston assembly in a diesel engine for the analysis of piston ring dynamics, mass transport and friction. *Tribology International*, 104:352–368, 2016. doi: 10.1016/j.triboint.2016.09.017.
- [66] Mid-Michigan Research. *CASE User’s Manual Version 5.3*. Okemos, Michigan, USA, 2007.
- [67] Inc 3D Systems. *Stereolithography Interface Specification*. October 1989.
- [68] Marshall Burns. *Automated fabrication : improving productivity in manufacturing*. PTR Prentice Hall, Englewood Cliffs, N.J, 1993. ISBN 978-0131194625.
- [69] Right-hand rule, Mar 2017. URL https://en.wikipedia.org/wiki/Right-hand_rule.

- [70] Chao Cheng, Ali Kharazmi, and Harold Schock. Modeling of piston ring-cylinder bore-piston groove contact. *SAE Technical Paper Series*, 2015. doi: 10.4271/2015-01-1724.
- [71] Ravi Teja Vedula, Ruitao Song, Thomas Stuecken, Guoming G Zhu, and Harold Schock. Thermal efficiency of a dual-mode turbulent jet ignition engine under lean and near-stoichiometric operation. *International Journal of Engine Research*, page 146808741769997, 2017. doi: 10.1177/1468087417699979.
- [72] Chin-Hsiu Li. Piston thermal deformation and friction considerations. *SAE Technical Paper Series*, Jan 1982. doi: 10.4271/820086.
- [73] Franz Koch, Paul Decker, Robert Gulpen, Franz-Josef Quadflieg, and Malte Loeprecht. Cylinder liner deformation analysis - measurements and calculations. *SAE Technical Paper Series*, 1998. doi: 10.4271/980567.
- [74] ConvergeCFD. *Converge 2.2.0 Theory Manual*. Convergent Science, Inc, Madison, Wisconsin, USA, 2014.
- [75] James W. Murdock. *Fundamental fluid mechanics for the practicing engineer*. Dekker, 1993.
- [76] Z. U. A. Warsi. *Fluid dynamics: theoretical and computational approaches*. CRC Press, 1999.
- [77] B. E. Launder and D. B. Spalding. The numerical computation of turbulent flows. *Comput. Methods Appl. Mech. Eng.*, pages 269–289, September 1990. ISSN 0045-7825. URL <http://dl.acm.org/citation.cfm?id=99300.99301>.
- [78] Zhiyu Han and Rolf D. Reitz. A temperature wall function formulation for variable-density turbulent flows with application to engine convective heat transfer modeling. *International Journal of Heat and Mass Transfer*, 40(3):613–625, 1997. doi: 10.1016/0017-9310(96)00117-2.
- [79] Blaise Barney. Introduction to parallel computing. URL https://computing.llnl.gov/tutorials/parallel_comp.
- [80] Roger W. Hockney and Chris R. Jesshope. *Parallel computers 2: architecture, programming and algorithms*. Hilger, 1988.
- [81] Michael J. Flynn. Some computer organizations and their effectiveness. *IEEE Transactions on Computers*, C-21(9):948–960, 1972. doi: 10.1109/tc.1972.5009071.
- [82] G. Bell. Ultracomputers: A teraflop before its time. *Science*, 256(5053):64–64, Mar 1992. doi: 10.1126/science.256.5053.64.
- [83] Marcus Fritzsche. Parallel numerical simulation of navier-stokes-equations on gpus. <http://cfile219.uf.daum.net/attach/1567A0474F05F95A1D4AC9>, 2009.
- [84] *Parallel computing in computational fluid dynamics*, volume 578 of *AGARD Conference Proceedings*, 1995.

- [85] Anna Kallias. *Multikriterielle Optimierung des Kolbenringpakets Taschenbuch*. Institut für Antriebs- und Fahrzeugtechnik der Universität Kassel; Auflage, October 2010. ISBN 978-3939124146.
- [86] Tecplot cfd post-processor visualizes simulation data. URL <http://www.tecplot.com/>.
- [87] Ensign. URL <https://www.ensight.com/>.
- [88] G. G. Stokes. On the Effect of the Internal Friction of Fluids on the Motion of Pendulums. *Transactions of the Cambridge Philosophical Society*, 9:8, 1851.
- [89] C. De Petris, V. Giglio, and G. Police. Some insights on mechanisms of oil consumption. *SAE Technical Paper Series*, Jan 1996. doi: 10.4271/961216.
- [90] Yunliang Qi, Yaqi Xu, Zhi Wang, and Jianxin Wang. The effect of oil intrusion on super knock in gasoline engine. *SAE Technical Paper Series*, 2014.